

University of Alabama in Huntsville

LOUIS

Theses

UAH Electronic Theses and Dissertations

2020

Double wall heat transfer with full-coverage effusion with and without louver slot cooling

Austin Click

Follow this and additional works at: <https://louis.uah.edu/uah-theses>

Recommended Citation

Click, Austin, "Double wall heat transfer with full-coverage effusion with and without louver slot cooling" (2020). *Theses*. 335.

<https://louis.uah.edu/uah-theses/335>

This Thesis is brought to you for free and open access by the UAH Electronic Theses and Dissertations at LOUIS. It has been accepted for inclusion in Theses by an authorized administrator of LOUIS.

**DOUBLE WALL HEAT TRANSFER WITH FULL-COVERAGE EFFUSION WITH
AND WITHOUT LOUVER SLOT COOLING**

By

Austin Click

A Thesis

**Submitted in partial fulfillment of the requirements for the degree of
Master of Science in Mechanical Engineering**

In

The Department of Mechanical and Aerospace Engineering

To

The School of Graduate Studies

Of

The University of Alabama in Huntsville

**Huntsville, Alabama
2020**

In presenting this thesis in partial fulfillment of the requirements for a master's degree from The University of Alabama in Huntsville, I agree that the Library of this University shall make it freely available for inspection. I further agree that permission for extensive copying for scholarly purposes may be granted by my advisor or, in his/her absence, by the Chair of the Department or the Dean of the School of Graduate Studies. It is also understood that due recognition shall be given to me and to The University of Alabama in Huntsville in any scholarly use which may be made of any material in this thesis.

Austin J. Click

05/01/2020

(Student signature)

(Date)

THESIS APPROVAL FORM

Submitted by Austin Click in partial fulfillment of the requirements for the degree of Master of Science in Mechanical Engineering and accepted on behalf of the Faculty of the School of Graduate Studies by the thesis committee.

We, the undersigned members of the Graduate Faculty of The University of Alabama in Huntsville, certify that we have advised and/or supervised the candidate on the work described in this thesis. We further certify that we have reviewed the thesis manuscript and approve it in partial fulfillment of the requirements for the degree of Master of Science in Mechanical Engineering.

Phillip M. Ligrani May 1, 2020 Committee Chair

Dr. Phillip Ligrani (Date)

Jason T Cassibry May 2, 2020


Dr. Jason Cassibry

Sheng May 1, 2020


Dr. Guangsheng Zhang

Shankar Mahalingam May 2, 2020 Department Chair

Dr. Keith Hollingsworth

Shankar Mahalingam  Digitally signed by Shankar Mahalingam
DN: cn=Shankar Mahalingam, o=College of Engineering, ou=Dean, email=sm0026@uah.edu, c=US
Date: 2020.05.04 15:35:23 -0500 College Dean

Dr. Shankar Mahalingam

David Berkowitz  Digitally signed by David Berkowitz
DN: cn=David Berkowitz, o=University of Alabama in Huntsville, ou=Graduate Dean, email=berkowd@uah.edu, c=US
Date: 2020.05.04 16:21:03 -0500 Graduate Dean

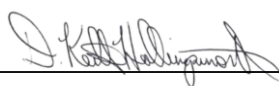
Dr. David Berkowitz

ABSTRACT

Presented are experimental heat transfer data for five different experimental configurations, where results are provided on different sides of the effusion plate, with full-coverage effusion cooling, both with and without louver slot injection. Three different coolant supply arrangements are considered, including a cross flow only arrangement, an impingement jet array only arrangement, and a combination cross flow and impingement jet array arrangement. Contraction ratios of 1 and 4 are used within the main flow passage to provide streamwise development with a zero pressure gradient, as well as with a strong favorable pressure gradient. With the five configurations, data are given for: (1) the film cooled side of the effusion plate, for effusion only cooling, with a combination coolant supply arrangement, (2) the cross flow side of the effusion plate, for effusion only cooling, with a combination coolant supply arrangement, (3) the film cooled side of the effusion plate, with louver and effusion combination cooling, with a combination coolant supply arrangement, (4) the cross flow side of the effusion plate, with louver and effusion combination cooling, with a combination coolant supply arrangement, and (5) the cross flow side of the effusion plate, with louver and effusion combination cooling, with an impingement only coolant supply. For configurations (1) and (2), also considered are the effects of different coolant supply arrangements on surface thermal performance for both sides of a double-wall cooled effusion plate. Configuration (1) results show that, overall, for larger x/d_e values, the cross flow/impingement combination behaves in a manner which is similar to the impingement only arrangement. For Configuration (2) Nusselt numbers generally increase with BR for each x/d_e location. Near impingement jets, Nusselt numbers approach impingement only values. Away from impingement jets, Nusselt numbers approach cross flow only configuration values. Configuration (3) results show that, when compared at the same effective blowing ratio or the same impingement jet Reynolds number, spanwise-averaged heat transfer coefficients are consistently lower, especially for the downstream portions of the test plate, when the louver is utilized. The presence of the louver slot additionally results in significantly larger adiabatic film cooling effectiveness values which are line-averaged, particularly at and near the upstream portions of the test plate. Nusselt numbers increase with BR (as x/d_e is constant) and proximity to impingement holes for Configuration (4) and for Configuration (5) for high and low mainstream Reynolds numbers.

Abstract Approval: Committee Chair Phillip M. Ligrani May 1, 2020

Dr. Phillip Ligrani

Department Chair  May 2, 2020

Dr. Keith Hollingsworth

Graduate Dean David Berkowitz

Digitally signed by David Berkowitz
DN: cn=David Berkowitz, o=University of Alabama in Huntsville,
ou=Graduate Dean, email=berkowi@uah.edu, c=US
Date: 2020.05.04 16:21:21 -0500

Dr. David Berkowitz

ACKNOWLEDGEMENTS

Dr. Phil Ligrani is the head of this project at the University of Alabama in Huntsville. He provides guidance for both students and sponsor on next steps and assists in every way he can. The sponsor of this project is Solar Turbines Incorporated of San Diego, California. This experiment, and thesis, would not be possible without their continued support, guidance, funding, and encouragement. I would also like to thank my family for their support and encouragement, as well as Natalie for her continued support, advice, and constant encouragement.

TABLE OF CONTENTS

	PAGE
Chapter 1: Introduction	1
1.1 Overview	1
1.2 Literature Survey	1
1.3 Thesis Organization	4
Chapter 2: Experimental Apparatus and Procedures	5
2.1 Double Wall Cooling Test Facility	5
2.2 Test Section and Test Surface for Effusion Only Cooling Arrangement	7
2.3 Test Section and Test Surface for Effusion and Louver Cooling Arrangement	8
2.4 Measurement of Flow Temperatures and Pressures	12
2.5 Impingement Flow Conditions and Parameters Determination	12
2.6 Cross Flow Conditions and Parameters Determination	13
2.7 Film Cooling Flow and Main Flow Conditions and Parameters Determination	13
2.8 Measurement of Surface Heat Transfer Coefficient and Adiabatic Wall Temperature Distributions - Main Flow Passage - Hot Surface of Effusion Plate	16
2.9 Measurement of Surface Nusselt Number Distributions – Impingement / Cross Flow Passage - Cold Surface of Effusion Plate	18
2.10 Uncertainty Analysis Results	20
Chapter 3: Effusion Only Cooling Data with Combination Coolant Supply for the Film Cooled Side of the Effusion Plate	22
3.1 Experimental Conditions	22
3.2 Pressure Variations and Flow Characteristics for Different Coolant Supply Arrangements	23
3.3 Line-Averaged Hot-Side Data for the Combination Cross Flow and Impingement Jet Array Arrangement	29
3.4 Line-Averaged Hot-Side Adiabatic Film Cooling Effectiveness Data for Different Coolant Supply Arrangements	30
3.5 Line-Averaged Hot-Side Heat Transfer Coefficient Data for Different Coolant Supply Arrangements	32
Chapter 4: Effusion Only Data with a Combination Coolant Supply for the Cross Flow Side of the Effusion Plate	35
4.1 Line-Averaged Cold-Side Data for the Combination Cross Flow and Impingement Jet Array Arrangement	35

4.2 Line-Averaged Cold-Side Nusselt Number Data for Different Coolant Supply Arrangements	36
Chapter 5: Louver and Effusion Combination Cooling with a Combination Coolant Supply Arrangement for the Film-Cooled Side of the Effusion Plate	39
5.1 Experimental Conditions	39
5.2 Louver and Effusion Configuration Geometry	41
5.3 Test Section Velocity, Pressure, Blowing Ratio, and Discharge Coefficient Variations	42
5.4 Local Surface Adiabatic Film Cooling Effectiveness and Local Surface Heat Transfer Coefficient Variations	45
5.5 Spanwise-Averaged Surface Heat Transfer Coefficient Variations	48
5.6 Spanwise-Averaged Surface Adiabatic Film Cooling Effectiveness Variations	52
Chapter 6: Louver and Effusion Combination Cooling with Combination Coolant Supply Arrangement for the Cross Flow Side of the Effusion Plate	56
6.1 Experimental Conditions	56
6.2 Test Section Velocity, Pressure, and Blowing Ratio Variations	57
6.3 Line-Averaged Cold-Side Data for the Combination Cross Flow and Impingement Jet Array Arrangement	62
6.4 Line-Averaged Cold-Side Nusselt Number Data for Different Coolant Supply Arrangements	63
Chapter 7: Louver and Effusion Combination Cooling with an Impingement Only Coolant Supply Arrangement for the Cross Flow Side of the Effusion Plate	66
7.1 Experimental Conditions	66
7.2 Test Section Velocity, Pressure, and Blowing Ratio Variations	67
7.3 Line-Averaged Cold-Side Data for the Impingement Jet Array Only Arrangement	71
7.4 Line-Averaged Cold-Side Nusselt Number Data for Different Coolant Supply Arrangements	72
7.5 Experimental Conditions	75
7.6 Test Section Velocity, Pressure, and Blowing Ratio Variations	76
7.7 Line-Averaged Cold-Side Data for Impingement Jet Array Only Arrangement	79
7.8 Line-Averaged Cold-Side Nusselt Number Data for Different Coolant Supply Arrangements	81
Chapter 8: Summary and Conclusions	84
References	88
Appendix A: Data File Directory	92

LIST OF FIGURES

Figures	Page
Figure 1a: Side-cut-away view of the CR=4 test section.	6
Figure 1b: Side-cut-away view of the CR=1 test section.	6
Figure 2a: Film cooling test plate.	8
Figure 2b: Impingement test plate.	9
Figure 2c: Film cooling test plate with louver slot cooling.	10
Figure 2d: Additional louver details.	10
Figure 3: Dimensions and layout of different layers of the effusion test plate.	11
Figure 4: Gray scale contours of an instantaneous infrared camera image for the film cooled, hot-side of the effusion test plate, for louver and effusion cooling with $Re_{ms,avg}=106610$.	17
Figure 5a: Comparisons of normalized pressure drop variations between crossflow to mainstream for cross flow and impingement flow together data with CR=4, impingement only data with CR=4, and cross flow only data with CR=4, for mainstream Reynold number values of $Re_{ms,avg}=222000-233000$.	19
Figure 5b: Comparisons of normalized pressure drop variations between impingement flow to mainstream for cross flow and impingement flow together data with CR=4, and impingement only data with CR=4, for mainstream Reynold number values of $Re_{ms,avg}=222000-233000$.	19
Figure 5c: Comparisons of normalized pressure drop variations between impingement flow to cross flow for cross flow and impingement flow together data with CR=4, and impingement only data with CR=4, for mainstream Reynold number values of $Re_{ms,avg}=222000-233000$.	20
Figure 6a: Comparisons of main stream static gage pressure with CR=4 for cross flow and impingement flow together data with CR=4, impingement only data with CR=4, and cross flow only data with CR=4, for mainstream Reynold number values of $Re_{ms,avg}=222000-233000$.	21
Figure 6b: Comparisons of mainstream velocity variations with CR=4 for cross flow and impingement flow together data with CR=4, impingement only data with CR=4, and cross flow only data with CR=4, for mainstream Reynold number values of $Re_{ms,avg}=222000-233000$.	22
Figure 6c: Streamwise variations of local flow acceleration parameter with cross flow and impingement flow together data with CR=4, impingement only data with CR=4, and cross flow only data with CR=4, for mainstream Reynold number values of $Re_{ms,avg}=222000-233000$.	22
Figure 7: Comparisons of effusion hole exit velocity variations with CR=4 for cross flow and impingement flow together data with CR=4, impingement only data with CR=4, and cross flow only data with CR=4, for mainstream Reynold number values of $Re_{ms,avg}=222000-233000$.	28

- Figure 8: Comparisons of local blowing ratio with CR=4 for cross flow and impingement flow together data with CR=4, impingement only data with CR=4, and cross flow only data with CR=4, for mainstream Reynold number values of $Re_{ms,avg}=222000-233000$. 38
- Figure 9: Hot-side line-averaged heat transfer coefficient variations with normalized streamwise location for different values of initial blowing ratio for cross flow and impingement flow together data with CR=4 for mainstream Reynold number values of $Re_{ms,avg}=222000$ to 233000 . 29
- Figure 10: Hot-side line-averaged adiabatic film cooling effectiveness variations with normalized streamwise location for different values of initial blowing ratio for cross flow and impingement flow together data with CR=4 for mainstream Reynold number values of $Re_{ms,avg}=222000-233000$. 30
- Figure 11: Hot-side line-averaged adiabatic film cooling effectiveness variations with initial blowing ratio for $x/de=30$ and $Re_{ms,avg}=222000-233000$, including comparisons with impingement only data and cross flow only data. 31
- Figure 12: Hot-side line-averaged adiabatic film cooling effectiveness variations with initial blowing ratio for $x/de=80$ and $Re_{ms,avg}=222000-233000$, including comparisons with impingement only data and cross flow only data. 32
- Figure 13: Hot-side line-averaged heat transfer coefficient variations with initial blowing ratio for $x/de=35$ and $Re_{ms,avg}=222000-233000$, including comparisons with impingement only data and cross flow only data. 33
- Figure 14: Hot-side line-averaged heat transfer coefficient variations with initial blowing ratio for $x/de=80$ and $Re_{ms,avg}=222000-233000$, including comparisons with impingement only data and cross flow only data. 33
- Figure 15: Cold-side line-averaged surface Nusselt number variations with normalized streamwise location for different values of initial blowing ratio for $Re_{ms,avg}=222000-233000$. Solid rectangles denote effusion hole entrance streamwise locations. Dashed rectangles denote impingement hole streamwise locations. 36
- Figure 16: Cold-side line-averaged surface Nusselt number variations with initial blowing ratio for $x/de=37$ and $Re_{ms,avg}=222000-233000$, including comparisons with impingement only data and cross flow only data. 37
- Figure 17: Cold-side line-averaged surface Nusselt number variations with initial blowing ratio for $x/de=40$ and $Re_{ms,avg}=222000-233000$, including comparisons with impingement only data and cross flow only data. 37
- Figure 18: Cold-side line-averaged surface Nusselt number variations with initial blowing ratio for $x/de=45$ and $Re_{ms,avg}=222000-233000$, including comparisons with impingement only data and cross flow only data. 38

Figure 19: Test section configuration. Left, a three-dimensional view of test plate, including louver slot device and full-coverage film cooling holes. Right, side cross-sectional view of louver slot. All dimensions given in millimeters.	41
Figure 20: Test section passages pressure drop variations with initial blowing ratio for the louver and full-coverage film cooling configuration and $Re_{ms,avg}=107000$ to 114000 .	42
Figure 21: Local main flow freestream velocity and spatially-averaged effusion flow velocity variations with initial blowing ratio for the louver and full-coverage film cooling configuration and $Re_{ms,avg}=107000$ to 114000 .	43
Figure 22: Local main flow static pressure changes with x/de normalized streamwise location for the louver and full-coverage film cooling configuration and $Re_{ms,avg}=107000$ to 114000 .	43
Figure 23: Local blowing ratio changes with x/de normalized streamwise location for the louver and full-coverage film cooling configuration and $Re_{ms,avg}=107000$ to 114000 .	44
Figure 24: Discharge coefficient changes as impingement jet Reynolds number varies for the louver and full-coverage film cooling configuration and $Re_{ms,avg}=107000$ to 114000 .	45
Figure 25: Local surface adiabatic film cooling effectiveness distribution for the louver and film cooling full-coverage configuration for a blowing ratio BR of 4.91 and $Re_{ms,avg}=107000$ to 114000 .	46
Figure 26: Local surface heat transfer coefficient distribution for the louver and film cooling full-coverage configuration for a blowing ratio BR of 4.91 and $Re_{ms,avg}=107000$ to 114000 .	46
Figure 27: Local heat transfer coefficient comparisons with effusion cooling only local data. Left, louver and effusion cooling data at $y/de = 11.5$. Right, louver and effusion cooling data at $y/de = 13.5$.	47
Figure 28: Local adiabatic film cooling effectiveness comparisons with effusion cooling only local data. Left, louver and effusion cooling data at $y/de = 11.5$. Right, louver and effusion cooling data at $y/de = 13.5$.	47
Figure 29: Heat transfer coefficient (spanwise-averaged) variations with x/de , provided at different blowing ratios for the louver and full-coverage film cooling configuration, $Re_{ms,avg}=107000$ to 114000 .	49
Figure 30: Heat transfer coefficient (spanwise-averaged) variations with x/de (at approximately the same effective blowing ratios of 5.2 and 5.3) for the effusion cooling only configuration, and for the louver and full-coverage film cooling configuration, $Re_{ms,avg}=107000$ to 114000 .	50
Figure 31: Heat transfer coefficient (spanwise-averaged) variations with x/de (at approximately the same effective blowing ratios of 6.9 and 7.3) for the effusion cooling only configuration, and for the louver and full-coverage film cooling configuration, $Re_{ms,avg}=107000$ to 114000 .	50
Figure 32: Heat transfer coefficient (spanwise-averaged) variations with x/de (at approximately the same impingement jet Reynolds numbers of 3399 and 3506) for the effusion cooling only	

configuration, and for the louver and full-coverage film cooling configuration, $Re_{ms,avg}=107000$ to 114000. 51

Figure 33: Heat transfer coefficient (spanwise-averaged) variations with x/de (at approximately the same impingement jet Reynolds numbers of 7668 and 7418) for the effusion cooling only configuration, and for the louver and full-coverage film cooling configuration, $Re_{ms,avg}=107000$ to 114000. 51

Figure 34: Adiabatic film cooling effectiveness (spanwise-averaged) variations with x/de , provided at different blowing ratios for the louver and full-coverage film cooling configuration, $Re_{ms,avg}=107000$ to 114000. 52

Figure 35: Adiabatic film cooling effectiveness (spanwise-averaged) variations with x/de (at approximately the same effective blowing ratios of 5.2 and 5.3) for the effusion cooling only configuration, and for the louver and full-coverage film cooling configuration, $Re_{ms,avg}=107000$ to 114000. 53

Figure 36: Adiabatic film cooling effectiveness (spanwise-averaged) variations with x/de (at approximately the same effective blowing ratios of 6.9 and 7.3) for the effusion cooling only configuration, and for the louver and full-coverage film cooling configuration, $Re_{ms,avg}=107000$ to 114000. 53

Figure 37: Adiabatic film cooling effectiveness (spanwise-averaged) variations with x/de (at approximately the same impingement jet Reynolds numbers of 3399 and 3506) for the effusion cooling only configuration, and for the louver and full-coverage film cooling configuration, $Re_{ms,avg}=107000$ to 114000. 54

Figure 38: Adiabatic film cooling effectiveness (spanwise-averaged) variations with x/de (at approximately the same impingement jet Reynolds numbers of 7668 and 7418) for the effusion cooling only configuration, and for the louver and full-coverage film cooling configuration, $Re_{ms,avg}=107000$ to 114000. 55

Figure 39: Normalized pressure variations between cross flow to mainstream for mainstream Reynolds values of $Re_{ms,avg}=166000$ to 176000. 58

Figure 40: Normalized pressure variations between impingement flow to mainstream for mainstream Reynolds values of $Re_{ms,avg}=166000$ to 176000. 58

Figure 41: Normalized pressure variations between impingement flow to cross flow for mainstream Reynolds values of $Re_{ms,avg}=166000$ to 176000. 59

Figure 42: Mainstream velocity variations with normalized streamwise location for mainstream Reynolds values of $Re_{ms,avg}=166000$ to 176000. 60

Figure 43: Effusion hole exit velocity variations with normalized streamwise location for mainstream Reynolds values of $Re_{ms,avg}=166000$ to 176000. 60

Figure 44: Mainstream pressure variations with normalized streamwise location for mainstream Reynolds values of $Re_{ms,avg}=166000$ to 176000. 61

- Figure 45: Blowing ratio variations with normalized streamwise location for mainstream Reynolds values of $Re_{ms,avg}=166000$ to 176000 . 61
- Figure 46: Cold-side line-averaged surface Nusselt number variations with normalized streamwise location for different values of initial blowing ratio for $Re_{ms,avg}=166000$ to 176000 . Solid rectangles denote effusion hole entrance streamwise locations. Dashed rectangles denote impingement hole streamwise locations. 63
- Figure 47: Comparison of line-averaged surface Nusselt number variations for louver and effusion cooling with $CR=1$ and $BR=3.9$, and effusion only cooling with $CR=4$ for and $BR=4.8$. 64
- Figure 48: Comparison of line-averaged surface Nusselt number variations for louver and effusion cooling with $CR=1$ and $BR=4.7$, and effusion only cooling with $CR=4$ for and $BR=5.7$. 64
- Figure 49: Comparison of line-averaged surface Nusselt number variations for louver and effusion cooling with $CR=1$ and $BR=5.4$, and effusion only cooling with $CR=4$ for and $BR=6.5$. 65
- Figure 50: Comparison of line-averaged surface Nusselt number variations for louver and effusion cooling with $CR=1$ and $BR=6.5$, and effusion only cooling with $CR=4$ for and $BR=7.7$. 65
- Figure 51: Normalized pressure variations between cross flow to mainstream flow for mainstream Reynolds values of $Re_{ms,avg}=145000$ to 161000 . 68
- Figure 52: Normalized pressure variations between impingement flow to mainstream flow for mainstream Reynolds values of $Re_{ms,avg}=145000$ to 161000 . 68
- Figure 53: Normalized pressure variations between impingement flow to cross flow for mainstream Reynolds values of $Re_{ms,avg}=145000$ to 161000 . 69
- Figure 54: Mainstream pressure variations for mainstream Reynolds values of $Re_{ms,avg}=145000$ to 161000 . 69
- Figure 55: Mainstream velocity variations for mainstream Reynolds values of $Re_{ms,avg}=145000$ to 161000 . 70
- Figure 56: Effusion hole velocity variations for mainstream Reynolds values of $Re_{ms,avg}=145000$ to 161000 . 70
- Figure 57: Blowing ratio variations for mainstream Reynolds values of $Re_{ms,avg}=145000$ to 161000 71
- Figure 58: Cold-side line-averaged surface Nusselt number variations with normalized streamwise location for different values of initial blowing ratio for $Re_{ms,avg}=145000$ to 161000 . Solid rectangles denote effusion hole entrance streamwise locations. Dashed rectangles denote impingement hole streamwise locations. 72
- Figure 59: Comparison of line-averaged surface Nusselt number variation between impingement only and cross flow and impingement together for $BR=2.3$ and $BR=3.9$, respectively. 73

Figure 60: Comparison of line-averaged surface Nusselt number variation between impingement only and cross flow and impingement together for BR=3.6 and BR=4.7, respectively.	73
Figure 61: Comparison of line-averaged surface Nusselt number variation between impingement only and cross flow and impingement together for BR=5.2 and BR=5.4, respectively.	73
Figure 62: Comparison of line-averaged surface Nusselt number variation between impingement only and cross flow and impingement together for BR=6.3 and BR=6.1, respectively.	74
Figure 63: Normalized pressure variations between cross flow to mainstream for mainstream Reynolds values of $Re_{ms,avg}=92000$ to 102000.	76
Figure 64: Normalized pressure variations between impingement flow to mainstream for mainstream Reynolds values of $Re_{ms,avg}=92000$ to 102000.	77
Figure 65: Normalized pressure variations between impingement flow to cross flow for mainstream Reynolds values of $Re_{ms,avg}=92000$ to 102000.	77
Figure 66: Mainstream pressure variations for mainstream Reynolds values of $Re_{ms,avg}=92000$ to 102000.	78
Figure 67: Mainstream velocity variations for mainstream Reynolds values of $Re_{ms,avg}=92000$ to 102000.	78
Figure 68: Effusion hole exit velocity variations for mainstream Reynolds values of $Re_{ms,avg}=92000$ to 102000.	79
Figure 69: Blowing ratio variations for mainstream Reynolds values of $Re_{ms,avg}=92000$ to 102000.	79
Figure 70: Cold-side line-averaged surface Nusselt number variations with normalized streamwise location for different values of initial blowing ratio for $Re_{ms,avg}=92000$ to 102000. Solid rectangles denote effusion hole entrance streamwise locations. Dashed rectangles denote impingement hole streamwise locations.	80
Figure 71: Comparison of line-averaged surface Nusselt number variation between impingement only and cross flow and impingement together for BR=2.3 and BR=3.7, respectively.	81
Figure 72: Comparison of line-averaged surface Nusselt number variation between impingement only and cross flow and impingement together for BR=3.7 and BR=4.6, respectively.	82
Figure 73: Comparison of line-averaged surface Nusselt number variation between impingement only and cross flow and impingement together for BR=5.4 and BR=5.3, respectively.	82
Figure 74: Comparison of line-averaged surface Nusselt number variation between impingement only and cross flow and impingement together for BR=6.3 and BR=6.1, respectively.	83

LIST OF TABLES

Tables	Page
Table 1: Full-coverage film cooling experimental conditions.....	23
Table 2: Film Cooling full-coverage experimental conditions.....	40
Table 3: Louver slot cooling experimental conditions.....	40
Table 4: Louver slot cooling effective blowing ratios.....	41
Table 5: Film cooling full-coverage experimental conditions.....	57
Table 6: Louver slot cooling experimental conditions.....	57
Table 7: Louver slot cooling effective blowing ratios.....	57
Table 8: Experimental Conditions for Impingement Only for mainstream Reynolds number values of $Re_{ms,avg}=145000$ to 161000	66
Table 9: Louver slot cooling experimental conditions.....	67
Table 10: Louver slot cooling effective blowing ratios.....	67
Table 11: Experimental Conditions for Impingement Only for mainstream Reynolds number values of $Re_{ms,avg}=92000$ to 102000	75
Table 12: Louver slot cooling experimental conditions.....	75
Table 13: Louver slot cooling effective blowing ratios.....	76

LIST OF SYMBOLS

A	area
A_e	cross-sectional area of each film cooling hole
A_{ht}	area of the etched foil heater
BR_e	effusion cooling blowing ratio
C_d	discharge coefficient
CR	main flow passage contraction ratio
d_e	film cooling hole diameter
DH	hydraulic diameter
DR	effusion cooling density ratio
h	local iso-energetic heat transfer coefficient
\bar{h}	line-averaged iso-energetic heat transfer coefficient
I	effusion cooling momentum flux ratio, current
k	molecular thermal conductivity
k_{pst}	molecular thermal conductivity of polystyrene
k_{PVC}	molecular thermal conductivity of polyvinylchloride (PVC)
K	flow acceleration parameter
l_1	embedded thermocouple depth for the film cooled side of the effusion test plate
l_2	embedded thermocouple depth for the cross flow side of the effusion test plate
M	Mach number
\dot{m}	mass flow rate
N_e	number of holes in the film cooling test plate
Nu	local Nusselt number
\overline{Nu}	line-averaged Nusselt number
P	pressure, power
ΔP	differential pressure
Q	heat power
Q_{cret}	corrected heat power
\dot{q}_o''	surface heat flux
R	gas constant
Re_{cf}	cross flow Reynolds number, $\frac{DH_{cf} \cdot V_{cf}}{\nu_{cf}}$
Re_{ef}	effusion flow Reynolds number, $\frac{V_{ef} \cdot d_e}{\nu_{ef}}$

Re_i	impingement flow Reynolds number, $\frac{\rho_{s,i}V_i d_i}{\mu_i}$
Re_{ms}	main flow Reynolds number, $\frac{DH_{ms} \cdot V_{ms}}{v_{ms}}$
$Re_{ms,avg}$	main flow Reynolds number, $\frac{DH_{ms} \cdot V_{ms,avg}}{v_{ms}}$
t	thickness of PVC core
T	temperature
T_{aw}	local adiabatic wall temperature
T_{LC}	liquid crystal temperature
T_{surf}	surface/wall temperature
T_s	static temperature
T_t	stagnation temperature
T_{icl}	thermocouple temperature
T_{wcrct}	corrected wall temperature
V	time-averaged flow velocity
V	Voltage
VR	effusion cooling velocity ratio
x	streamwise coordinate
X	streamwise film hole spacing
y	spanwise coordinate
Y	spanwise film hole spacing

GREEK SYMBOLS

η	local adiabatic film cooling effectiveness
$\bar{\eta}$	line-averaged adiabatic film cooling effectiveness
μ	absolute viscosity
ρ	air density
ρ_s	static air density

SUBSCRIPTS

Avg	average value
aw	adiabatic wall value
c	cross flow coolant supply channel value
cf	cross flow value
crct	corrected value
e	effusion hole value

ef	effusion jet value
ht	heater
ideal	ideal value
i	impingement value
imp	impingement value
Local	local value
LC	liquid crystal
M	main flow value
ms	local main flow value, or main flow value based upon inlet hydraulic diameter, and freestream flow velocity at inlet of main flow passage
ms,avg	main flow value based upon inlet hydraulic diameter, and flow velocity averaged along streamwise length of main flow passage
s	static value
surf	surface value
t	stagnation value
tc	thermocouple
w	wall value

Chapter 1: Introduction

The present chapter provides an overview of the experiment, a literature survey, and discussion of thesis organization.

1.1 Overview

The apparatus for the present experiment is located the Propulsion Research Center at the University of Alabama in Huntsville. Investigated is a double wall cooling arrangement of an effusion test plate. This arrangement models combustor liner configurations which are employed in utility gas turbine engines. Within this experimental facility, three separate channels are used to supply the airflow for the main flow, the cross flow, and the impingement jet array flow. The flow rate for each channel is independently provided and controlled using blowers connected to frequency drives. With this arrangement, the test facility can be configured for different cooling supply arrangements. Several different cooling supply arrangements and two different main flow film cooling arrangements are utilized in the present investigation.

1.2 Literature Survey

Rogers et al. (2016), Schulz et al. (2001), and Krewinkle et al. (2013) discuss a variety of complex cooling and thermal protection approaches for combustor liners. Andrews, et al. (1988), Al Dabagh, et al. (1990), Andrews, et al. (1992), and Andrews and Nazari (1999) describe results from investigations which employ effusion cooling and impingement cooling together. All four of these studies measure pressure loss variations through coolant supply systems, and demonstrate the importance of the number of effusion holes and the number of impingement holes on local and overall surface thermal protection. Andrews, et al. (1988) also show that combined impingement and effusion cooling has higher effectiveness than impingement alone. Al Dabagh et al. (1990) provides additional consideration of the optimum number of impingement cooling holes for a given number of effusion holes. According to these investigators, the optimum configuration results when the number of holes for both cooling techniques is the same, arranged such that each impingement cooling hole is located exactly in the middle of four effusion cooling holes.

Cho and Rhee (2001) later demonstrate that heat/mass transfer is augmented with decreased spacing distances between the impingement and effusion plates. A naphthalene sublimation

experimental technique is employed by these investigators to determine spatially-resolved distributions of local heat transfer coefficients along the target surface of the effusion plate, as it is cooled using an array of impingement jets, for Reynolds numbers of 5000 to 12000. Local heat/mass transfer coefficients are also measured using a naphthalene sublimation method by Hong et al. (2007). For this investigation, the influences of different-shaped fins, installed between the impingement and effusion plates, are considered as they affect fluid mechanics and thermal characteristics. Crossflow blowing ratio ranges from 0.5 to 1.5, for a fixed jet Reynolds number of 10,000. Cho et al. (2008) employ the same effusion/impingement cooling configuration, and consider the effects of hole arrangements on local surface heat transfer characteristics, with relatively small hole spacing. Cho et al. (2008) demonstrate that a staggered hole arrangement provides improved performance, relative to an in-line hole arrangement.

Miller et al. (2014) consider different streamwise and spanwise spacings of effusion holes and impingement holes, and different impingement jet-to-target plate distances. Shi et al. (2016) investigate a configuration such that one impingement hole is present for each effusion hole, wherein the same streamwise spacing and spanwise spacing are used for both the effusion and impingement holes. Measured are surface distributions of mainstream-side, cooling effectiveness. According to Oguntade et al. (2017), overall cooling effectiveness for impingement/effusion cooling is higher, relative to effusion cooling alone, especially for rows of holes at locations which are farther upstream. Farther downstream, the addition of impingement cooling to effusion cooling results in only small increases in overall cooling effectiveness for the experimental conditions which are considered within the investigation. El-Jumamah et al. (2016, 2017) consider arrangements with a fixed impingement jet-target distance, and a fixed number of impingement holes. These investigators show that surface-averaged heat transfer coefficients generally increase as the number of effusion holes becomes larger.

Very little information is available regarding the use of louver slot cooling to provide thermal protection of combustor liners within gas turbine engines. Of the very limited number of past investigations which consider louver slot cooling, one of the earliest is described by Juhasz and Marek (1971). These investigators use a variety of slot arrangements within a simulated combustor segment of a gas turbine, with a rectangular cross-section. Correlation equations are provided which match experimental results, which are based upon a mixing model for local flow turbulence. According to Lefebvre (1998), such slot arrangements, including annular slot configurations, are

an efficient means of providing enhanced thermal protection to the inner wall of a combustor liner, provided axial injection paths are utilized. Jia et al. (2003) use both experimental and numerical tools to document the performance, at different blowing ratios, of angled film cooling slots. According to these investigators, different boundary condition arrangements affect numerically-obtained velocity profiles in a significant manner, but do not affect film cooling effectiveness distributions. Cooling injection angle also affects the size and development of the resulting recirculation bubbles. Ceccherini et al. (2009) consider overall influences of slot, effusion, and dilution holes, using both experimental measurements and numerical predictions. The investigators indicate that cooling effectiveness magnitudes and distributions are affected in a significant manner by values of the exit velocity associated with effusion cooling. In a follow-up study with the same liner cooling configurations, Andreini et al. (2010) address heat transfer coefficient behavior also using numerical prediction tools. In a later experimental investigation, Andreini et al. (2012) investigate magnitudes of heat flux reduction, heat transfer coefficient, and film cooling effectiveness downstream of louver slots. Considered are the influences of velocity ratio and blowing ratio for experimental configurations which are associated with operating combustor components within aero engines.

Inanli et al. (2017) employ six different slot configurations in combination with several different effusion cooling arrangements. Each louver device is referred to as a leap geometry, with investigation of both flat and angled leap configurations. Effusion cooling configurations utilize two different effusion hole angles. With consideration of film cooling effectiveness distributions, the straight leap geometry generally provides better performance relative to the angled arrangement, provided results are compared at the same blowing ratio. With the straight geometry, magnitudes of mean cooling effectiveness range from 0.60 to 0.70. Kiyici et al. (2018) provide numerically predicted results for the same arrangements and experimental conditions which are employed by Inanli et al. (2017). Considered by Kiyici et al. (2018) are three different blowing ratio values, and three different slot heights. The numerical results, and the associated experimental data, show that mean effectiveness varies only slightly as either streamwise location or blowing ratio is varied. Da Silva et al. (2018) describe film cooling effectiveness and local velocity variations associated with a louver combined scheme for a freestream velocity of 6.0 m/s and an inlet hole coolant blowing ratio of 0.87. Centerline film cooling effectiveness values range from

magnitudes near 1.0, with decreasing values with streamwise development, such that values eventually approach 0.2 to 0.5, depending upon the magnitude of blowing ratio.

1.3 Thesis Organization

Within the present thesis, Chapter 1 gives an introduction. Chapter 2 provides a description of the experimental apparatus and procedures. Chapter 3 presents experimental data for the film cooled side of the effusion plate, for effusion only cooling, with a combination coolant supply arrangement. Chapter 4 presents experimental data for the cross flow side of the effusion plate, for effusion only cooling, with a combination coolant supply arrangement. Chapter 5 presents experimental data for the film cooled side of the effusion plate, with louver and effusion combination cooling, with a combination coolant supply arrangement. Chapter 6 presents experimental data for the cross flow side of the effusion plate, with louver and effusion combination cooling, with a combination coolant supply arrangement. Chapter 7 presents experimental data for the cross flow side of the effusion plate, with louver and effusion combination cooling, with an impingement only coolant supply. Chapter 8 provides a summary and conclusions. Presented in Appendix A are references. Appendix B provides a data file directory. Appendix C provides a software directory.

Chapter 2: Experimental Apparatus and Procedures

The present chapter provides information on the double wall cooling test facility, test section, and test surfaces, measurement procedures for temperatures and pressures, coolant supply conditions and parameters, film cooling and main flow conditions and parameters, measurement of surface heat transfer coefficients (for the film-cooled side of the effusion plate), measurement of surface adiabatic film cooling effectiveness (for the film-cooled side of the effusion plate), and measurement of surface Nusselt numbers (for the cross flow side of the effusion plate).

2.1 Double Wall Cooling Test Facility

The blower for the main flow operates in a suction mode. This ensures the flow moves in the correct direction through the effusion plate. Flow enters the facility into a nozzle which is 762 mm by 419.1 mm. The exit of the nozzle is 254 mm by 419.1 mm. Following the nozzle is a mesh heater, and then a short duct, and then a second mesh heater. A second duct is attached directly to the test section. Following the test section, a 609.6 mm long duct connects to the main flow blower. The two mesh heaters are composed of Kanthol-D wire mesh, and are connected in series to an Ametek Sorensen SGA60/500D 30 kilowatt DC power supply. These mesh heaters are employed to generate a timewise step increase in air flow static temperature of the mainstream air, after all facility flow conditions are established. The heaters are insulated on either side by 12 mm Teflon gaskets to prevent thermal and electrical interaction with the rest of the facility. These heaters provide a step in temperature of up to 12 degrees Celsius for the main flow hot side of the test plate. Downstream of the second heater, a static pressure tap and Kiel probe are employed to determine static and total pressures. Kiel probes are United Sensor Corporation KCC-8 Kiel probes. Three thermocouples are mounted parallel to the flow for temperature measurements. The thermocouples used are Omega 5TC-TT-T40-72 fine-wire copper-constantan (Type T) thermocouples. In the test section, four static pressure taps are used to determine test sections flow conditions. These taps are at the midpoint of the test section, between the wall and test plate. The taps are used to determine pressure variations along the main flow.

The cross flow and impingement flow coolant supplies operate with the blowers in a pressurizing mode. The cross flow blower is attached to a small plenum that connects from the round blower to the square coolant supply configuration. This nozzle inlet is 355.6 mm by 419.1

mm. The exit of the cross flow nozzle is 88.9 mm by 419.1 mm. The end of the cross flow passage is blocked by an end cap. Figure 1a shows a schematic drawing of a side-cut-away view of the CR=4 test section. Figure 1b shows a schematic drawing of a side-cut-away view of the CR=1 test section.

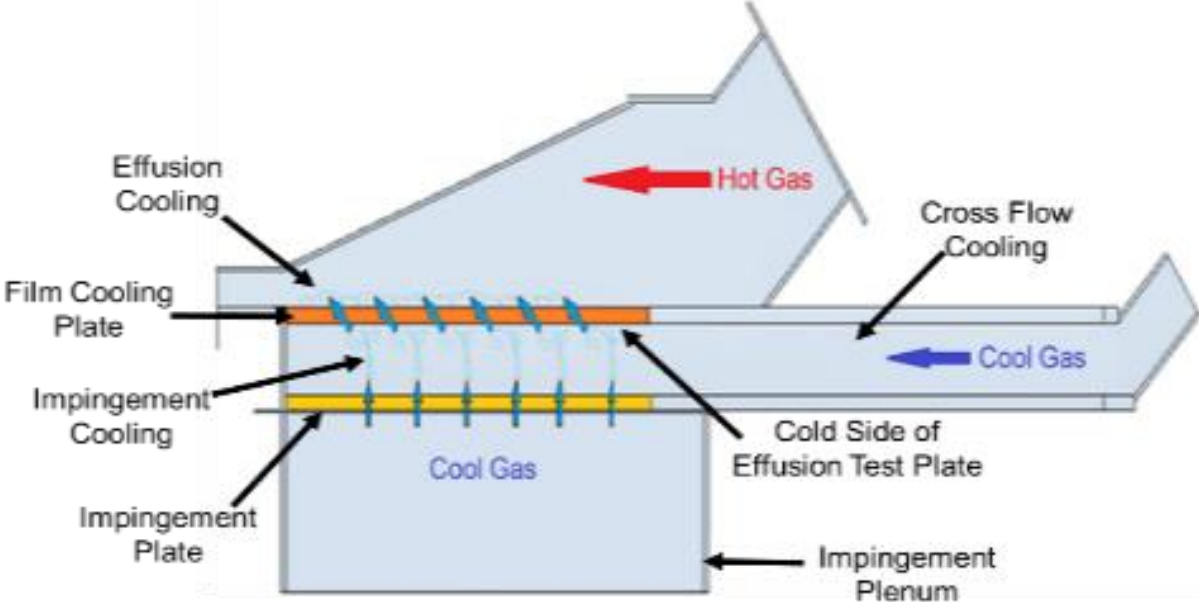


Figure 1a: Side-cut-away view of the CR=4 test section.

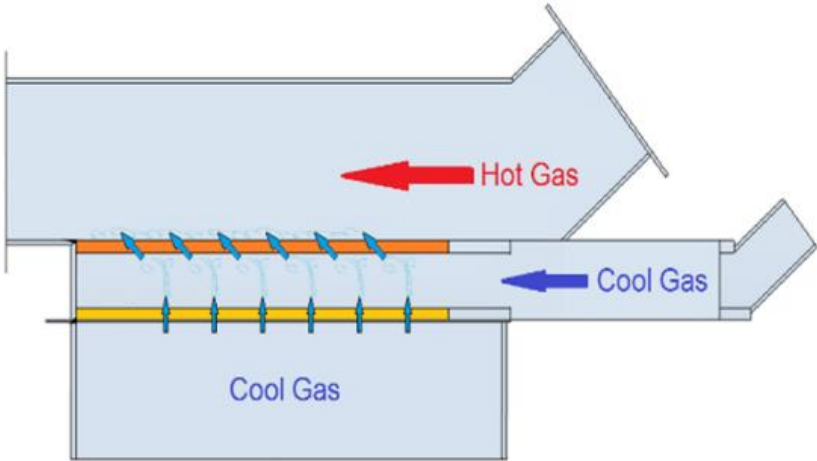


Figure 1b: Side-cut-away view of the CR=1 test section.

The impingement blower is attached to a plenum 781.05 mm by 635 mm by 635 mm. The plenum is connected to a supply pipe. This pipe diameter is 152.4 mm. The length of the pipe is 1066.8 mm. This pipe connects to another, shorter length of pipe of the same diameter. Between these pipes is an ASME orifice plate used for air mass flow rate measurements. This pipe leads to a second plenum where flow straightening mesh and a baffle are located before the impingement plate. Inside the plenum, a Chameleon3 CM3-U3-13Y3C 1.3 MP Color USB3 VISION camera, with ON Semi PYTHON 1300 sensor and a 4.5 mm EO Megapixel Fixed Focal Length Lens. It is used to capture images of the liquid crystal side of the test plate. After the plenum is the impingement plate. The impingement plate is clear acrylic to allow the camera to view the effusion test plate. The plate has 60 holes, arranged in the same pattern as the effusion test plate. The holes are 8.33 mm in diameter and are perpendicular to the cross flow and main flow direction.

To provide airflow for the three channels, a blower is employed for each. The main flow blower is a New York Blower Co. model 1708A pressure blower with a 15 HP, 1800 RPM motor. The cross flow blower is a New York Blower Co. model 1808S with a 7.5 HP, 1800 RPM motor. The impingement flow blower is a New York Blower Co. model 2404A with a 15 HP, 1800 RPM motor. All three blowers are powered by three phase variable frequency drives from Fuji Electric. Blower frequency settings are adjusted to achieve desired conditions. To control the temperature for the coolant supply, a heat exchanger is employed before the cross flow and impingement flow blowers. Liquid nitrogen at 22 PSI (151.685 kPa) is then passed through to reduce the temperature. This heat exchanger is then connected to an 8 inch (203.2 mm) Tee that splits the cooled air between the cross flow and impingement flow respectively.

2.2 Test Section and Test Surface for Effusion Only Cooling Arrangement

The test plate used for this experiment is 711.2 mm in the longitudinal direction, and 431.8 mm in the spanwise direction. For the effusion only plate, 60 holes are present. These holes are configured in 6 rows of 10 holes. The holes are 6.35 mm in diameter, are angled at 25 degrees with respect to the flow direction. The first row of holes starts 121.44 mm on center from the leading edge of the plate. The rows are arranged in a staggered pattern. Spanwise position of adjacent holes are 25.4 mm apart from one centerline to another. Effusion holes are separated in the streamwise direction by 95.25 mm.

The core material of the effusion test plate is polyvinyl chloride (PVC) type 1 plastic. It is 16 mm thick with an approximate thermal conductivity of 0.17 W/mK. The coolant side of the test plate has a 0.5 mm Kapton heater between the PVC core and the outer polystyrene layer. The outer layers of the test plate are 1.5 mm polystyrene layers, with an approximate thermal conductivity of 0.22 W/mK. The overall thickness of the plate is 19.5 mm when all four layers are assembled. Six thermocouples reside in each of the two polystyrene layers. The thermocouples used are Omega 5TC-TT-T40-72 fine-wire copper-constantan (Type T) thermocouples. The channels for each thermocouple are 0.6 x 0.6 mm. The thermocouples are secured in place with Loctite® epoxy, with an approximate thermal conductivity of 0.20 W/mK. Figure 2a shows a schematic drawing of the effusion test plate, and Figure 2b shows a schematic drawing of the impingement plate.

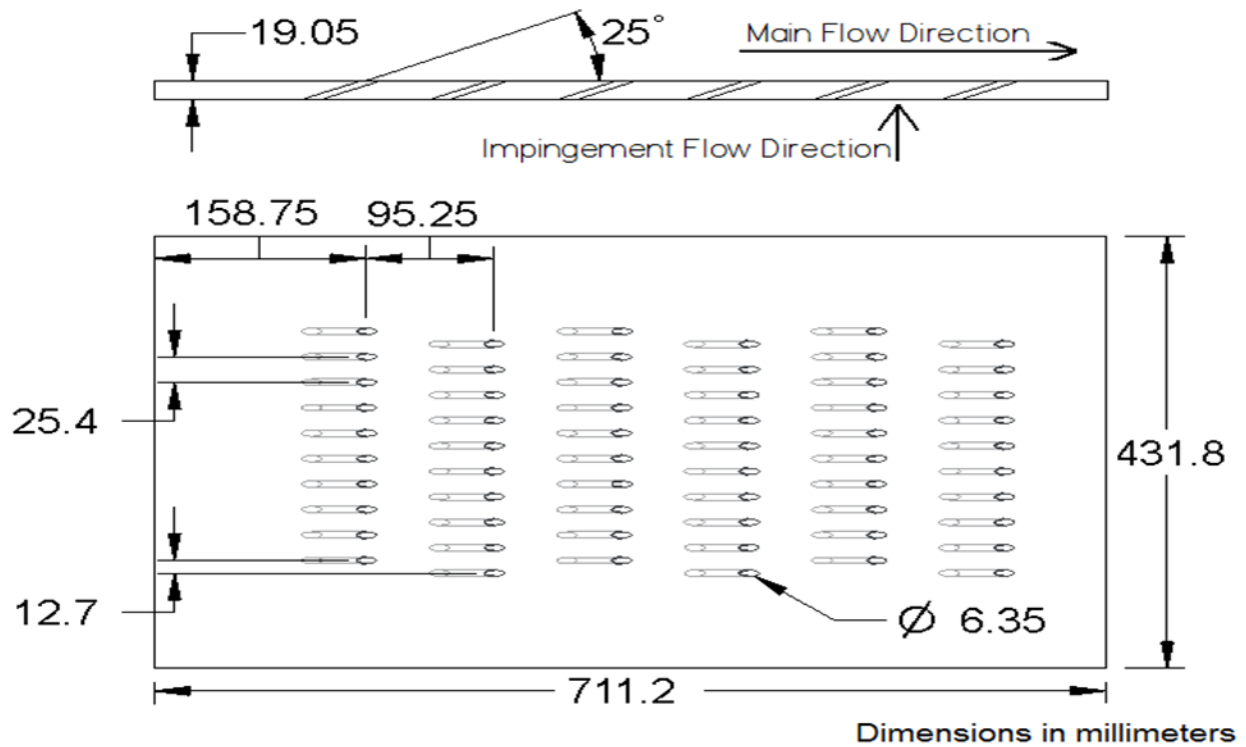


Figure 2a: Film cooling test plate.

2.3 Test Section and Test Surface for Effusion and Louver Cooling Arrangement

The test plate used in the combination louver and effusion cooling is similar to the effusion only plate. In addition to the 60 effusion holes, 11 louver feed holes are present. The louver holes are positioned at $x = 88.69$ mm from the leading edge of the plate. Louver holes are oriented at 90

degrees to the flow. A throttle slide is included as part of the test plate. The slide is 25.4 mm wide, is centered on the louver holes, and is the entire width of the plate. The channel for the slide includes an ultra-high molecular weight polyethylene barrier to prevent the throttle slide from adhering to the Kapton heater present inside the plate. The throttle slide is arranged to leave the louver holes fully open in the present experiment.

The core material of the effusion test plate is polyvinyl chloride (PVC) type 1 plastic. It is 16 mm thick with an approximate thermal conductivity of 0.17 W/mK. The coolant side of the test plate has a 0.5 mm Kapton heater between the PVC core and the outer polystyrene layer. The outer layers of the test plate are 1.5 mm polystyrene layers, with an approximate thermal conductivity of 0.22 W/mK. The overall thickness of the plate is 19.5 mm when all four layers are assembled. Six thermocouples reside in each of the two polystyrene layers. The thermocouples used are Omega 5TC-TT-T40-72 fine-wire copper-constantan (Type T) thermocouples. The channels for each thermocouple are 0.6 x 0.6 mm. The thermocouples are secured in place with Loctite® epoxy, with an approximate thermal conductivity of 0.20 W/mK. Figure 2c shows a schematic drawing of the louver and effusion test plate. Figure 2d presents detailed schematic drawings with additional louver details. Figure 3 shows the dimensions and layout of different layers of the effusion test plate.

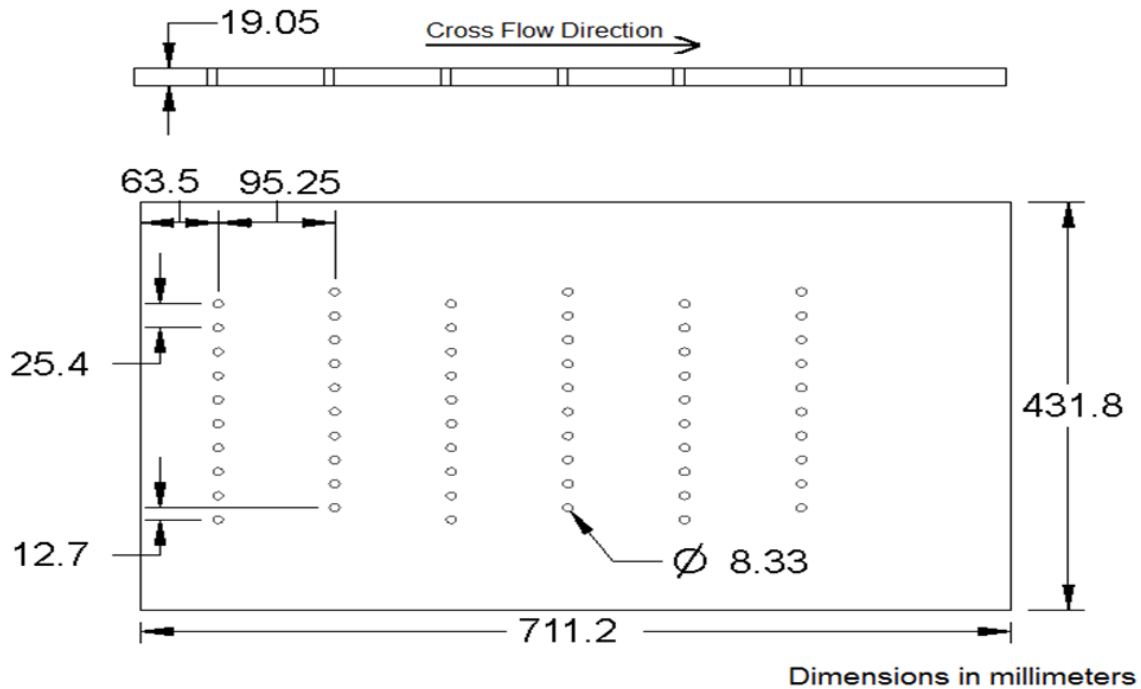


Figure 2b: Impingement test plate.

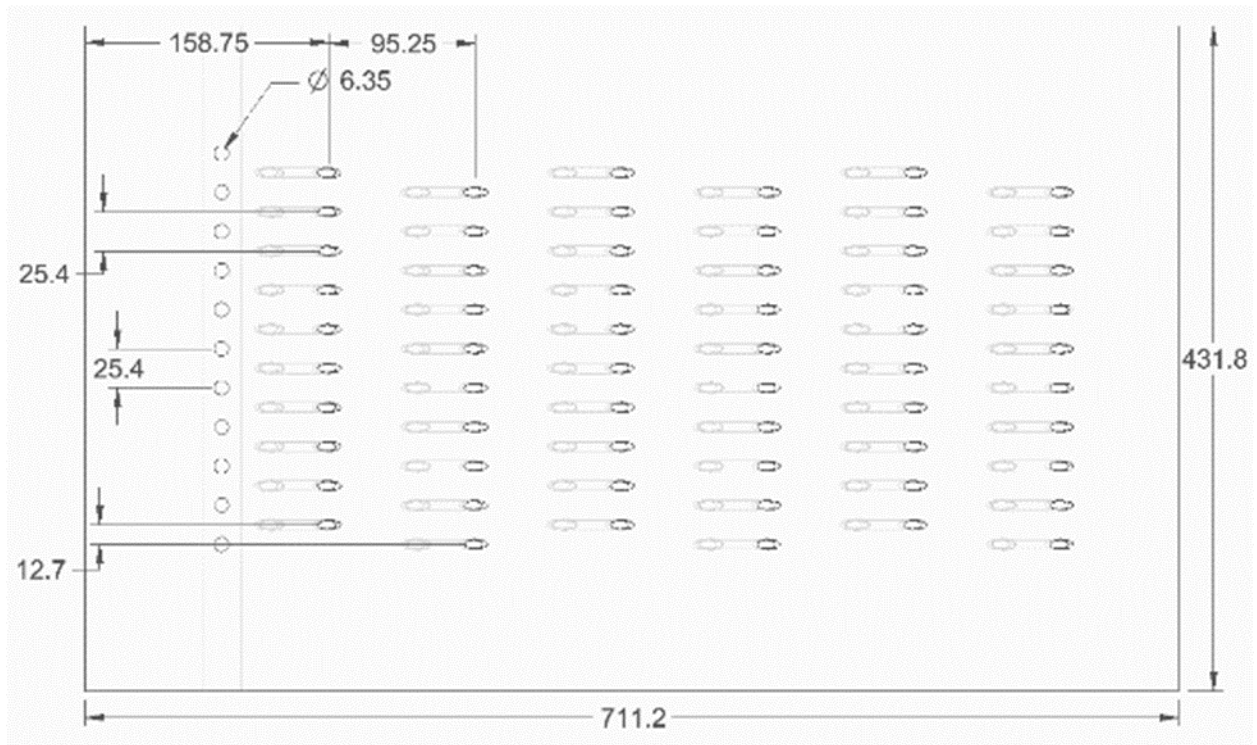


Figure 2c: Film cooling test plate with louver slot cooling.

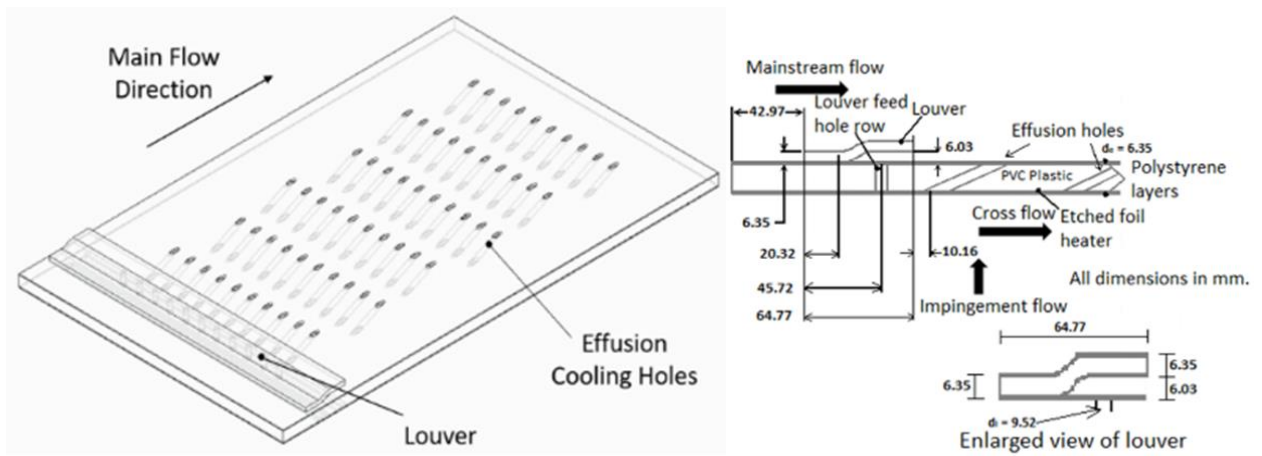


Figure 2d: Additional louver details.

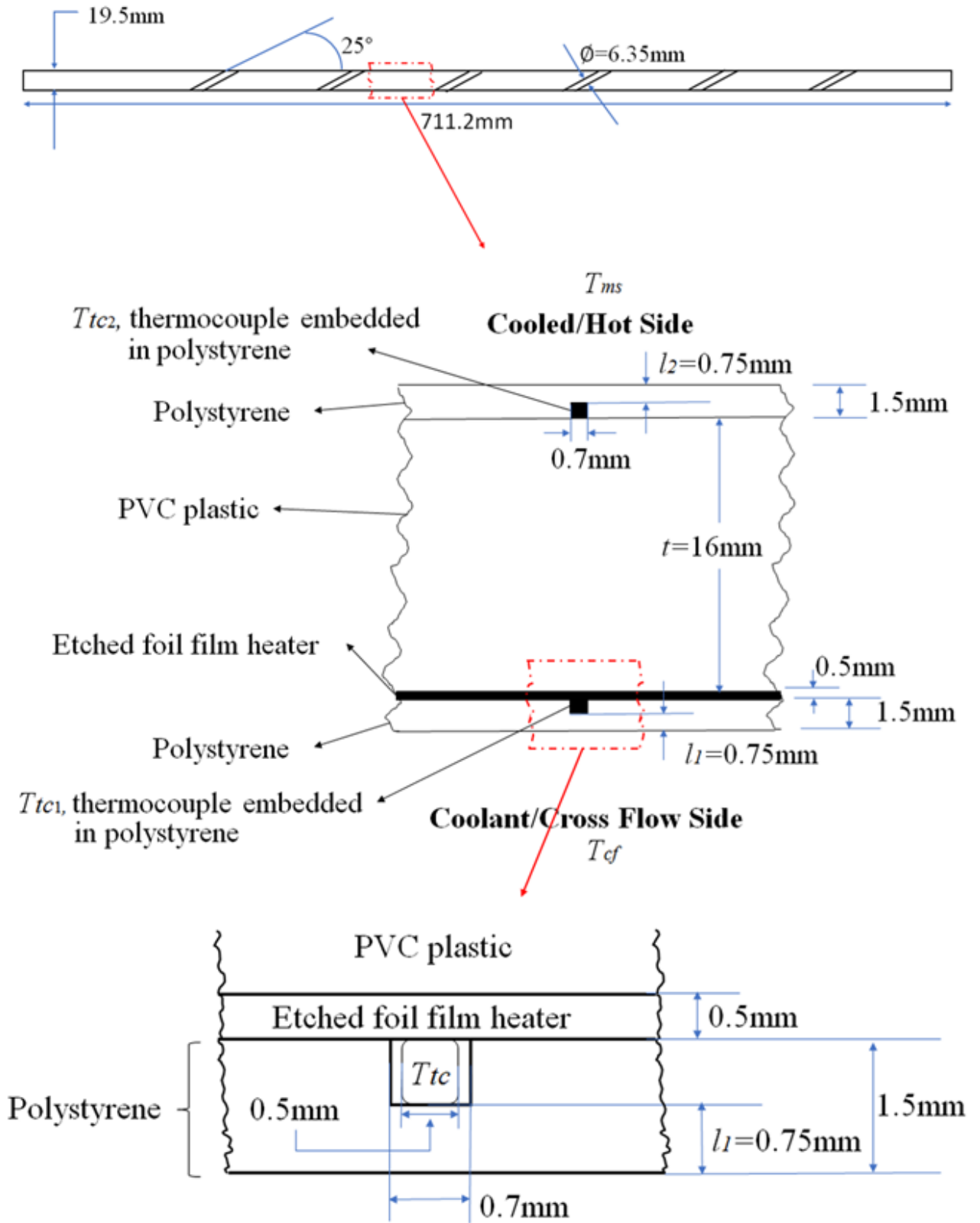


Figure 3: Dimensions and layout of different layers of the effusion test plate.

2.4 Measurement of Flow Temperatures and Pressures

The same thermocouples are used throughout the experiment. The thermocouples used are Omega 5TC-TT-T40-72 fine-wire copper-constantan (Type T) thermocouples. Three thermocouples are located in the mainstream, with the junctions parallel to the flow. A similar setup is employed in the cross flow. Two thermocouples are located in the impingement plenum parallel to the airflow. The test plate has 6 embedded thermocouples on the main flow side, and another 6 embedded on the coolant supply side. All thermocouples are connected to a National Instruments 9213 thermocouple card that resides in a National Instruments cDAQ-9188.

Pressure measurements are conducted with static pressure taps and Keil probes. Where probes are used, they are positioned in the centerline of the flow in x and y directions. Kiel probes are United Sensor Corporation KCC-8 Kiel probes. Probes and taps are connected to Validyne DP15 differential pressure transducers, which are in turn connected to Validyne CD15 Carrier Demodulators. A 100-microfarad capacitor is placed across the output terminals of the carrier demodulator to reduce noise. Due to different pressure ranges, the pressure transducers use varying internal diaphragms, selected to best suit the particular needs of that pressure transducer. Data are recorded to a lab computer using a National Instruments NI USB-6210 data acquisition card.

2.5 Impingement Flow Conditions and Parameters Determination

The mass flow rate of the impingement air is determined from measurements of pressures and temperatures, relative to the ASME standard orifice plate located within the connecting pipe between the first and second upstream plenums. Associated equations are solved in an iterative fashion to obtain values of spatially-averaged pipe velocity, and impingement air mass flow rate \dot{m}_i . Centerline pipe velocity is also measured upstream of the orifice plate, using a total Kiel probe pressure and the local surface static pressure within the pipe. Resulting values are compared with spatially-averaged pipe velocity, as a verification of mass flow rate measurement, with centerline values 15 to 30 percent higher than spatially-averaged values.

Since the impingement plenum cross sectional area is much larger than the area of the impingement test plate holes, the air in the impingement plenum is nearly stagnate. As a result, plenum thermocouples and wall static pressure taps provide impingement stagnation temperature, and impingement stagnation pressure, $T_{t,i}$ and $P_{t,i}$. The impingement jet spatially-averaged velocity

for an individual impingement jet hole exit V_i is determined using the impingement air mass flow rate, determined for an individual impingement hole. This requires an iterative solution procedure, wherein values of V_i , impingement air static density $\rho_{s,i}$, and impingement air static temperature $T_{s,i}$ are determined simultaneously.

2.6 Cross Flow Conditions and Parameters Determination

Cross flow static temperature $T_{s,cf}$ is determined from measurements using a thermocouple located near the entrance of the cross flow supply channel. Cross flow static density $\rho_{s,cf}$ is determined using $T_{s,cf}$ and $P_{s,cf}$, which is measured using wall static pressure taps, located near the entrance of the cross flow supply channel. Stagnation pressure $P_{t,cf}$ is measured by a total Kiel probe, also near the entrance of the cross flow supply channel. Spatially-averaged cross flow inlet supply velocity V_{cf} , and cross flow inlet static density $\rho_{s,cf}$ are then determined from these measured quantities. The resulting cross flow entrance mass flow rate is then given by

$$\dot{m}_{cf} = \rho_{s,cf} A_{cf} V_{cf} \quad (1)$$

The associated Reynolds number is then determined using an equation of the form

$$Re_{cf} = \frac{\rho_{s,cf} V_{cf} D_{Hcf}}{\mu_{cf}} \quad (2)$$

2.7 Film Cooling Flow and Main Flow Conditions and Parameters Determination

The overall mass flow rate of the effusion coolant is the sum of the cross flow mass flow rate and impingement mass flow rate, as given by

$$\dot{m}_e = \dot{m}_{cf} + \dot{m}_i \quad (3)$$

The stagnation temperature for the effusion coolant $T_{t,e}$ is determined as a mass weighted average of cross flow stagnation temperature and impingement flow stagnation temperature. The local static density, $\rho_{s,e}$ and spatially-averaged static density $\rho_{s,e,AvG}$ are determined using ideal gas equations. For this determination, $P_{s,e}$ is the effusion hole exit static pressure, which is determined

near the exit of each effusion hole row using a sixth-order polynomial equation, determined from main stream static pressure measurements along the main flow channel.

Spatially-averaged effusion Reynolds number and Mach number are given as

$$Re_e = \frac{\rho_{s,e,Avg} V_{e,Avg} d_e}{\mu_e} \quad (4)$$

and

$$M_{e,Avg} = \frac{V_{e,Avg}}{\sqrt{\gamma R T_{s,e,Avg}}} \quad (5)$$

respectively. A spatially-averaged discharge coefficient is then determined using an equation of the form

$$C_d = \frac{\rho_{s,e,Avg} V_{e,Avg}}{(\rho_{s,e,Avg} V_{e,Avg})_{ideal}} = \frac{\rho_{s,e,Avg} V_{e,Avg}}{\sqrt{2 \rho_{s,e,Avg} (\Delta P_{e,Avg})}} \quad (6)$$

where ΔP_e is difference between the inlet stagnation pressure, $P_{t,e}$, measured within the cross flow channel, and the static pressure at the exit of each effusion hole row, $P_{s,e}$, measured within the main flow passage. Values of ΔP_e at each effusion hole exit are then averaged to determine $\Delta P_{e,Avg}$.

Local freestream static temperature $T_{s,ms}$, and local freestream stagnation temperature $T_{t,ms}$ are determined from thermocouple measurements of air flow recovery temperature near the entrance of the main flow channel test section. Local freestream streamwise velocity V_{ms} , and local freestream static density $\rho_{s,ms}$ are determined using an iterative solution, where V_{ms} is given as

$$V_{ms} = V_{ms,Local} = \sqrt{\frac{2 \Delta P_{ms,Local}}{\rho_{s,ms,Local}}} \quad (7)$$

Within this last equation, $\Delta P_{ms,Local} = P_{t,ms} - P_{s,ms,Local}$, where $P_{t,ms}$ values are measured by total Kiel probe near the entrance of the main stream channel. $P_{s,ms,Local}$ is equal to $P_{s,e}$, which is calculated near the exit of each effusion hole row, using a sixth-order polynomial equation, determined from main stream static pressure measurements along the main flow channel. Local

freestream static density $\rho_{s,ms}$ is determined using the appropriate ideal gas equation. Note that local values given by Eqn. (7) are determined for the inlet of the main flow passage and near the exit of each effusion hole row.

$\Delta P_{ms,Avg}$ and $\rho_{s,ms,Avg}$ are determined as the average values of ΔP_{ms} and $\rho_{s,ms}$ along the length of the main flow test section, from measurements near the exit of each effusion hole row. $V_{ms,Avg}$ is then given by

$$V_{ms,Avg} = \sqrt{\frac{2\Delta P_{ms,Avg}}{\rho_{s,ms,Avg}}} \quad (8)$$

Mainstream Reynolds numbers, $Re_{ms,Avg}$ and Re_{ms} are subsequently calculated using

$$Re_{ms,Avg} = \frac{\rho_{s,ms,Local} V_{ms,Avg} DH_{ms}}{\mu_{ms}} \quad (9)$$

$$Re_{ms} = \frac{\rho_{s,ms,Local} V_{ms,Local} DH_{ms}}{\mu_{ms}} \quad (10)$$

With this approach, $Re_{ms,Avg}$ is calculated based on the average variation of mean mainstream velocity through the main flow test section. Re_{ms} is calculated based on the inlet mean mainstream velocity within the main flow test section. $\rho_{s,ms,Local}$, DH_{ms} , and μ_{ms} within Eqns. (9) and (10) are determined based upon values at the inlet of the main stream test section.

The equation for local effusion hole exit blowing ratio is then given by

$$BR = BR_{e,Local} = \frac{\rho_{s,e} V_{e,Local}}{\rho_{s,ms,Local} V_{ms,Local}} \quad (11)$$

When $BR_{e,Local}$ varies along the length of the main flow test section, values at the inlet of the test section are employed to characterize associated data. Effusion velocity ratio, density ratio, and momentum flux ratio are then given by

$$VR = \frac{V_{e,Local}}{V_{ms,Local}} \quad (12)$$

$$DR = \frac{\rho_{s,e}}{\rho_{s,ms,Local}} \quad (13)$$

$$I = BR * VR \quad (14)$$

Note that values of VR , DR , and I from Eqns. (12), (13), and (14) for the inlet of the test section are also employed to characterize associated data, when these parameters vary significantly along the length of the main flow test section.

2.8 Measurement of Surface Heat Transfer Coefficient and Adiabatic Wall Temperature Distributions - Main Flow Passage - Hot Surface of Effusion Plate

For the mainstream flow side of the effusion plate, a transient approach is utilized to measure spatially-resolved distributions of adiabatic surface temperature (which is used to determine adiabatic film cooling effectiveness), and heat transfer coefficients. Additional details are provided by Rogers et al. (2016).

To obtain the present data, the infrared radiation emitted by the film cooled interior surface of the channel is captured using a FLIR Systems Inc. ThermoVision® T650sc Infrared Camera (S/N 22700776), which operates at infrared wavelengths from 7.5 μm to 13.0 μm . This camera is operated with a FLIR T197915 80 degree infrared lens. Temperatures, measured using the calibrated, copper-constantan (Type-T) thermocouples distributed along the test surface adjacent to the flow, are used to perform the *in situ* calibrations simultaneously as the radiation contours from surface temperature variations are recorded.

When obtaining data, a sequence of digital images is captured from the infrared camera at a rate of 2 Hz. Each digital image from the infrared camera represents an array of wall temperatures at varying x and y locations for a given time t which is equal to the frame number multiplied by the sampling frequency. Figure 4 shows gray scale contours of an instantaneous infrared camera image for the film cooled, hot-side of the effusion test plate, for louver and effusion cooling with $Re_{ms,avg}=106610$.

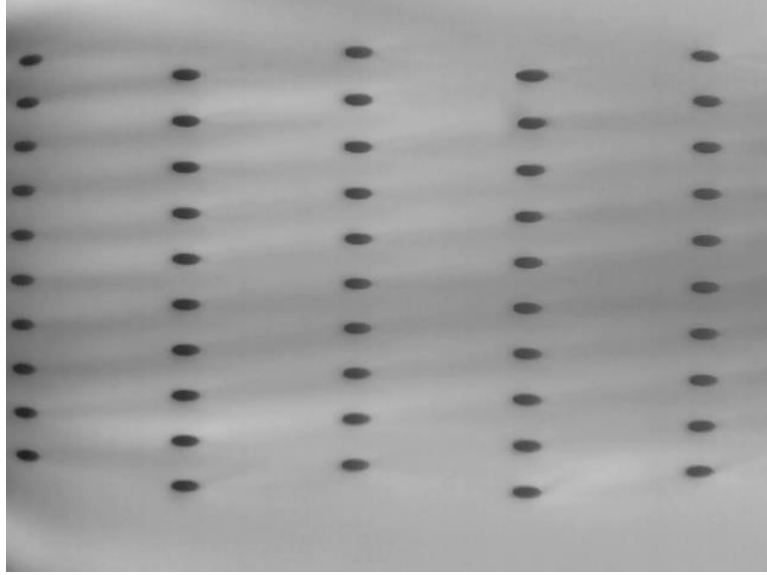


Figure 4: Gray scale contours of an instantaneous infrared camera image for the film cooled, hot-side of the effusion test plate, for louver and effusion cooling with $Re_{ms,avg}=106610$.

The present investigation focuses on measurement of local, and line-averaged adiabatic wall temperatures, adiabatic film cooling effectiveness, and heat transfer coefficients for a range of blowing ratios. These data are produced using a computationally efficient method to reconstruct heat flux from discrete temperature samples taken at some sampling frequency. Note that the procedure assumes that surface heat flux is related to timewise variations of surface temperature by one-dimensional, semi-infinite conduction. Deviations from such behavior (near effusion holes, for example) are accommodated through heat transfer coefficient and film cooling effectiveness uncertainty estimates.

After reconstruction of the heat flux from temperature traces, the heat flux is then plotted against temperature for the time period over which the heater mesh is operating. A linear relationship between the heat flux and wall temperature is expected and observed when using the linear convective heat transfer equation. From the resulting data, the slope has the magnitude of the heat transfer coefficient and adiabatic wall temperature is extrapolated for zero surface heat flux. Measured spatially-resolved distributions of adiabatic surface temperature are then used to determine local values of the spatially-resolved surface effectiveness, using the equation given by

$$\eta = (T_{aw} - T_{s,M}) / (T_{t,C} - T_{s,M}) \quad (15)$$

The heat transfer coefficient is then defined using

$$\dot{q}_0'' = h(T_{aw} - T_{surf}) \quad (16)$$

Line-averaged adiabatic wall temperature and heat transfer coefficient values are determined by averaging the quantity of interest for a row of pixels at constant x/d_e for a range of y/d_e . For the present study, this y range is over a distance of $8.0d_e$.

2.9 Measurement of Surface Nusselt Number Distributions – Impingement / Cross Flow Passage - Cold Surface of Effusion Plate

Liquid crystal thermography is employed to acquire spatially-resolved surface temperature distributions on the coolant side of the effusion plate. Spatially-resolved surface Nusselt numbers are then deduced from these measurements, as well as from measurements of coolant supply temperature, etched foil heater power, and other quantities. A summary of associated apparatus and procedures from Ren et al. (2017) is also given in the section which follows.

A JAI CB-040GE compact digital color progressive scan charge-coupled camera with Navitar Zoom 7000 lens is employed to record and capture liquid crystal images along the test plate. The device is a Bayer mosaic color progressive scan camera with 0.4 million pixels resolution and GigE Vision interface. The camera utilizes the Sony ICX415 CCD and outputs 61 full frames per second in continuous (free-run) mode. The readout mode with full scan for the camera is 776 pixels by 582 pixels. The JAI camera is controlled by the version 2.1.6 of JAI Camera Control software. The Zoom 7000 lens has an effective focal length of 18 to 108 mm, spectral range of 400 to 1000 nm, back focal length of 24.28 mm, and F-stop of 2.5 to close. The outer diameter of the lens filter is 52 mm and the pitch is 0.75 mm. The JAI Camera is used to form a 776 pixel by 582 pixel collection of 24 bit images of the test plate. Resulting images of the test plate are then recorded using the version 2.1.6 of JAI Camera Control Software.

As mentioned, the test plate is mounted on the coolant side of the effusion plate. The locations of thermocouples, which are embedded inside the coolant/cold side of the 1.5 mm polystyrene layer of the test plate, are accurately located within each acquired digital image. During the calibration, temperatures of the liquid crystals are measured using the thermocouples embedded in the coolant/cold flow side of the test plate.

The experimental setup is placed inside of a dark enclosure to provide uniform light and uniform temperature on the test plate, and for improved accuracy of the recorded images. The exposed surface of the polystyrene is coated with micro-encapsulated thermochromic liquid crystals of SPN100-R25C5W of LOT#160419-709-SPN produced by LCR HALLCREST LLC - US. The active range of these liquid crystals is 25⁰C to 30⁰C which is considered to be a wide band of temperature sensitivity. With this arrangement, the red color starts at 25⁰C and the green color ends at 30⁰C. The power level supplied to the thin etched-foil film heater is set so that resulting surface temperature variations are within the liquid crystal temperature bandwidth. As such, the bandwidth is sufficient to capture surface temperature variations, relative to overall temperature differences between the coolant flow coolant and the interior surface of the effusion plate. The test plate surface is painted with SPB100 black backing paint of LOT#151202 from the LCRHallcrest Company. The recorded images of liquid crystals are analyzed using the software program LiquiTherm Image Processor.bat.

To determine surface Nusselt numbers, the power supplied to the etched foil heater is first determined using

$$Q = P = VI \quad (17)$$

Heat power supplied to the coolant flow side of the effusion test plate is then determined by subtracting the heat conduction losses from this measured power value as given by

$$Q_{crct} = Q - \frac{T_{tc1} - T_{ms}}{\frac{2l_2}{k_{pst} * A_{ht}} + \frac{t}{k_{PVC} * A_{ht}}} \quad (18)$$

With this approach, mainstream temperature T_{ms} , is assumed to be uniform. The temperature variation through the 1.5 mm polystyrene layer of the test plate is then determined, so that temperatures of liquid crystals for particular surface thermocouple locations are determined. This approach is then utilized to determine surface temperature values for each pixel of the 760 by 164 digital image array, as given by

$$T_{w_{crct}} = T_{LC} - \frac{Q_{crct} * l_1}{k_{pst} * A_{ht}} \quad (19)$$

The associated cold/cross flow surface convective heat flux is subsequently determined from

$$\dot{q}_0'' = \frac{Q_{crct}}{A_{ht}} \quad (20)$$

From these different measured quantities, local, spatially resolved Nusselt numbers are then determined for each pixel of the 760 by 164 array, using the equation given by

$$Nu = \frac{\dot{q}_0'' d_e}{k(T_{wcrct} - T_{cf})} \quad (21)$$

Within this equation, T_{cf} is then the uniform, mixed-mean temperature at the inlet of the cross flow supply channel.

2.10 Uncertainty Analysis Results

Uncertainty estimates are based on 95 percent confidence levels, and determined using procedures described by Kline and McClintock (1953) and by Moffat (1988). Uncertainty of thermocouple temperature readings is $\pm 0.15^\circ\text{C}$. This uncertainty is dependent upon the thermocouple calibration procedure. Pressure uncertainty is ± 0.25 Pa. This uncertainty is dependent upon the pressure transducer calibration procedure. Spatial and temperature resolutions achieved with the infrared imaging are about 0.2 mm and 0.75°C , respectively. This spatial resolution corresponds to the distance associated with half-spacing between two adjacent pixels within a typical infrared image. This magnitude of temperature resolution is due to uncertainty in determining the exact locations of thermocouples with respect to pixel values used for the *in situ* calibrations. The experimental uncertainty of the blowing ratio is ± 4.0 percent. The experimental uncertainty of the coolant mass flow rate is also approximately ± 4.0 percent, and is primarily due to uncertainty in local coolant velocity. This local coolant velocity value is a result of uncertainty in measured coolant pressure ratio (± 0.8 percent) and uncertainty in the discharge coefficient (± 3.4 percent).

The uncertainty of adiabatic wall temperature is estimated to be $\pm 0.4^\circ\text{C}$. Main flow recovery temperature and coolant stagnation temperature uncertainty is estimated to be $\pm 0.25^\circ\text{C}$. Local surface effectiveness uncertainty is estimated to be ± 0.033 or about ± 8.2 percent for a nominal

effectiveness value of 0.4. Experimental uncertainty magnitudes of line-averaged heat transfer coefficients are ± 8 -10 percent, or approximately ± 4.5 W/m²K for a spanwise-averaged heat transfer coefficient value of 50 W/m²K. These estimates include the influences of radiation and conduction losses and heat transfer to and from the test surface. Uncertainty in the temperature of liquid crystals, calculated from the calibration depends on the uncertainty in hue angle value. The uncertainty magnitude for the surface temperature of liquid crystals ranges from 0.12 to 1.82 degrees, for different magnitudes of surface heat flux. Associated surface Nusselt number uncertainty ranges from 6 to 9 percent.

Chapter 3: Effusion Only Cooling Data with Combination Coolant Supply for the Film Cooled Side of the Effusion Plate

The present chapter provides information on experimental conditions, flow characteristics for different coolant supply arrangements, line-averaged heat transfer coefficient and adiabatic film cooling effectiveness data, and comparisons of line-averaged adiabatic film cooling effectiveness and heat transfer coefficient data.

3.1 Experimental Conditions

The cooling configuration for this chapter is a combination cross flow and impingement coolant supply. The cross flow Reynolds number is approximately constant, in the range of 8400 to 9300. The impingement Reynolds number range is from 6000 to 13000. The main stream Reynolds number range is 145000 to 149000. Presented are the effects of different coolant supply arrangements on surface thermal performance for both sides of the effusion plate. Supply arrangements include a cross flow only arrangement, an impingement jet array arrangement, and a combination cross flow and impingement jet array arrangement. For the effusion cooled/hot surface, presented are spatially-resolved distributions of surface adiabatic film cooling effectiveness, and surface heat transfer coefficients (measured using infrared thermography). For the coolant/cold side, presented are spatially-resolved distributions of surface Nusselt numbers (measured using liquid crystal thermography). These results are given for a range of main flow Reynolds numbers $Re_{ms,avg}$ of 222,000 to 233,000. For this main flow Reynolds number range, four different combination values of crossflow Reynolds number and impingement Reynolds number are tested, which are associated with four different values of initial blowing ratio BR. With this arrangement, crossflow Reynolds number is approximately constant as impingement jet Reynolds number is varied. Table 1 provides experimental conditions.

Table 1: Full-coverage film cooling experimental conditions.

Main Flow					Cross Flow			Impingement Flow		
	V_{ms}	Mass Flow Rate	Re_{ms}	$Re_{ms,avg}$	V_{cf}	Mass Flow Rate	Re_{cf}	V_{imp}	Mass Flow Rate	Re_{imp}
Test	[m/s]	[kg/s]			[m/s]	[kg/s]		[m/s]	[kg/s]	
1	7.58	0.942	149220	232821	0.90	0.041	9200	10.73	0.043	5940
2	7.53	0.937	148281	230528	0.80	0.036	8192	15.53	0.062	8642
3	7.44	0.925	146496	226118	0.83	0.038	8609	18.14	0.073	10162
4	7.41	0.921	145785	221816	0.80	0.037	8355	22.85	0.093	12922
Effusion Flow					Non-Dimensional Parameters					
	V_{ef}	Mass Flow Rate	Mach Number	Re_{ef}	Density Ratio	Velocity Ratio	Momentum Flux Ratio	Blowing Ratio		
Test	[m/s]	[kg/s]			DR	VR	I	BR		
1	36.4	0.084	0.11	15712	1.03	4.9	24.31	5.0		
2	42.7	0.099	0.13	18371	1.03	5.7	34.04	5.9		
3	47.8	0.111	0.14	20601	1.03	6.6	44.37	6.8		
4	55.4	0.130	0.16	23951	1.03	7.7	61.04	7.9		

3.2 Pressure Variations and Flow Characteristics for Different Coolant Supply Arrangements

Figures 5a, b, and c present comparisons of normalized pressure drop variations for the three different coolant supply arrangements: the cross flow only arrangement, the impingement jet array arrangement, and the combination cross flow and impingement jet array arrangement. Included are normalized measurements of: (i) the difference between the cross flow passage static pressure and the mainstream static pressure (Figure 5a), (ii) the difference between the impingement supply static pressure and the mainstream static pressure (Figure 5b), and (iii) the difference between the impingement supply static pressure and cross flow passage static pressure (Figure 5c). For a particular cooling configuration, and for particular values of x/d_e and initial blowing ratio BR, values from Figure 5a (associated with changes from the cross flow passage to the main flow passage) added to values from Figure 5b (associated with changes from the impingement supply plenum to the cross flow passage) give values in Figure 5c (associated with changes from the impingement supply plenum to the main flow passage). Note that the range of initial blowing ratio values are slightly higher for the combination cooling arrangement (relative to the cross flow and impingent jet array configurations), because of extra coolant provided by the combined use of impingement flow and cross flow together.

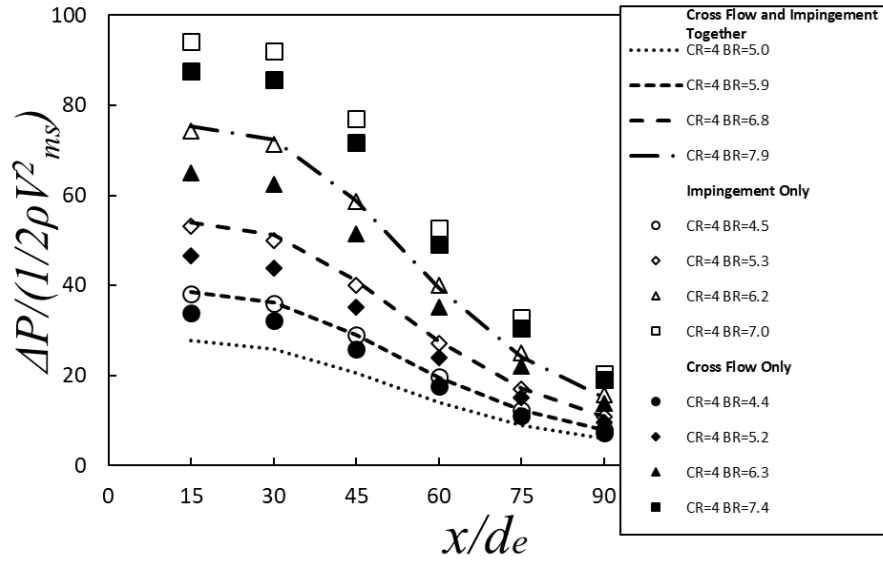


Figure 5a: Comparisons of normalized pressure drop variations between crossflow to mainstream for cross flow and impingement flow together data with CR=4, impingement only data with CR=4, and cross flow only data with CR=4, for mainstream Reynold number values of $Re_{ms,avg}=222000-233000$.

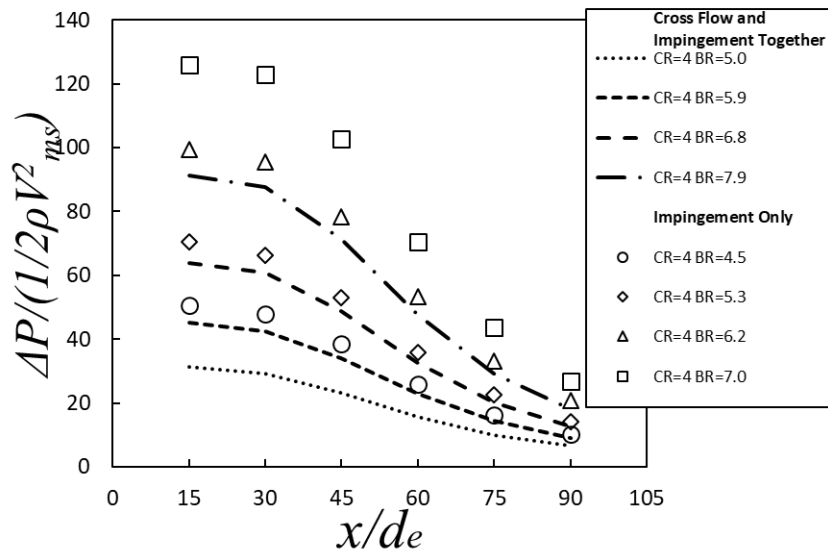


Figure 5b: Comparisons of normalized pressure drop variations between impingement flow to mainstream for cross flow and impingement flow together data with CR=4, and impingement only data with CR=4, for mainstream Reynold number values of $Re_{ms,avg}=222000-233000$.

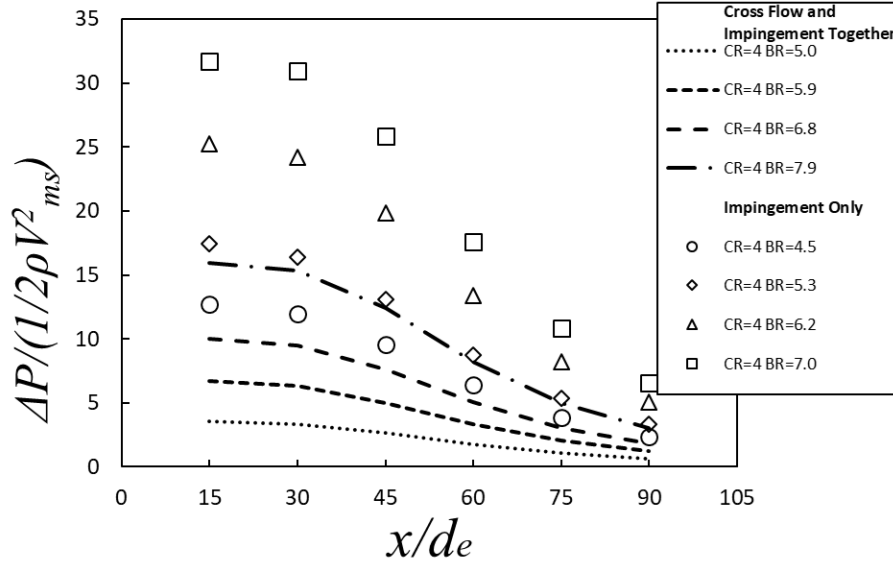


Figure 5c: Comparisons of normalized pressure drop variations between impingement flow to cross flow for cross flow and impingement flow together data with CR=4, and impingement only data with CR=4, for mainstream Reynolds number values of $Re_{ms,avg}=222000-233000$.

Important differences between the three coolant supply arrangements are evident from comparisons of associated results in Figures 5a, b, and c. In all cases, $\Delta P/(1/2 \rho V_{ms}^2)$ decreases with streamwise development and increasing x/d_e for a particular cooling configuration and initial blowing ratio BR. This is mostly due to decreases of main stream static pressure P_{ms} with streamwise development, shown in Figure 6a, which results in substantial increases of V_{ms} with streamwise development, shown in Figure 6b. For each film cooling configuration and initial blowing ratio, dimensional pressure drop ΔP values increase with x/d_e . For each cooling configuration and x/d_e location, $\Delta P/(1/2 \rho V_{ms}^2)$ values increase with initial blowing ratio BR for all three internal cooling configurations within Figures 5a-c. Note that overall qualitative trends are similar for all three internal cooling configurations, as $\Delta P/(1/2 \rho V_{ms}^2)$ variations are considered, either as initial blowing ratio BR or streamwise location x/d_e are varied.

The streamwise variations of the acceleration parameter K for CR=4 are shown within Figure 6c. Dramatic streamwise velocity increases with streamwise development are evident as x/d_e increases. Variations of the acceleration parameter, determined using $K=(v/V_{ms}^2)(dV_{ms}/dx)$, then initially increase as x/d_e becomes larger than 15. The decrease with streamwise development, as x/d_e becomes greater than 60, then occurs because of local increases of V_{ms}^2 . K parameter variations associated with the CR=4 arrangement are important because values along a larger

portion of the test surface are greater than 2×10^{-6} , the lower limiting value associated with re-laminarization of the local boundary layer.

Figure then presents effusion hole exit velocity variations, which increase only slightly with x/d_e for each initial blowing ratio BR value. Comparisons of local blowing ratio values with impingement coolant supply, cross flow supply, and combined supply for the same Re_{MS} range with $CR=4$ are given in Figure 8. In all cases, data are given for the test section entrance and for six different effusion hole locations. The local blowing ratio BR increases with increase in the effusion jet Reynolds number. Figure 8 shows that the local blowing ratio decreases with streamwise development and x/d_e , which is mostly due to the local main flow streamwise velocity increase with x/d_e for $CR=4$.

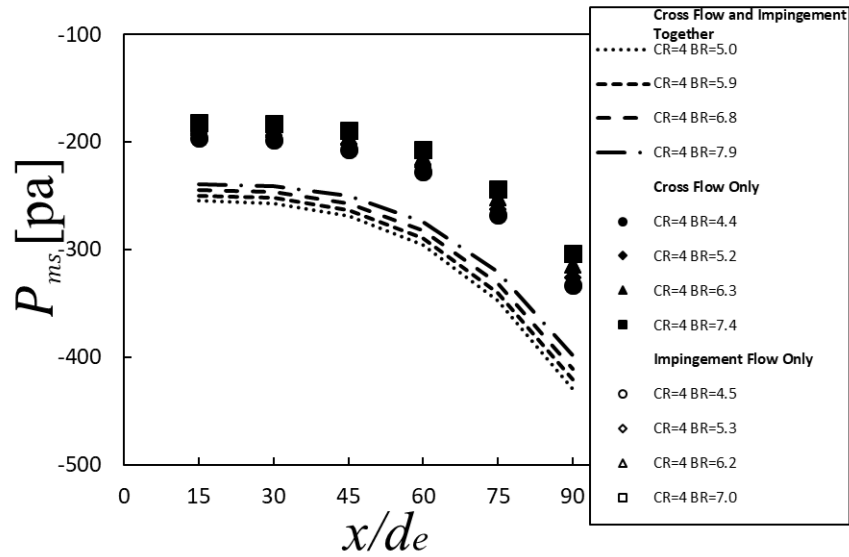


Figure 6a: Comparisons of main stream static gage pressure with $CR=4$ for cross flow and impingement flow together data with $CR=4$, impingement only data with $CR=4$, and cross flow only data with $CR=4$, for mainstream Reynold number values of $Re_{ms,avg}=222000-233000$.

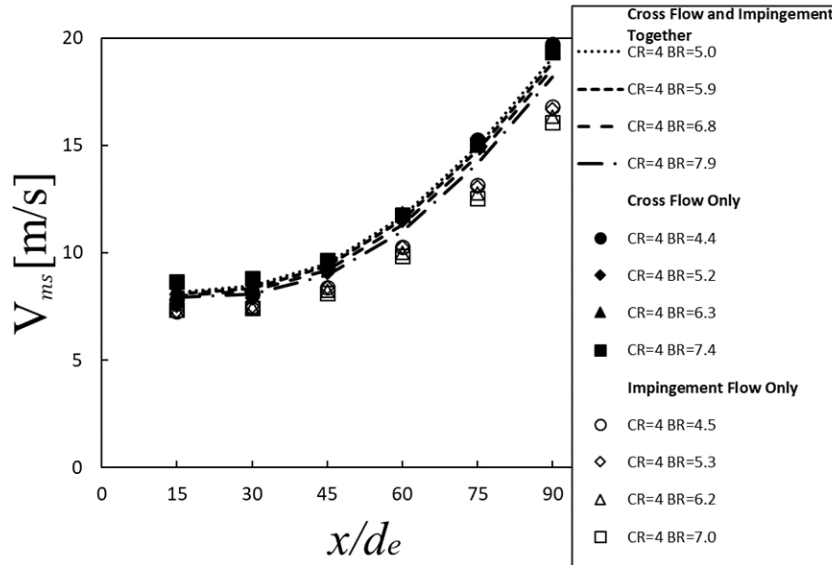


Figure 6b: Comparisons of mainstream velocity variations with CR=4 for cross flow and impingement flow together data with CR=4, impingement only data with CR=4, and cross flow only data with CR=4, for mainstream Reynold number values of $Re_{ms,avg}=222000-233000$.

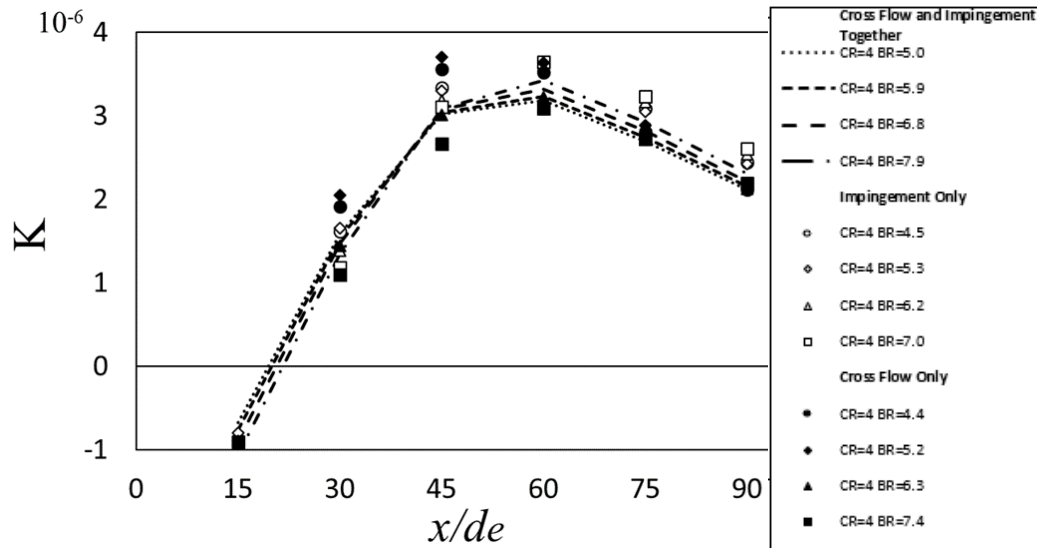


Figure 6c: Streamwise variations of local flow acceleration parameter with cross flow and impingement flow together data with CR=4, impingement only data with CR=4, and cross flow only data with CR=4, for mainstream Reynold number values of $Re_{ms,avg}=222000-233000$.

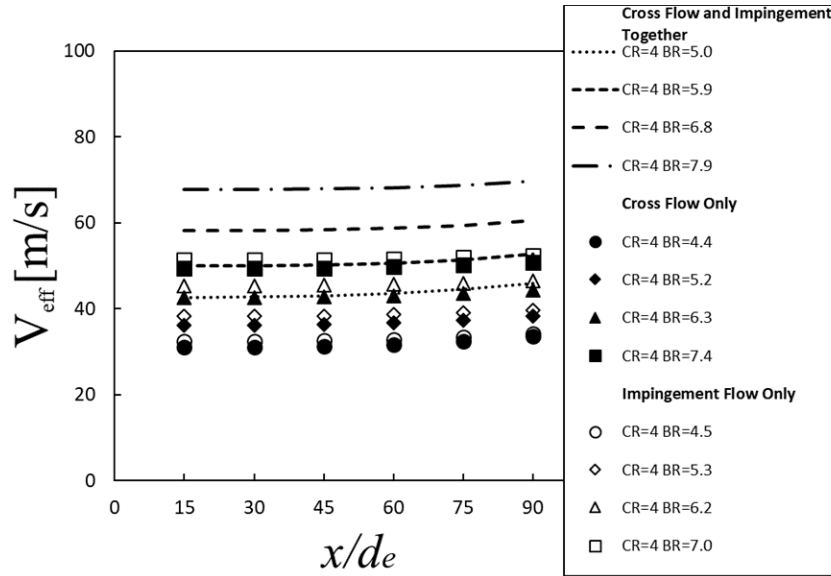


Figure 7: Comparisons of effusion hole exit velocity variations with CR=4 for cross flow and impingement flow together data with CR=4, impingement only data with CR=4, and cross flow only data with CR=4, for mainstream Reynold number values of $Re_{ms,avg}=222000-233000$.

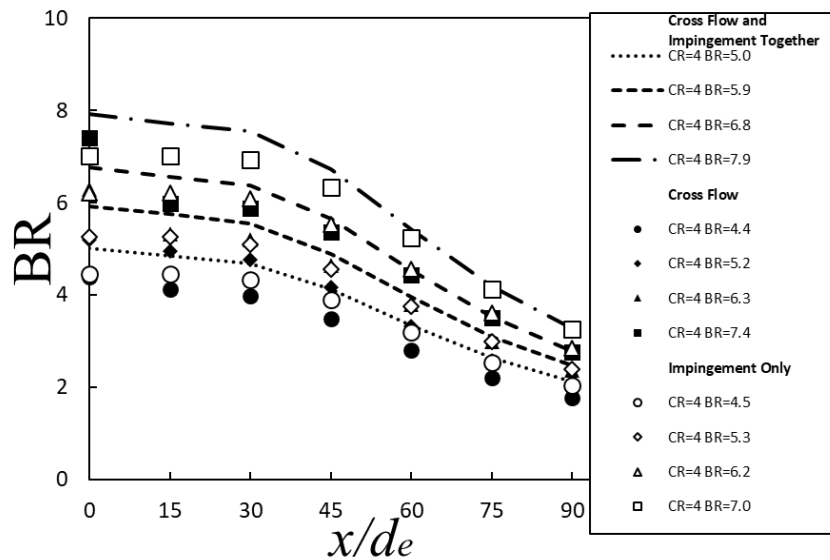


Figure 8: Comparisons of local blowing ratio with CR=4 for cross flow and impingement flow together data with CR=4, impingement only data with CR=4, and cross flow only data with CR=4, for mainstream Reynold number values of $Re_{ms,avg}=222000-233000$.

3.3 Line-Averaged Hot-Side Data for the Combination Cross Flow and Impingement Jet Array Arrangement

Line-averaged heat transfer coefficient data for cross flow cooling and impingement jet array cooling together are presented in Figure 9 as they vary with x/d_e . Data for each initial BR value show local gradient variations near each effusion hole location, which are positioned at x/d_e of 15, 30, 45, 60, and 75. Line-averaged coefficients increase across each of these gradients, as a result of augmented shear and turbulent mixing from the presence of effusion jets. Values also increase at each x/d_e location with initial blowing ratio BR, which are associated with increases of the impingement jet Reynolds number and increased turbulent mixing and thermal transport.

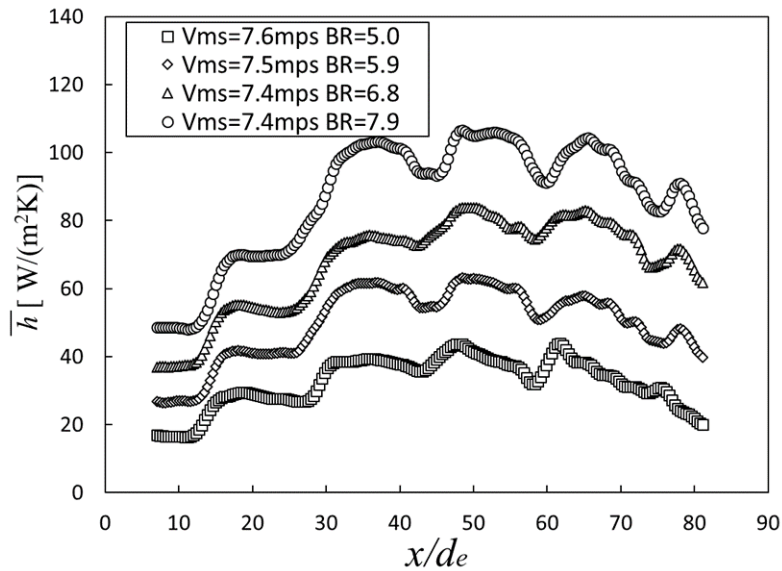


Figure 9: Hot-side line-averaged heat transfer coefficient variations with normalized streamwise location for different values of initial blowing ratio for cross flow and impingement flow together data with CR=4 for mainstream Reynold number values of $Re_{ms,avg}=222000$ to 233000 .

Important heat transfer coefficient decreases with streamwise development are evident in Figure 9 (for each initial value of blowing ratio BR), especially as x/d_e becomes greater than 60. Locally lower BR values, shown in Figure 8, are responsible, along with pronounced streamwise acceleration along the main flow test section. As indicated, this acceleration is characterized by acceleration parameter K values greater than 2×10^{-6} (shown in Figure 6c), which generally leads to stabilization of boundary layer turbulence, along with a trend of local re-laminarization.

Line-averaged adiabatic film cooling effectiveness data for the same configuration and experimental conditions are given in Figure 10, also as they vary with x/d_e location, for different

initial BR values. Because increasing amounts of coolant are generally spread along the test surface as initial blowing ratio BR increases, line-averaged adiabatic film cooling effectiveness values often increase with BR at each x/d_e location. Also important are sequential increases of $\bar{\eta}$ with streamwise development, which are due to accumulations of effusion coolant along the test surface. Such accumulations are especially pronounced near effusion hole row locations, where $\bar{\eta}$ distributions often show local maximum behavior. In most cases, coolant accumulations with x/d_e location are so pronounced that they offset the effects of local BR variations, as well as main flow acceleration. The most pronounced exception to this trend within Figure 10 is associated with BR=5.0 data, wherein substantial $\bar{\eta}$ decreases with x/d_e are apparent, as x/d_e location becomes greater than 65.

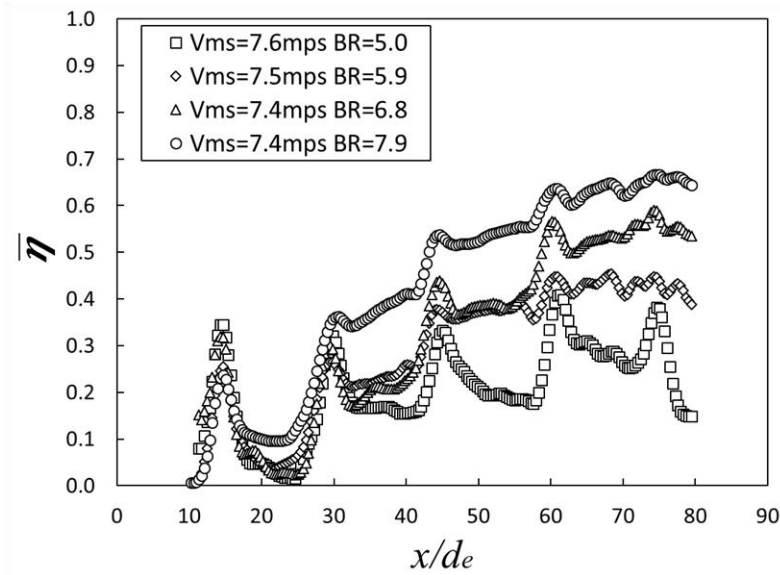


Figure 10: Hot-side line-averaged adiabatic film cooling effectiveness variations with normalized streamwise location for different values of initial blowing ratio for cross flow and impingement flow together data with CR=4 for mainstream Reynold number values of $Re_{ms,avg}=222000-233000$.

3.4 Line-Averaged Hot-Side Adiabatic Film Cooling Effectiveness Data for Different Coolant Supply Arrangements

Variations of line-averaged adiabatic film cooling effectiveness with BR are given in Figure 11 for $x/d_e=30$ and in Figure 12 for $x/d_e=80$. Compared in each of these figures are data for cross flow and impingement flow together, impingement only data from Vanga et al. (2018), and cross flow only data from Allgaier et al. (2018).

Data for $x/d_e=30$ are selected for comparison within Figure 11 because they are representative of effusion cooling behavior for the second streamwise row of holes. Here, the lowest line-averaged effectiveness magnitudes, with magnitudes of 0.15 and lower, are generally produced by the cross flow only arrangement. Values associated with combination cross flow/impingement are then somewhat higher, showing a slightly increasing trend with BR, as BR values exceed 6.0. Figure 11 also shows that the highest effectiveness values are produced by the impingement only configuration, provided BR values exceed 6.0. The impingement only arrangement is also advantageous because of substantial $\bar{\eta}$ increases with BR, as BR values exceed 5.0.

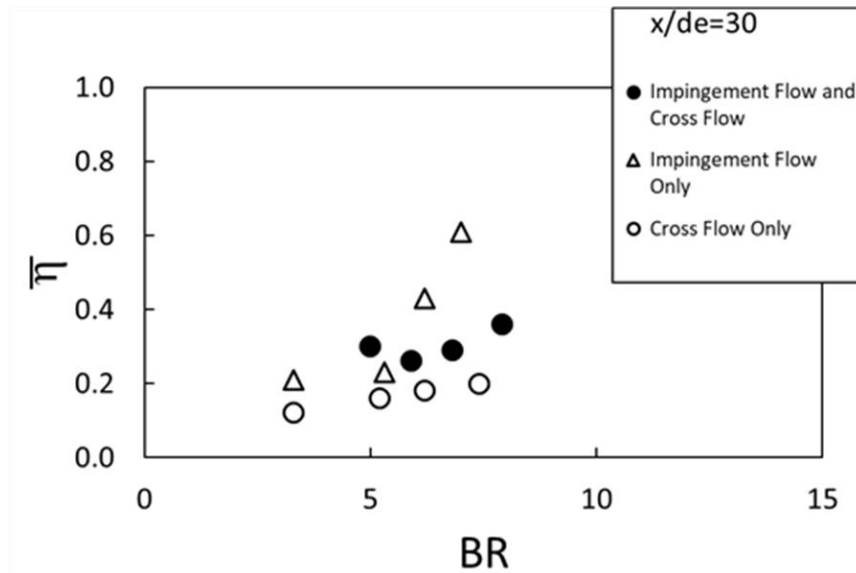


Figure 11: Hot-side line-averaged adiabatic film cooling effectiveness variations with initial blowing ratio for $x/d_e=30$ and $Re_{ms,avg}=222000-233000$, including comparisons with impingement only data and cross flow only data.

Figure 12 presents data for comparison at $x/d_e=80$ because they are representative of effusion cooling downstream of the fifth streamwise row of holes, near the downstream edge of the test surface. An important feature of the data within this figure is similar $\bar{\eta}$ values for all three different coolant supply arrangements, which are largely invariant with blowing ratio, for BR values less than or equal to 5.0. When BR values are greater than 5.0, data trends with initial blowing ratio BR in Figure 12, for the impingement only data and for the cross flow only data, are qualitatively similar to variations in Figure 11. Substantially different qualitative data trends are evident relative to Figure 11, in regard to the cross flow/impingement combination configuration. For this cooling arrangement, Figure 12 shows that $\bar{\eta}$ data associated with the cross flow/impingement combination configuration increase dramatically with blowing ratio, as BR values exceed 5.0. Such values

illustrate excellent effusion coverage along and near to the test surface, at larger downstream locations, with less adequate near-surface coverage at upstream locations, near and upstream of $x/d_e=30$.

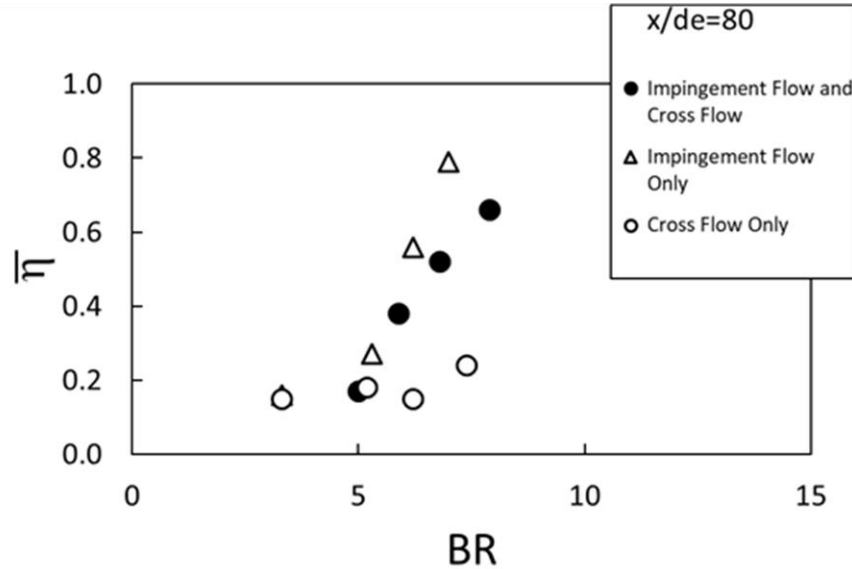


Figure 12: Hot-side line-averaged adiabatic film cooling effectiveness variations with initial blowing ratio for $x/d_e=80$ and $Re_{ms,avg}=222000-233000$, including comparisons with impingement only data and cross flow only data.

Overall, the differences shown by the data in Figures 11 and 12 for the three different coolant supply configurations evidence substantial differences whereby effusion coolant is supplied and enters into the effusion holes by these configurations. These variations in supply then affect distributions of coolant, after it exits individual effusion holes. Of particular importance are the resulting distributions and accumulations of effusion coolant along the test surface. Here, coolant distributions near the test surface are so concentrated that they generally dominate film effectiveness behavior, which in many cases, offsets the influences of main flow streamwise acceleration, as well as the decreases of local blowing ratio which occur with streamwise development.

3.5 Line-Averaged Hot-Side Heat Transfer Coefficient Data for Different Coolant Supply Arrangements

Line-averaged heat transfer coefficient data for different coolant supply arrangements are given in Figure 13 for $x/d_e=35$ and in Figure 14 for $x/d_e=80$. Compared in each of these figures are

data for cross flow and impingement flow together, impingement only data from Vanga et al. (2018), and cross flow only data from Allgaier et al. (2018).

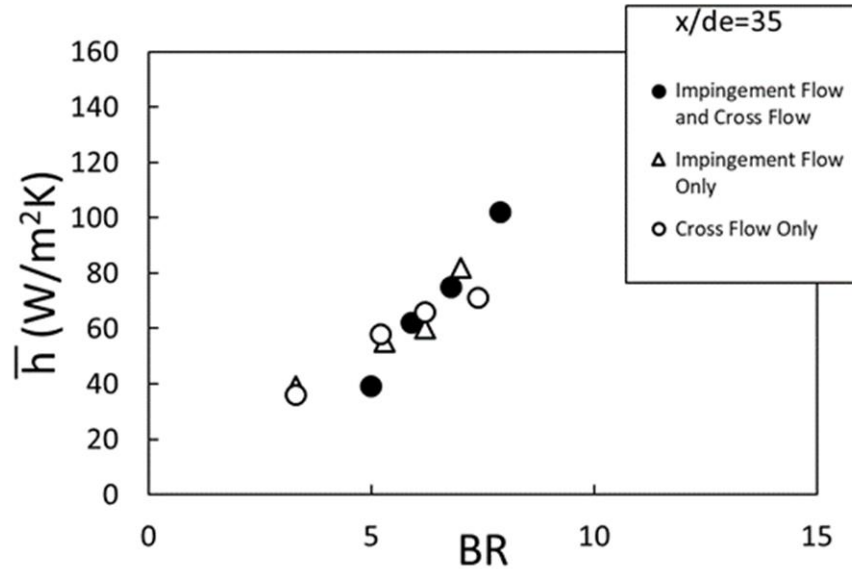


Figure 13: Hot-side line-averaged heat transfer coefficient variations with initial blowing ratio for $x/de=35$ and $Re_{ms,avg}=222000-233000$, including comparisons with impingement only data and cross flow only data.

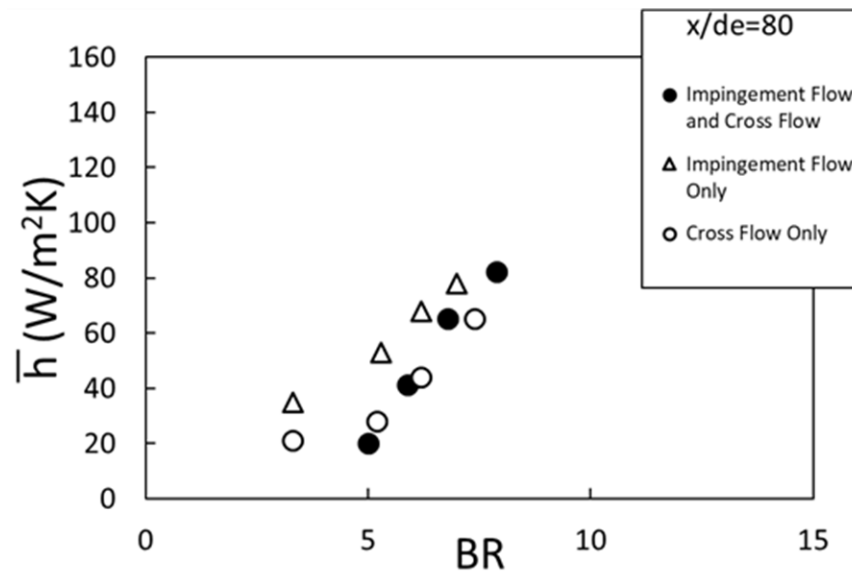


Figure 14: Hot-side line-averaged heat transfer coefficient variations with initial blowing ratio for $x/de=80$ and $Re_{ms,avg}=222000-233000$, including comparisons with impingement only data and cross flow only data.

Every line-averaged heat transfer coefficient data set within Figures 13 and 14 shows a substantial increase with blowing ratio, for all BR values which are considered. When considered

at $x/d_e=80$, and a particular value of initial blowing ratio BR, the lowest \bar{h} values are consistently obtained with the combination cross flow and impingement configuration, and with the cross flow only arrangement. Such differences are related to the shear which develops adjacent to effusion coolant concentrations as they emerge from individual holes, and the associated augmentations of local three-dimensional local mixing and turbulent transport. The emergence and trajectory of effusion coolant concentrations, within and from an individual effusion hole, is then related to the means whereby effusion coolant is supplied and enters into effusion holes by the three different coolant supply configurations.

Comparing the results in Figures 13 and 14 also illustrates the effects of local blowing ratio variations with x/d_e , as well as main flow acceleration. The influences of these phenomena are more pronounced for heat transfer coefficient data, than for film effectiveness data, because the former are more strongly affected by magnitudes and distributions of local turbulent transport. As such, associated influences are illustrated by lower line-averaged heat transfer coefficient values in Figure 14 for $x/d_e=80$, where local blowing ratios are lower and acceleration is stronger, relative to data in Figure 13 for $x/d_e=35$ (provided comparisons are made for the same coolant supply configuration and the same initial blowing ratio).

Chapter 4: Effusion Only Data with a Combination Coolant Supply for the Cross Flow Side of the Effusion Plate

The present chapter provides line-averaged Nusselt number data and comparisons of line-averaged Nusselt number for different cooling supply arrangements. Table 1 provides experimental conditions.

4.1 Line-Averaged Cold-Side Data for the Combination Cross Flow and Impingement Jet Array Arrangement

Line-averaged Nusselt number data for cross flow cooling and impingement jet array cooling together are presented in Figure 15 as they vary with x/d_e , for the cold side of the double-wall test plate. Such results are determined from surface distributions of local, spatially-resolved surface Nusselt numbers. The data in Figure 15 are given for initial blowing ratios of 5.0, 5.9, 6.8, and 7.9, and for main flow Reynolds numbers $Re_{ms,avg}$ of 222000 to 233000. Measured test surface Nusselt numbers within these figures vary from 20 to values as high as 65, and are given for the CR=4 cross flow/impingement combination configuration. Note that dashed rectangles denote impingement hole streamwise locations, whereas solid rectangles denote effusion hole entrance streamwise locations, within Figure 15. Within this figure, the upstream edge of the spatially-resolved measurements is located at $x/d_e=0$.

Regardless of the value of initial blowing ratio BR, results in Figure 15 show that the highest line-averaged Nusselt numbers are often present at smaller x/d_e locations, relative to the locations of the impingement hole centerlines. These locally augmented Nusselt number regions are then often positioned at higher x/d_e locations, relative to effusion hole entrance streamwise locations. As such, evidence is provided of turning and re-direction of the impingement jets, as the jet fluid crosses the cross flow passage. This is because static pressure variations within the cross flow passage induce coolant motion towards and into the entrances of effusion holes. Note that, for the present arrangement, this turning is opposed by the cross flow, whose direction is aligned with the positive x/d_e direction.

As such, associated variations indicate that the impingement jets are more influential in affecting local and line-averaged Nusselt number variations, than the cross flow. Data in Figure 15 evidence such a conclusion since greater impingement jet turning seems to be present at local blowing ratio increases. In addition, when compared for a particular streamwise location x/d_e and

mainstream Reynolds number $Re_{ms,avg}$, line-averaged Nusselt numbers in Figure 15 often increase with initial blowing ratio BR, especially for larger x/d_e values, and especially near impingement jet impact locations. These changes are directly related to increases of the impingement jet Reynolds number, which is directly related to the strength of each individual impingement jet.

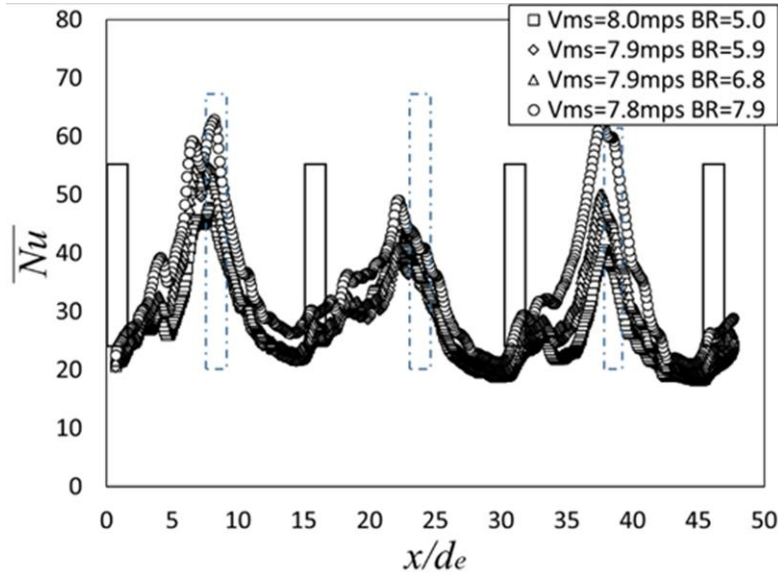


Figure 15: Cold-side line-averaged surface Nusselt number variations with normalized streamwise location for different values of initial blowing ratio for $Re_{ms,avg}=222000-233000$. Solid rectangles denote effusion hole entrance streamwise locations. Dashed rectangles denote impingement hole streamwise locations.

4.2 Line-Averaged Cold-Side Nusselt Number Data for Different Coolant Supply Arrangements

Line-averaged Nusselt number data for the cold side of the double-wall test plate, and for different coolant supply arrangements, are given in Figures 16, 17, and 18 for x/d_e values of 37, 40, and 45, respectively. Compared in each of these figures are data for the CR=4 combination cross flow/impingement configuration, the CR=4 cross flow only configuration from Allgaier et al. (2018), and the CR=4 impingement flow only configuration from Vanga et al. (2018). Data are provided as they vary with initial blowing ratio BR for $Re_{ms,avg}$ of 222000 to 233000.

When compared at a particular BR value, Figures 16, 17, and 18 show that line-averaged Nusselt number are generally highest for the impingement only configuration, and lowest for the cross flow only arrangement. Nusselt number data associated with the cross flow/impingement combination generally increase as BR increases, whereas the cross flow only data increase only slightly with initial blowing ratio. With the exception of one data point, line-averaged Nusselt

number data for the impingement only arrangement generally range between 50 and 73, as initial blowing ratio BR changes.

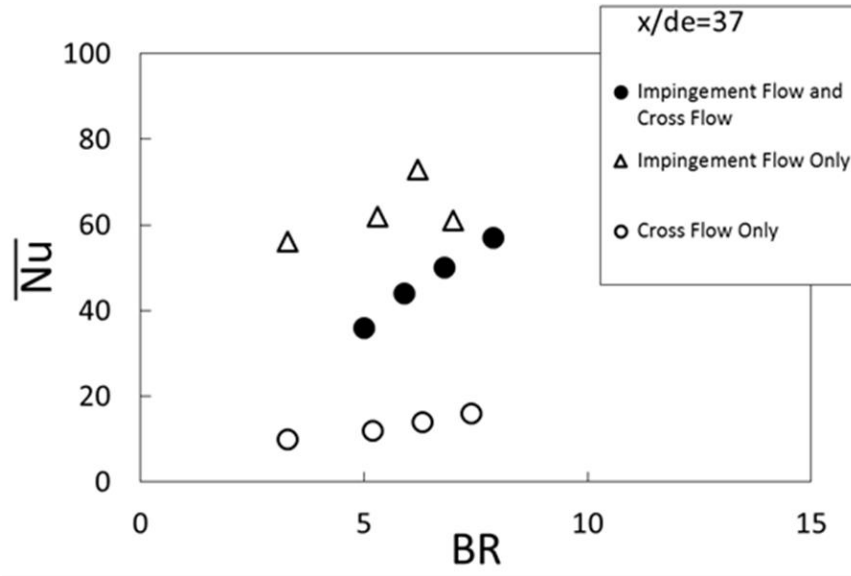


Figure 16: Cold-side line-averaged surface Nusselt number variations with initial blowing ratio for $x/de=37$ and $Re_{ms,avg}=222000-233000$, including comparisons with impingement only data and cross flow only data.

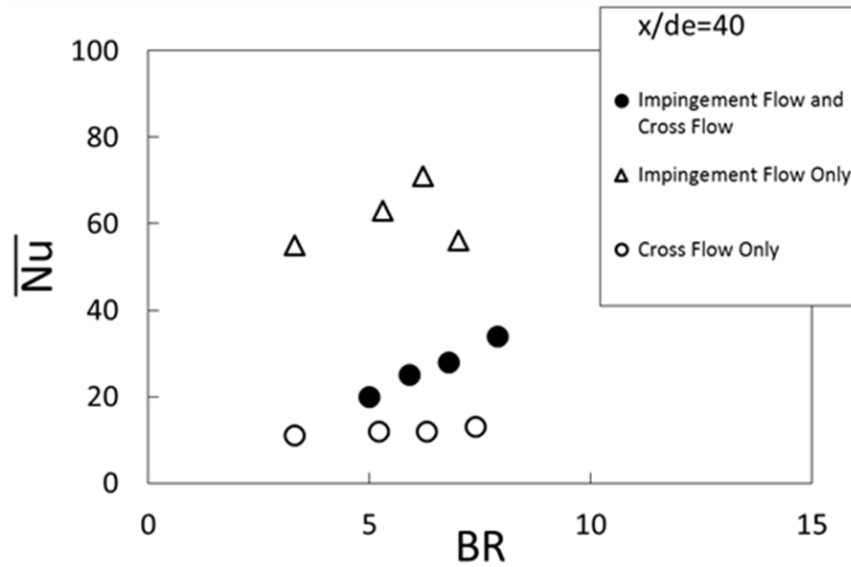


Figure 17: Cold-side line-averaged surface Nusselt number variations with initial blowing ratio for $x/de=40$ and $Re_{ms,avg}=222000-233000$, including comparisons with impingement only data and cross flow only data.

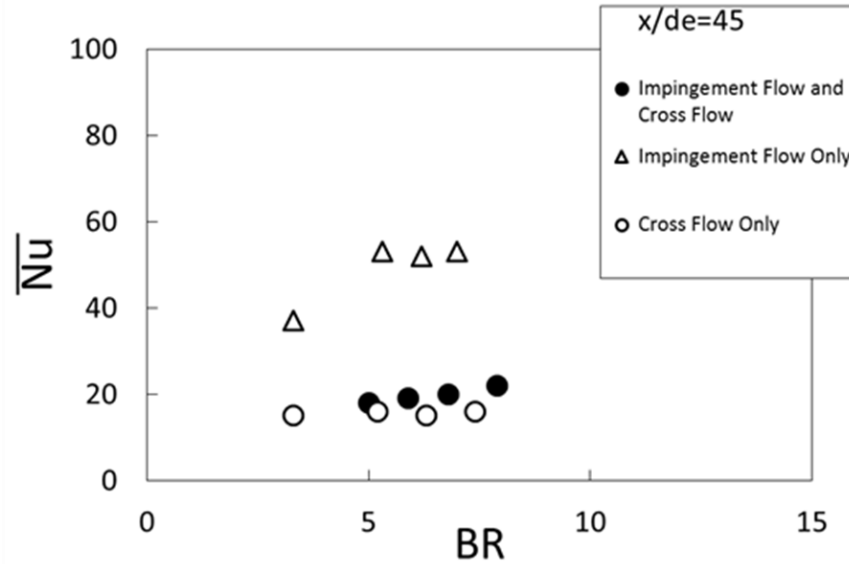


Figure 18: Cold-side line-averaged surface Nusselt number variations with initial blowing ratio for $x/d_e=45$ and $Re_{ms,avg}=222000-233000$, including comparisons with impingement only data and cross flow only data.

Effects of cross flow are illustrated by different line-averaged Nusselt number values at particular BR values within Figures 16, 17, and 18 for the three coolant supply arrangements. Of particular importance are values for the cross flow/impingement combination, which are reduced relative to impingement only magnitudes, for all BR values considered. These reductions become more pronounced for locations between impingement jets ($x/d_e=45$), and less pronounced for locations closer to impingement jet centerlines ($x/d_e=37$).

Chapter 5: Louver and Effusion Combination Cooling with a Combination Coolant Supply Arrangement for the Film-Cooled Side of the Effusion Plate

The present chapter provides information on experimental conditions, test section flow conditions, louver and effusion configuration geometry, local surface adiabatic film cooling effectiveness and surface heat transfer coefficient data, and spanwise-averaged surface adiabatic film cooling effectiveness variations and surface heat transfer coefficient variations data.

5.1 Experimental Conditions

The data within this chapter, and the associated experimental conditions, are given for the combined use of full coverage effusion and louver cooling on the hot side of the effusion test plate. For these data, the coolant is supplied with both cross flow and impingement jets, where in the present arrangement, the cross flow Reynolds number is approximately constant as the impingement jet Reynolds number is varied. The data are given for a main stream Reynolds number range of 107000 to 114000. Experimental conditions for these tests are given in Table 2 and Table 3. Note that louver slot blowing ratios are provided for the spanwise-normal plane at the exit of the louver leap arrangement. Table 4 then provides louver slot cooling effective blowing ratios, which represent values determined with the same overall mass flow rate through an effusion only cooling arrangement. These effective blowing ratios apply to the full-coverage holes, and represent values determined with the same overall film mass flow rates as are present in the full-coverage holes and louver slot together. Such blowing ratio effective values offer another viable means of comparing data obtained with full-coverage holes and louver slots together, with data obtained with full-coverage film cooling holes only.

The experimental conditions illustrated by the data in Table 2 are obtained as the impingement jet Reynolds number is altered, with the cross flow Reynolds number approximately invariant. The range of experimental conditions associated with these tests is relatively small. This is a result of employment of cross flow and an impingement jet array together to supply the coolant. The result is a range of experimental conditions, such as the ones which are given in Table 2. Outside of these conditions, one or the other coolant supply arrangements may act in a non-optimal manner. Such an occurrence is caused by coolant flow from one source which may overwhelm and reverse the coolant flow from the other source. For example, if impingement jet magnitudes are excessive relative to the cross flow, flow from impingement jets may move in the nominal upstream direction

causing the cross flow to reverse. Alternatively, if cross flow magnitudes are excessive relative to the impingement jets, cross flow may enter impingement jet hole exits, resulting in reversal of the nominal impingement flow direction.

Table 2: Film Cooling full-coverage experimental conditions.

Main Flow					Cross Flow			Impingement Flow		
	V_{ms}	Mass Flow Rate	Re_{ms}	$Re_{ms,avg}$	V_{cf}	Mass Flow Rate	Re_{cf}	V_{imp}	Mass Flow Rate	Re_{imp}
Test	[m/s]	[kg/s]			[m/s]	[kg/s]		[m/s]	[kg/s]	
1	5.85	0.717	112298	113656	0.94	0.042	9421	6.29	0.025	3399
2	5.82	0.713	111567	110204	0.95	0.043	9570	8.73	0.034	4729
3	5.75	0.705	110254	107801	0.95	0.043	9560	11.36	0.045	6169
4	5.64	0.690	107986	106610	0.97	0.044	9800	14.09	0.056	7668
Effusion Flow					Non-Dimensional Parameters					
	V_{ef}	Mass Flow Rate	Mach Number	Re_{ef}	Discharge Coefficient	Density Ratio	Velocity Ratio	Momentum Flux Ratio	Blowing Ratio	
Test	[m/s]	[kg/s]			C_d	DR	VR	I	BR	
1	20.7	0.067	0.06	8542	0.70	1.04	3.5	13.03	3.68	
2	23.9	0.077	0.07	9862	0.71	1.04	4.1	17.55	4.28	
3	27.0	0.087	0.08	11194	0.72	1.05	4.7	23.10	4.91	
4	30.7	0.099	0.09	12728	0.74	1.05	5.4	31.01	5.70	
	Blowing Ratio	Main Flow	Cross Flow	Impingement Flow						
	BR	Blower Setting	Blower Setting	Blower Setting						
Test		[Hz]	[Hz]	[Hz]						
1	3.68	33	14	12						
2	4.28	33	17	15						
3	4.91	33	20	18						
4	5.70	33	23	21						

Table 3: Louver slot cooling experimental conditions.

Velocity Ratio	Momentum Flux Ratio	Blowing Ratio	Density Ratio
VR	I	BR	DR
1.6	2.82	1.72	1.04
1.9	3.80	1.99	1.04
2.2	5.00	2.29	1.05
2.5	6.71	2.66	1.05

Table 4: Louver slot cooling effective blowing ratios.

Effusion BR	Louver Slot BR	Effective BR without Louver Slot
3.68	1.72	5.20
4.28	1.99	6.05
4.91	2.29	6.94
5.70	2.66	8.05

5.2 Louver and Effusion Configuration Geometry

The louver slot supply holes, shown in Figure 19, are sized relative to the effusion hole diameter to give dominate louver slot cooling, relative to the moderate thermal protection provided by the array of full-coverage film cooling holes. This is accomplished as the louver slot produces a thick, uniform layer of cooling air along the test surface downstream. The resulting thermal protection is accomplished as this cooling air acts as a thermal insulator and as a heat sink. Based upon relative flow areas, the mass flow rate of the louver flow through 11 holes (each with a diameter of 9.52 mm) is 41.2 percent of the effusion mass flow rate through 60 holes (each with a diameter of 6.35 mm).

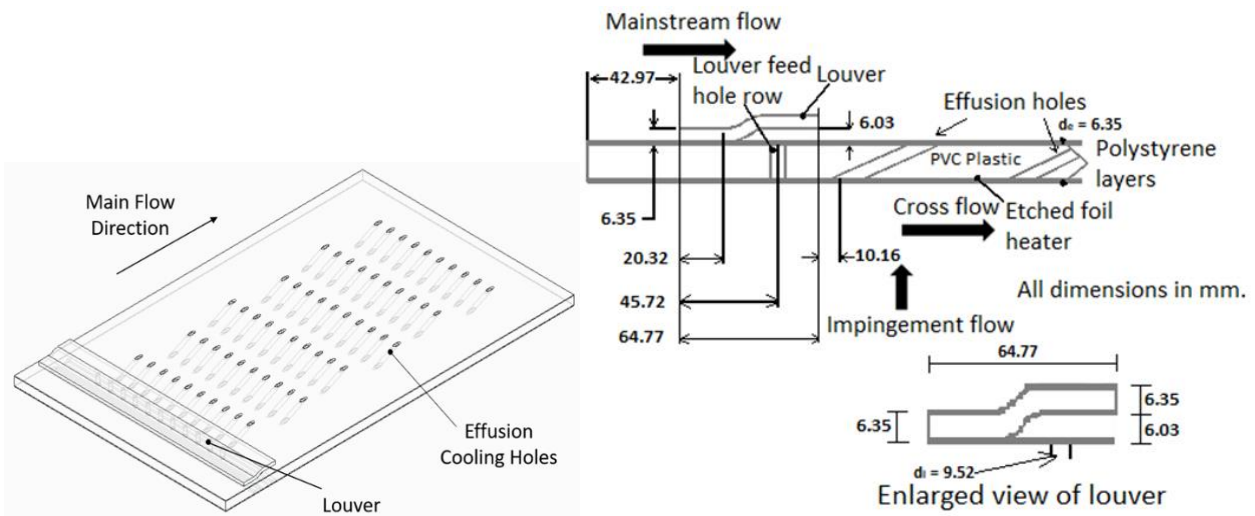


Figure 19: Test section configuration. Left, a three-dimensional view of test plate, including louver slot device and full-coverage film cooling holes. Right, side cross-sectional view of louver slot. All dimensions given in millimeters.

5.3 Test Section Velocity, Pressure, Blowing Ratio, and Discharge Coefficient Variations

Additional understanding of the impingement jet and cross flow coolant supply arrangement is provided by the data in Figure 20. Here, the normalized pressure drop is presented as it varies with blowing ratio for the impingement and cross flow passages, the cross flow and main flow passages, and the impingement and the cross flow passages. These data are presented for a $Re_{ms,avg}$ main flow Reynolds number of 107000 to 114000. Note that the sum of the first two of these pressure drops is equal to the third pressure drop at each blowing ratio considered. Note that all three types of pressure drop increase with blowing ratio. Because coolant air is supplied to the louver feed holes and the effusion holes from the same cross flow passage source, pressure variations associated with the louver alone cannot be determined separately.

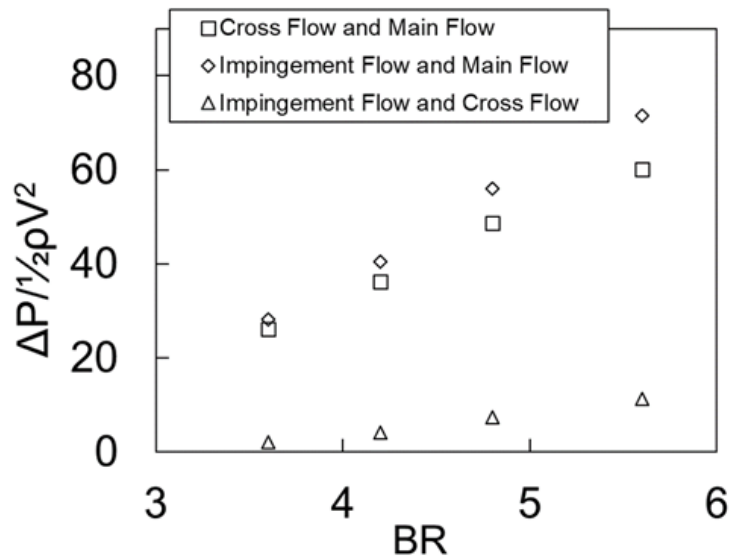


Figure 20: Test section passages pressure drop variations with initial blowing ratio for the louver and full-coverage film cooling configuration and $Re_{ms,avg}=107000$ to 114000 .

The resulting alterations of local main flow freestream velocity and spatially-averaged effusion flow velocity with blowing ratio are then given in Figure 21. Because the test section inlet and outlet areas are the same within the current study, no significant pressure gradient is present in the main flow passage, and the freestream velocity is constant with streamwise position. Figure 21 shows that this freestream velocity is also invariant with blowing ratio. The associated main flow static pressure is also generally invariant with x/de streamwise location and blowing ratio, as

shown in Figure 22. Because the blowing ratio is calculated using the spatially-averaged effusion flow velocity, Figure 21 also shows a linear relationship between the two quantities.

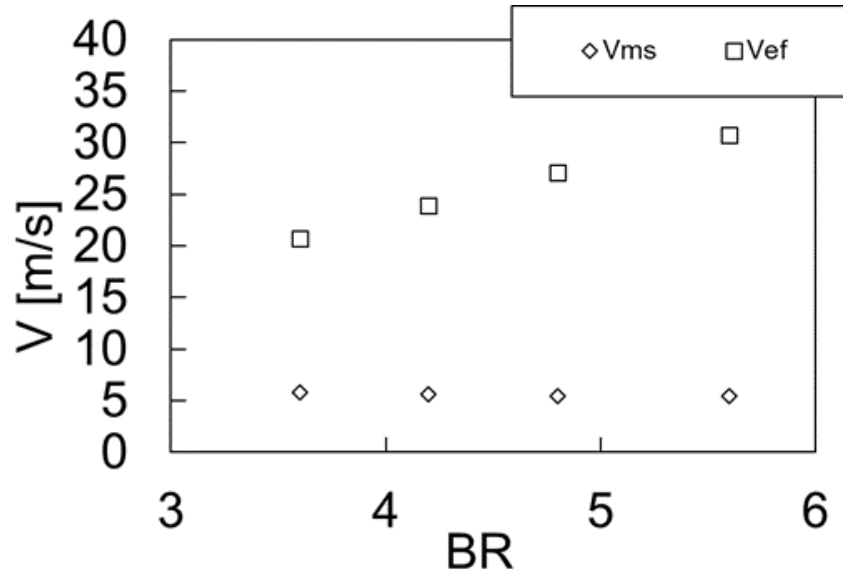


Figure 21: Local main flow freestream velocity and spatially-averaged effusion flow velocity variations with initial blowing ratio for the louver and full-coverage film cooling configuration and $Re_{ms,avg}=107000$ to 114000 .

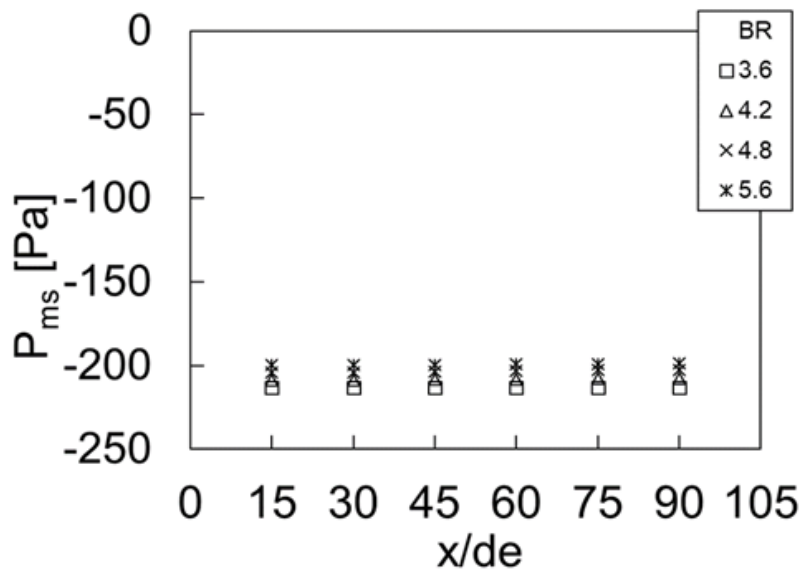


Figure 22: Local main flow static pressure changes with x/de normalized streamwise location for the louver and full-coverage film cooling configuration and $Re_{ms,avg}=107000$ to 114000 .

Figure 23 then presents local blowing ratio changes with normalized streamwise location x/de for different initial blowing ratio values. For each of these initial values, local BR magnitudes are approximately constant with streamwise development as x/de increases. This is, of course, partially

a consequence of the zero streamwise pressure gradient which is present within the main flow passage. The minor BR variations in Figure 23, for every initial blowing ratio value, are thought to be due to small static pressure variations within the coolant supply passage. The discharge coefficient data, shown in Figure 24, are provided for different impingement jet Reynolds numbers, as the cross flow Reynolds number is approximately constant. Note that these data are provided for a wider range of experimental conditions than are tabulated within Table 2. Values increase from 0.70 to 0.77 as Reynolds number, based upon each impingement jet, increases from 3420 to approximately 17000.

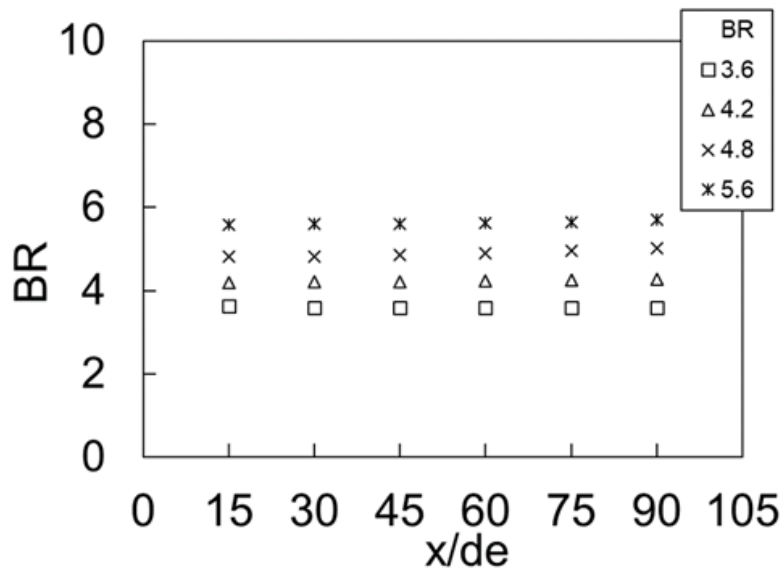


Figure 23: Local blowing ratio changes with x/de normalized streamwise location for the louver and full-coverage film cooling configuration and $Re_{ms,avg}=107000$ to 114000 .

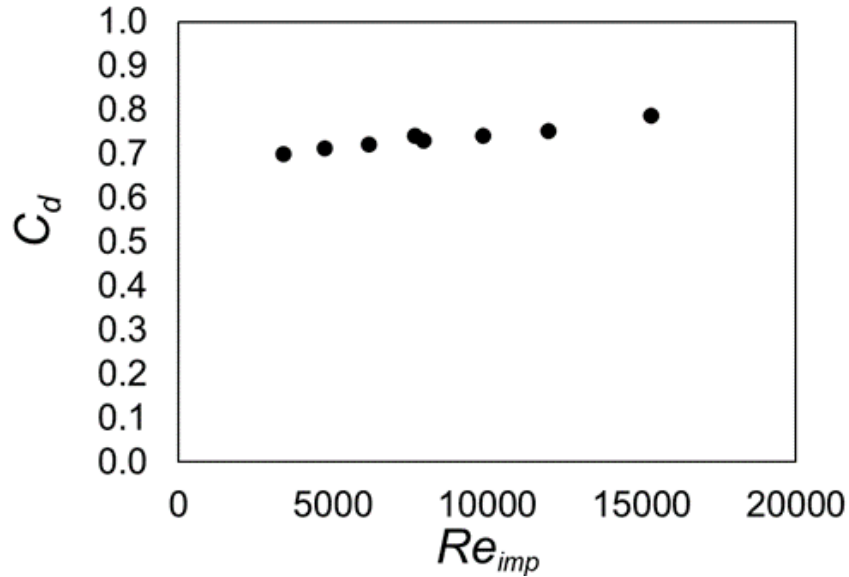


Figure 24: Discharge coefficient changes as impingement jet Reynolds number varies for the louver and full-coverage film cooling configuration and $Re_{ms,avg}=107000$ to 114000 .

5.4 Local Surface Adiabatic Film Cooling Effectiveness and Local Surface Heat Transfer Coefficient Variations

Figure 25 shows the local surface adiabatic film cooling effectiveness distribution. Figure 26 then shows the local surface heat transfer coefficient distribution. Both types of data are provided for the louver and full-coverage film cooling configuration, with an initial blowing ratio BR of 4.91 and a main flow Reynolds number $Re_{ms,avg}$ of 107000 to 114000. Both sets of data evidence influences of the horseshoe vortex which forms near the test surface around each coolant distribution as it emerges from a film cooling hole. The signature of such a three-dimensional vortex is locally augmented values of both heat transfer coefficient and effectiveness. Figure 25 and 26 show that the influences of the coolant jets are often present along the test surface in the vicinity of each film hole exit location, and generally persist for some distance downstream of each hole exit. Present downstream of many film cooling holes are locally increased magnitudes of both effectiveness and heat transfer coefficient, which are shaped in a v-shaped pattern directed in the downstream direction of individual hole exits.

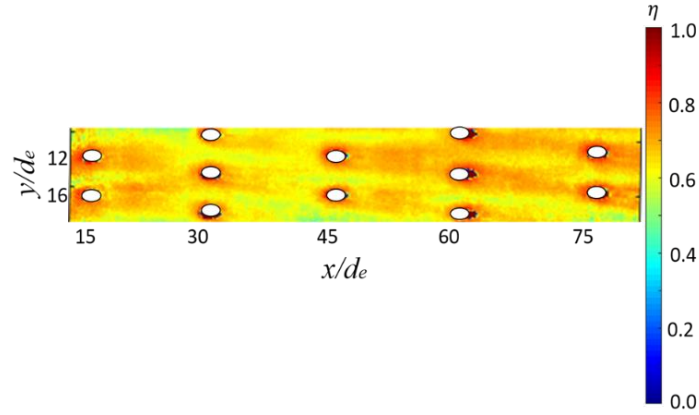


Figure 25: Local surface adiabatic film cooling effectiveness distribution for the louver and film cooling full-coverage configuration for a blowing ratio BR of 4.91 and $Re_{ms,avg}=107000$ to 114000.

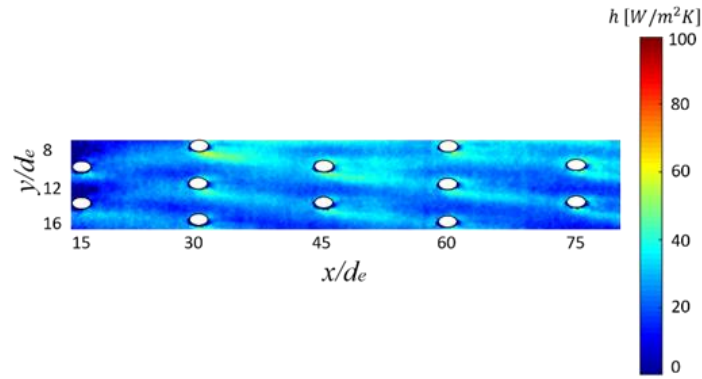


Figure 26: Local surface heat transfer coefficient distribution for the louver and film cooling full-coverage configuration for a blowing ratio BR of 4.91 and $Re_{ms,avg}=107000$ to 114000.

Local heat transfer coefficients associated with the louver and effusion cooling arrangement are compared with effusion cooling local data from Ritchie et al. (2019) in Figure 27. Data in Figure 27a are presented for $y/d_e = 11.5$, with local variations from the existence of film cooling holes which are located at x/d_e values of 15, 45, and 75. Data in Figure 27b are provided for $y/d_e = 13.5$, with local variations from the existence of film cooling holes which are positioned at $x/d_e=30$, and $x/d_e=60$. The most important conclusion from comparisons of the louver and effusion cooling data with effusion cooling only data, is that the presence of the louver is associated with heat transfer coefficient variations with x/d_e , which are generally somewhat smaller as x/d_e changes, and flow advects along the length of the test surface.

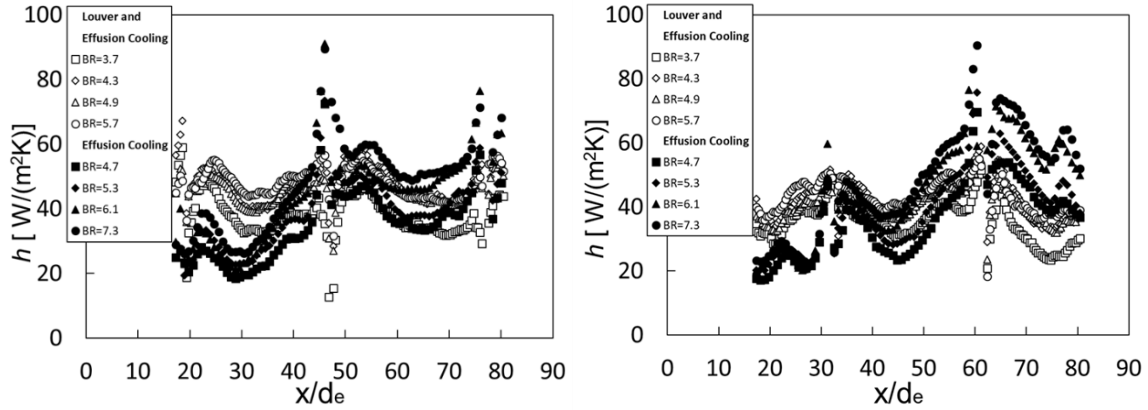


Figure 27: Local heat transfer coefficient comparisons with effusion cooling only local data. Left, louver and effusion cooling data at $y/d_e = 11.5$. Right, louver and effusion cooling data at $y/d_e = 13.5$.

Local adiabatic cooling effectiveness values are compared for the different arrangements for the same y/d_e values in Figure 28. Local variations from the existence of film cooling holes are evident at the same streamwise locations as for the heat transfer coefficient data. Here, dramatic increases of local effectiveness are evident as x/d_e increases for the effusion cooling only arrangement for each blowing ratio experimental condition. In contrast, effectiveness magnitudes for the louver and effusion cooling arrangement show significantly less variation with streamwise development for each blowing ratio value. For this latter configuration, effectiveness values are generally between 0.6 and 0.8 along the entire length of the test plate.

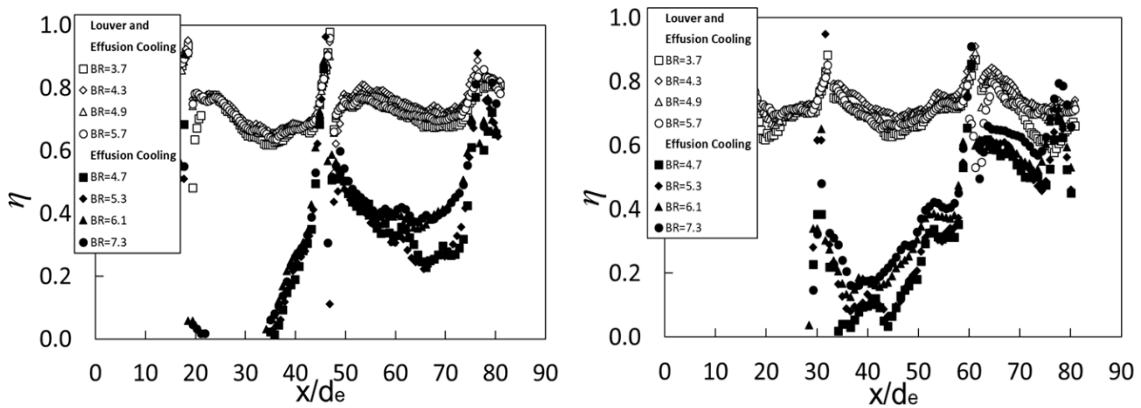


Figure 28: Local adiabatic film cooling effectiveness comparisons with effusion cooling only local data. Left, louver and effusion cooling data at $y/d_e = 11.5$. Right, louver and effusion cooling data at $y/d_e = 13.5$.

5.5 Spanwise-Averaged Surface Heat Transfer Coefficient Variations

Figures 29 to 33 show heat transfer coefficient variations (spanwise-averaged) with streamwise development for different initial blowing ratios for $Re_{ms,avg}=107000$ to 114000 . The first of these figures provides data for the louver and full-coverage film cooling configuration. The remaining figures provide comparisons of results from the effusion cooling only configuration, and from the louver and full-coverage film cooling configuration.

Within Figure 29, spanwise-averaged heat transfer coefficient numbers are relatively low, considering the magnitudes of mainstream Reynolds number, cross flow Reynolds number, and impingement jet Reynolds number which are employed when compared to Ritchie et al. (2019). When examined at a particular x/de location, values are lowest when $BR=3.7$, and then are approximately invariant with blowing ratio for BR values from 4.3 to 5.7. Note that coefficients show only small variations with streamwise development for each blowing ratio BR value. Such variations are associated with the relatively thick and relatively uniform layer of cooling air along the test surface, which is generated by the louver slot. The thermal protection provided by such a layer is tied to its actions as a heat sink and as a thermal insulator. Resulting heat transfer coefficient trends in Figure 29 evidence reduced magnitudes of local turbulent thermal transport, which occurs, in part, because of reduced local advection speeds within the substantial wake which forms downstream of the louver leap configuration.

Comparisons of heat transfer coefficients (which are line-averaged) are provided in Figures 30 and 31 for the effusion cooling only configuration, and for the louver and full-coverage film cooling configuration. These data are also provided for magnitudes of $Re_{ms,avg}$, the main flow Reynolds number, of 107000 to 114000 . The full-coverage film cooling data in these figures are presented for blowing ratio BR initial values of 5.3 and 7.3, respectively. The corresponding louver slot cooling effective blowing ratios (from Table 4) are 5.2 and 6.9, respectively. These effective values result for the combined louver and full-coverage film cooling configuration with effusion and louver slot blowing ratios of 3.7 and 1.7 for the Figure 30 results, and 4.9 and 2.3 for the Figure 31 results. With this comparison, the spanwise-averaged heat transfer coefficients show less variation with streamwise development location, relative to results obtained without a louver employed. In addition, spanwise-averaged heat transfer coefficients are consistently lower, especially for the downstream portions of the test plate, when the louver is utilized. Partially responsible is the blockage provided by the louver leap geometry, which gives a strong wake flow

and relatively low velocity distributions just above the test surface. Also evident from the results given in Figure 30 and 31 are smaller signatures in coefficient variations from the presence of individual rows of film cooling holes (when the louver slot is present). The local coefficient gradients, which are a signature of a row of holes are pronounced for the full-coverage film data in these figures, with variations evident at x/de in the vicinity of 15, 30, 45, 60, and 75. In contrast, variations at the locations with combined louver and full-coverage film cooling are much less evident.

Similar quantitative and qualitative conclusions are reached in regard to the spanwise-averaged heat transfer coefficient data which are given in Figures 32 and 33. Within the first of these figures, data are compared for impingement jet Reynolds numbers of 3399 and 3506. Within the second of these figures, data are compared for impingement jet Reynolds numbers of 7668 and 7418.

Results such as the ones presented in Figures 30 and 31, as well as in Figures 25 and 26, indicate that flow and surface thermal characteristics are very sensitive to the placement, location, and alignment of the louver leap device. Of particular importance are the extent and symmetry between the edges of the device and the nearby side walls within the test section. Small geometric variations have been found to affect measured data in a significant manner, depending upon the experimental conditions which are considered.

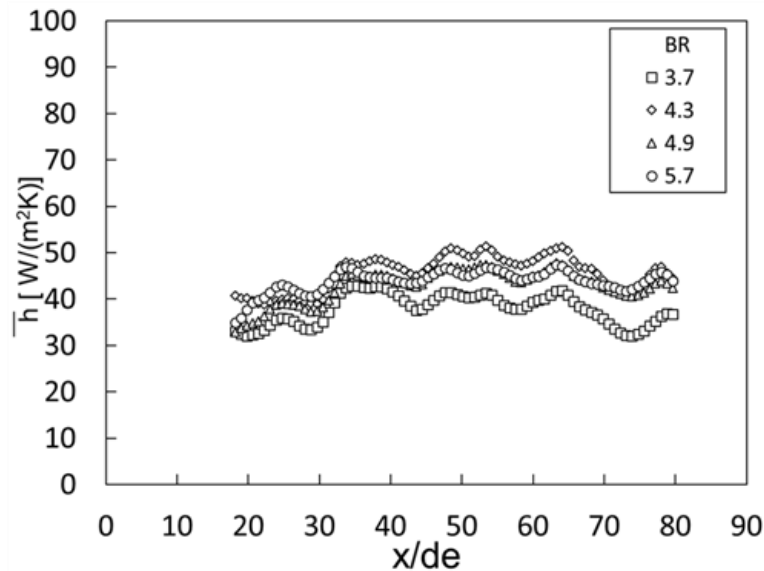


Figure 29: Heat transfer coefficient (spanwise-averaged) variations with x/de , provided at different blowing ratios for the louver and full-coverage film cooling configuration, $Re_{ms,avg}=107000$ to 114000.

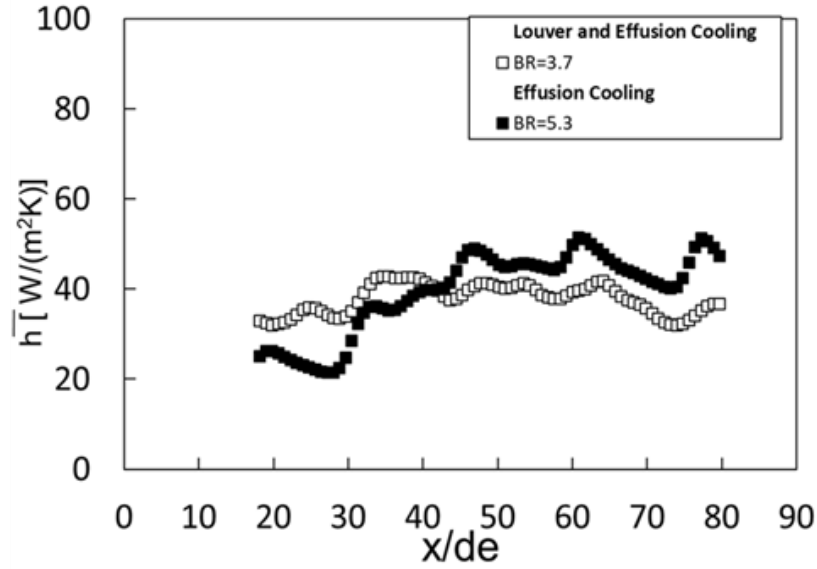


Figure 30: Heat transfer coefficient (spanwise-averaged) variations with x/d_e (at approximately the same effective blowing ratios of 5.2 and 5.3) for the effusion cooling only configuration, and for the louver and full-coverage film cooling configuration, $Re_{ms,avg}=107000$ to 114000 .

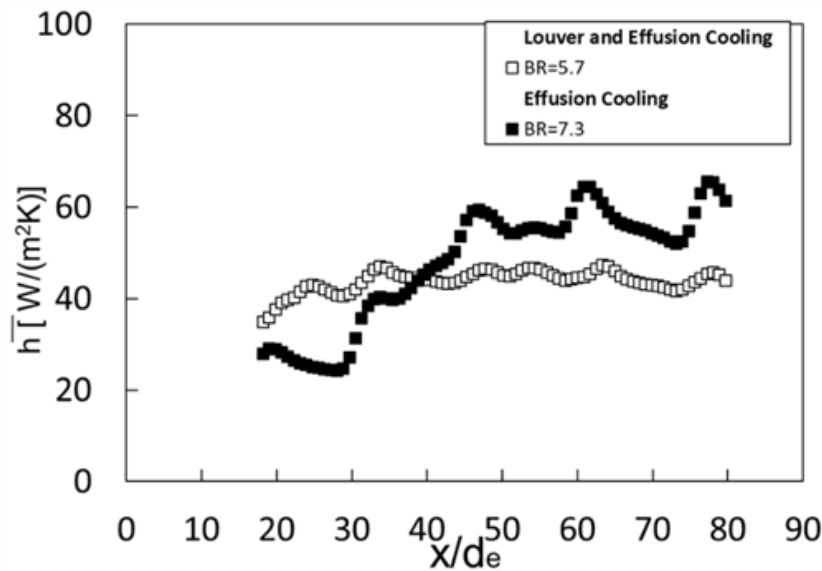


Figure 31: Heat transfer coefficient (spanwise-averaged) variations with x/d_e (at approximately the same effective blowing ratios of 6.9 and 7.3) for the effusion cooling only configuration, and for the louver and full-coverage film cooling configuration, $Re_{ms,avg}=107000$ to 114000 .

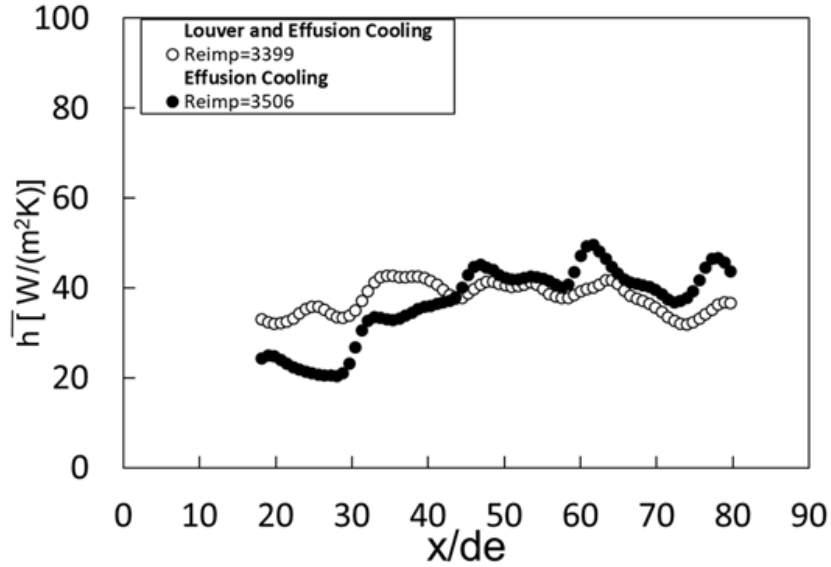


Figure 32: Heat transfer coefficient (spanwise-averaged) variations with x/d_e (at approximately the same impingement jet Reynolds numbers of 3399 and 3506) for the effusion cooling only configuration, and for the louver and full-coverage film cooling configuration, $Re_{ms,avg}=107000$ to 114000.

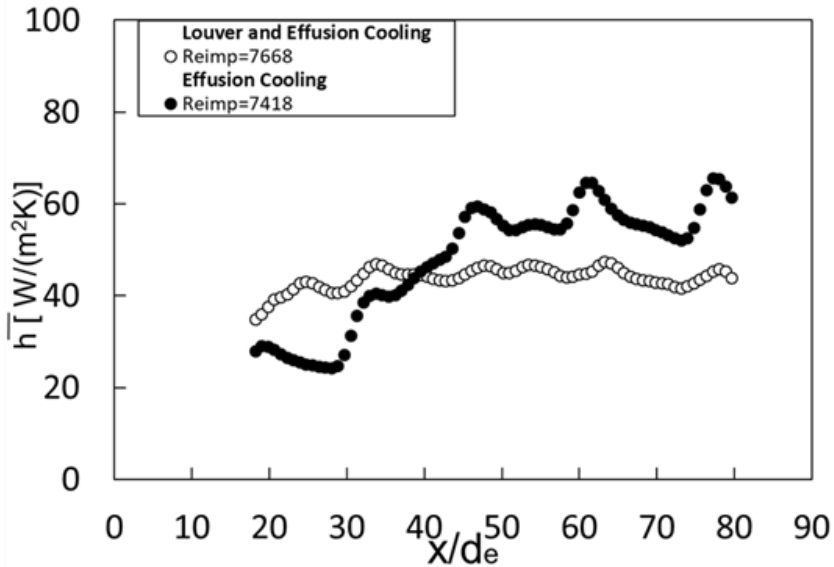


Figure 33: Heat transfer coefficient (spanwise-averaged) variations with x/d_e (at approximately the same impingement jet Reynolds numbers of 7668 and 7418) for the effusion cooling only configuration, and for the louver and full-coverage film cooling configuration, $Re_{ms,avg}=107000$ to 114000.

5.6 Spanwise-Averaged Surface Adiabatic Film Cooling Effectiveness Variations

Figures 34 to 38 give adiabatic film cooling effectiveness variations (which are spanwise-averaged) with streamwise development for different initial BR blowing ratios for $Re_{ms,avg}=107000$ to 114000. The first of these figures provides data for the louver and full-coverage film cooling configuration. The remaining figures provide comparisons of results from the effusion cooling only configuration, and from the louver and full-coverage film cooling configuration.

Figure 34 indicates that magnitudes of spanwise-averaged adiabatic effectiveness of film cooling vary by relatively small amounts, at a particular x/de streamwise location, as the initial blowing ratio is changed. When examined at a particular x/de location, values are then generally lowest when $BR=3.7$ and when $BR=5.7$. As different blowing ratio magnitudes are considered, associated effectiveness magnitudes vary only by small amounts as x/de changes, and the film cooled boundary layers develop along the test surface.

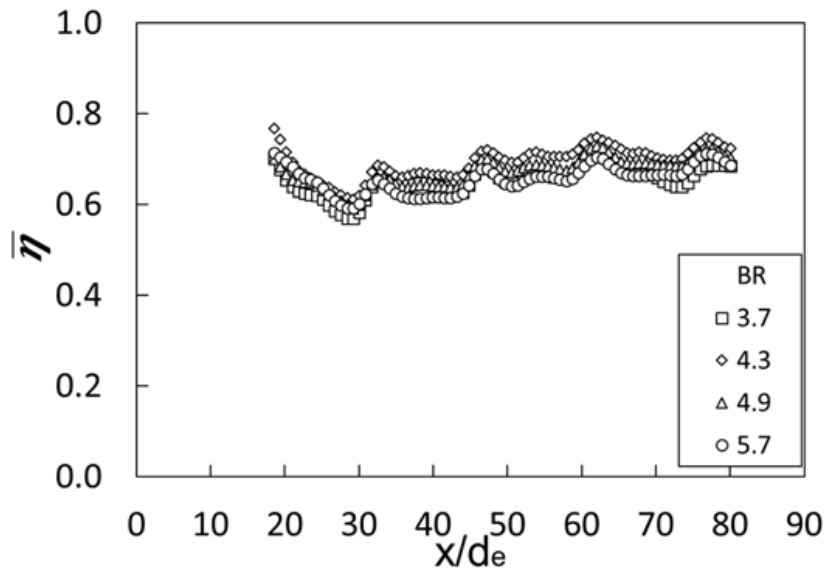


Figure 34: Adiabatic film cooling effectiveness (spanwise-averaged) variations with x/de , provided at different blowing ratios for the louver and full-coverage film cooling configuration, $Re_{ms,avg}=107000$ to 114000.

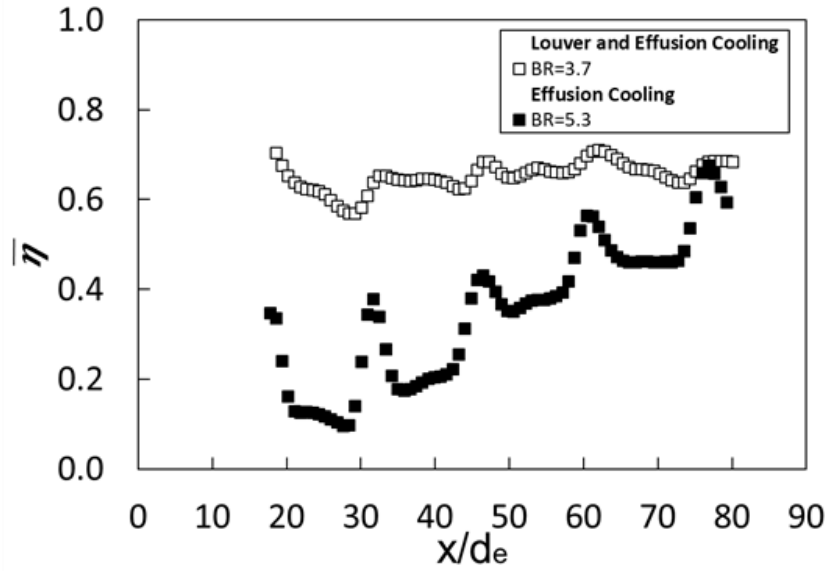


Figure 35: Adiabatic film cooling effectiveness (spanwise-averaged) variations with x/d_e (at approximately the same effective blowing ratios of 5.2 and 5.3) for the effusion cooling only configuration, and for the louver and full-coverage film cooling configuration, $Re_{ms,avg}=107000$ to 114000.

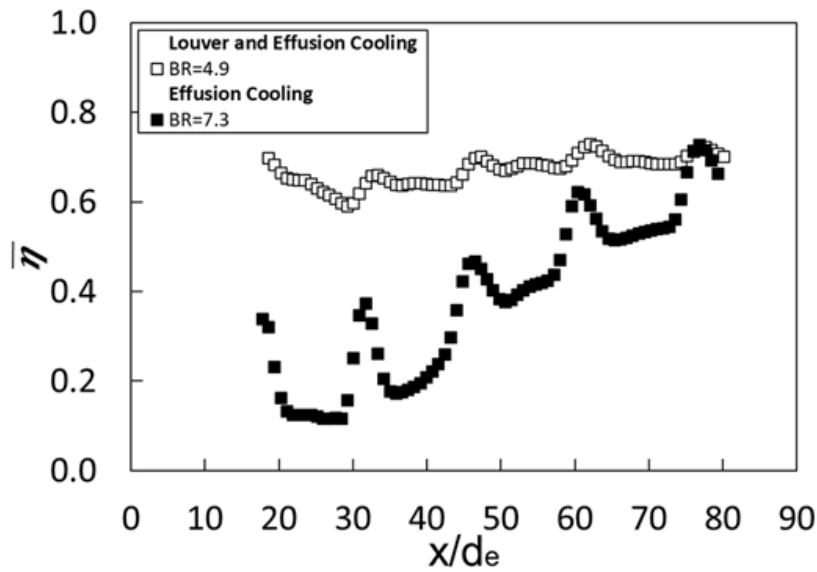


Figure 36: Adiabatic film cooling effectiveness (spanwise-averaged) variations with x/d_e (at approximately the same effective blowing ratios of 6.9 and 7.3) for the effusion cooling only configuration, and for the louver and full-coverage film cooling configuration, $Re_{ms,avg}=107000$ to 114000.

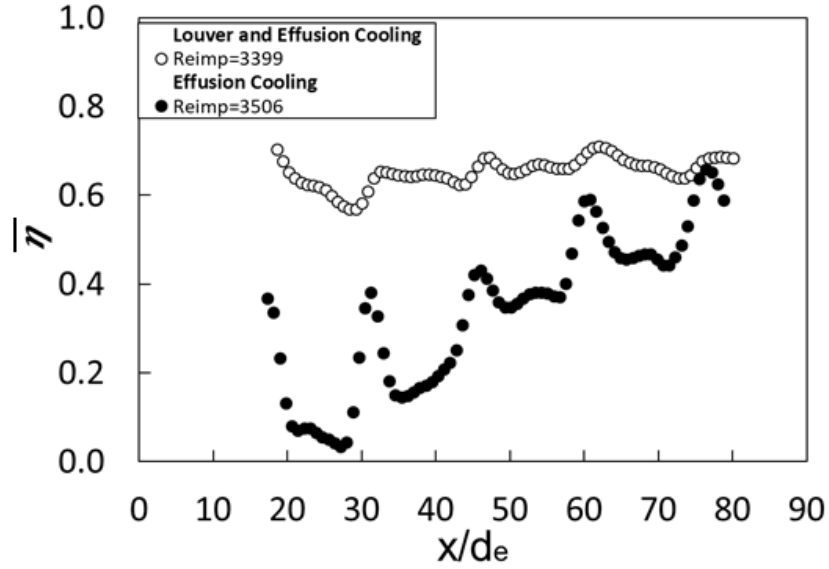


Figure 37: Adiabatic film cooling effectiveness (spanwise-averaged) variations with x/d_e (at approximately the same impingement jet Reynolds numbers of 3399 and 3506) for the effusion cooling only configuration, and for the louver and full-coverage film cooling configuration, $Re_{ms,avg}=107000$ to 114000.

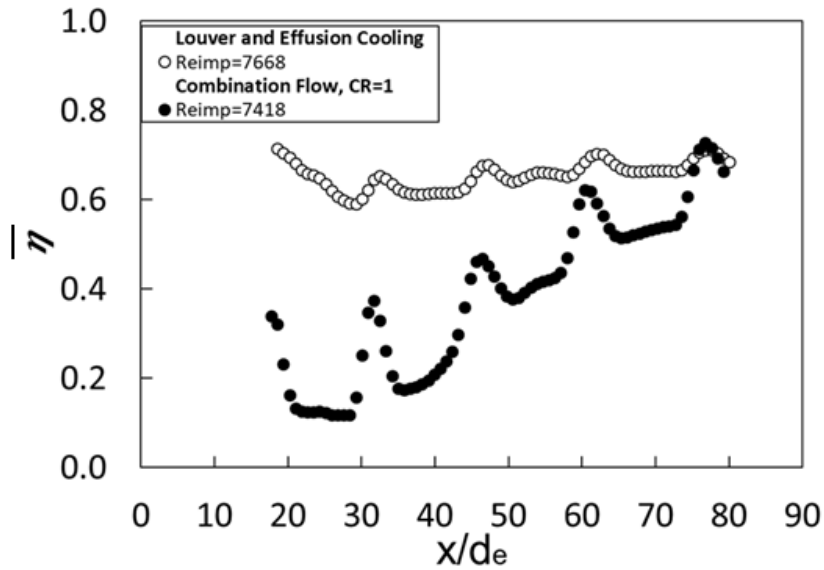


Figure 38: Adiabatic film cooling effectiveness (spanwise-averaged) variations with x/d_e (at approximately the same impingement jet Reynolds numbers of 7668 and 7418) for the effusion cooling only configuration, and for the louver and full-coverage film cooling configuration, $Re_{ms,avg}=107000$ to 114000.

Figures 35 and 36 show comparisons of adiabatic effectiveness (which are spanwise-averaged) for the effusion cooling only configuration, and for the louver and full-coverage film cooling configuration. These data are also provided for film cooling with the full-coverage arrangement associated with initial blowing ratio BR values of 5.3 and 7.3, respectively. The corresponding louver slot cooling effective blowing ratios (from Table 4) are again 5.2 and 6.9, respectively. Figures 37 and 38 show similar data comparisons based upon similar values of impingement jet Reynolds number. In all cases, data for the adiabatic effectiveness of the effusion cooling only configuration show much larger variations with streamwise development as x/de increases, as well as much larger local variations near rows of film cooling holes for x/de at and near to 15, 30, 45, 60, and 75. In particular, local maximum effectiveness values are evident at these locations. In contrast, significantly smaller line-averaged effectiveness changes with streamwise development, as well as near all near row hole locations, are present for the combined film cooling louver slot configuration. This is because the coolant from this slot is so plentiful that it is believed to surround and encapsulate volumes around the coolant trajectories which emerge from the full-coverage film cooling holes. The result is a relatively thick and relatively uniform layer of cooling air which is provided by the louver slot along the test surface downstream. Because of the nature of this layer, and the distributions of coolant which comprise this layer, contained within are significant heat sink and insulating characteristics.

The qualitative trends of the present adiabatic film cooling values (which are spanwise-averaged) are consistent with louver slot results which are presented by Inanli et al. (2017) and Kiyici et al. (2018), even though the designs and layout of the slots and film cooling holes are different. In particular, like the present data, results from these sources also show very little variation with x/de position, and with altered values of BR, as a particular louver configuration is maintained invariant.

Chapter 6: Louver and Effusion Combination Cooling with Combination Coolant Supply Arrangement for the Cross Flow Side of the Effusion Plate

The present chapter provides information on experimental flow conditions, line-averaged Nusselt numbers, and comparisons of line-averaged Nusselt number variations.

6.1 Experimental Conditions

Experimental conditions for full-coverage film cooling and louver slot cooling are given in Table 5 and Table 6, respectively. Note that louver slot blowing ratios are provided for the spanwise-normal plane at the exit of the louver leap arrangement. Table 7 then provides louver slot cooling effective blowing ratios. These effective blowing ratios apply to the full-coverage holes, and represent values determined with the same overall film mass flow rates as are present in the full-coverage holes and louver slot holes together. Such blowing ratio effective values offer a basis of comparison of data obtained with full-coverage holes and louver slots together, with data obtained with full-coverage film cooling holes only.

The experimental conditions illustrated by the data in Table 5 are obtained as the impingement jet Reynolds number is altered, with the cross flow Reynolds number approximately invariant. The range of experimental conditions associated with these tests is relatively small. This is a result of employment of cross flow and an impingement jet array together to supply the coolant. The result is a range of experimental conditions, such as the ones which are given in Table 5. Outside of these conditions, one or the other coolant supply arrangements may act in a non-optimal manner. Such an occurrence is caused by coolant flow from one source which may overwhelm and reverse the coolant flow from the other source. For example, if impingement jet magnitudes are excessive relative to the cross flow, flow from impingement jets may move in the nominal upstream direction causing the cross flow to reverse. Alternatively, if cross flow magnitudes are excessive relative to the impingement jets, cross flow may enter impingement jet hole exits, resulting in reversal of the nominal impingement flow direction.

Table 5: Film cooling full-coverage experimental conditions.

Main Flow					Cross Flow			Impingement Flow		
	V_{ms}	Mass Flow Rate	Re_{ms}	$Re_{ms,avg}$	V_{cf}	Mass Flow Rate	Re_{cf}	V_{imp}	Mass Flow Rate	Re_{imp}
Test	[m/s]	[kg/s]			[m/s]	[kg/s]		[m/s]	[kg/s]	
1	9.16	1.123	175978	174256	1.07	0.048	10761	15.81	0.062	8601
2	9.05	1.108	173452	172376	1.14	0.051	11455	20.09	0.079	10954
3	8.92	1.092	170914	169697	1.17	0.053	11768	24.31	0.096	13293
4	8.72	1.070	167764	166078	1.21	0.055	12186	30.01	0.120	16540
Effusion Flow					Non-Dimensional Parameters					
	V_{ef}	Mass Flow Rate	Mach Number	Re_{ef}	Discharge Coefficient	Density Ratio	Velocity Ratio	Momentum Flux Ratio	Blowing Ratio	
Test	[m/s]	[kg/s]			C_d	DR	VR	I	BR	
1	34.2	0.111	0.10	14126	0.83	1.04	3.73	14.52	3.89	
2	40.4	0.131	0.12	16673	0.87	1.05	4.46	20.83	4.67	
3	46.1	0.149	0.13	18966	0.88	1.05	5.16	27.90	5.40	
4	53.6	0.174	0.16	22194	0.88	1.05	6.15	39.68	6.45	

Table 6: Louver slot cooling experimental conditions.

Velocity Ratio	Momentum Flux Ratio	Blowing Ratio	Density Ratio
VR	I	BR	DR
1.73	3.14	1.81	1.04
2.07	4.51	2.18	1.05
2.40	6.04	2.52	1.05
2.86	8.59	3.01	1.05

Table 7: Louver slot cooling effective blowing ratios.

Effusion BR	Louver Slot BR	Effective BR without Louver Slot
3.89	1.81	5.50
4.67	2.18	6.59
5.40	2.52	7.63
6.45	3.01	9.12

6.2 Test Section Velocity, Pressure, and Blowing Ratio Variations

Additional understanding of the impingement jet and cross flow coolant supply arrangement is provided by the data in Figures 39-41. Here, the normalized pressure drop is presented as it varies with blowing ratio for the cross flow and main flow passages (Figure 39), the impingement and main flow passages (Figure 40), and the impingement and the cross flow passages (Figure 41). These data are presented for a $Re_{ms,avg}$ main flow Reynolds number of 166000 to 176000. Note that the sum of the first and third pressure drops is equal to the second pressure drop at each

blowing ratio considered. Note that all three types of pressure drop increase with blowing ratio. Because coolant air is supplied to the louver feed holes and the effusion holes from the same cross flow passage source, pressure variations associated with the louver alone cannot be determined separately.

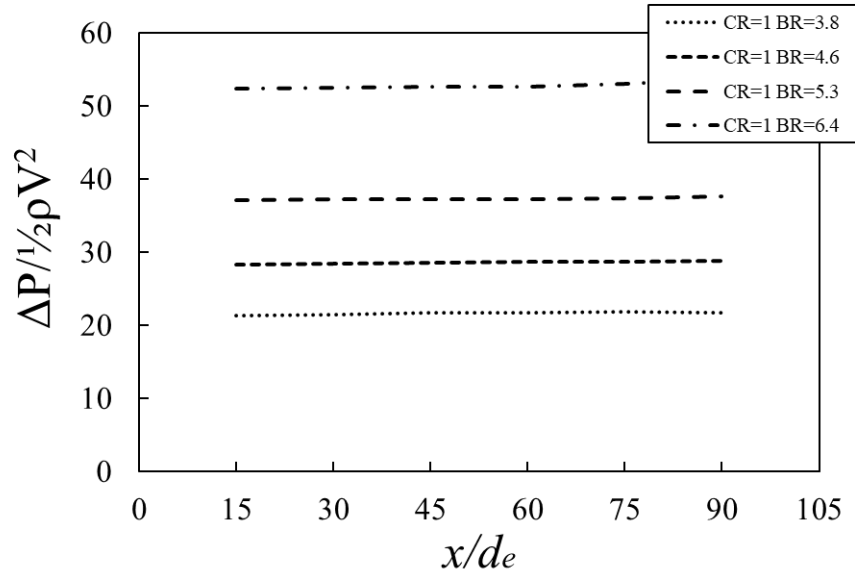


Figure 39: Normalized pressure variations between cross flow to mainstream for mainstream Reynolds values of $Re_{ms,avg}=166000$ to 176000 .

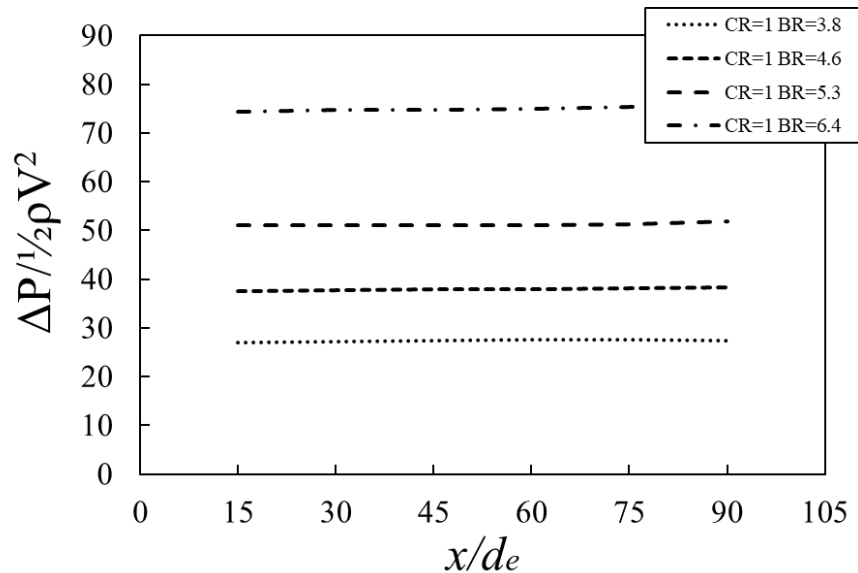


Figure 40: Normalized pressure variations between impingement flow to mainstream for mainstream Reynolds values of $Re_{ms,avg}=166000$ to 176000 .

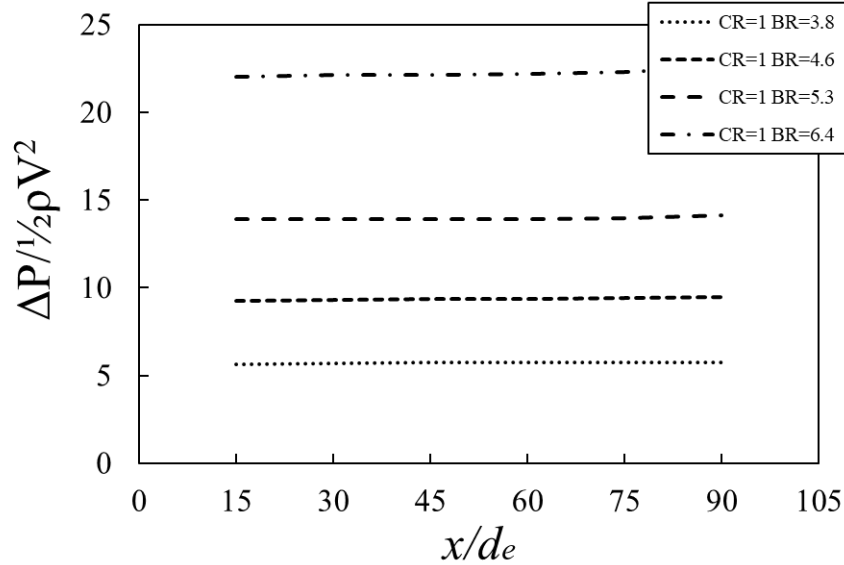


Figure 41: Normalized pressure variations between impingement flow to cross flow for mainstream Reynolds values of $Re_{ms,avg}=166000$ to 176000 .

The resulting alterations of local main flow freestream velocity and spatially-averaged effusion flow velocity with blowing ratio are then given in Figures 42 and 43, respectively. Because the test section inlet and outlet areas are the same within the current study, no significant pressure gradient is present in the main flow passage, and the freestream velocity is constant with streamwise position. Figure 42 shows that this freestream velocity is also invariant with blowing ratio. The associated main flow static pressure is also generally and approximately invariant with x/de streamwise location and blowing ratio, as shown in Figure 44. Figure 45 then presents local blowing ratio changes with normalized streamwise location x/de for different initial blowing ratio values. For each of these initial values, local BR magnitudes are approximately constant with streamwise development as x/de increases. This is, of course, partially a consequence of the zero streamwise pressure gradient which is present within the main flow passage.

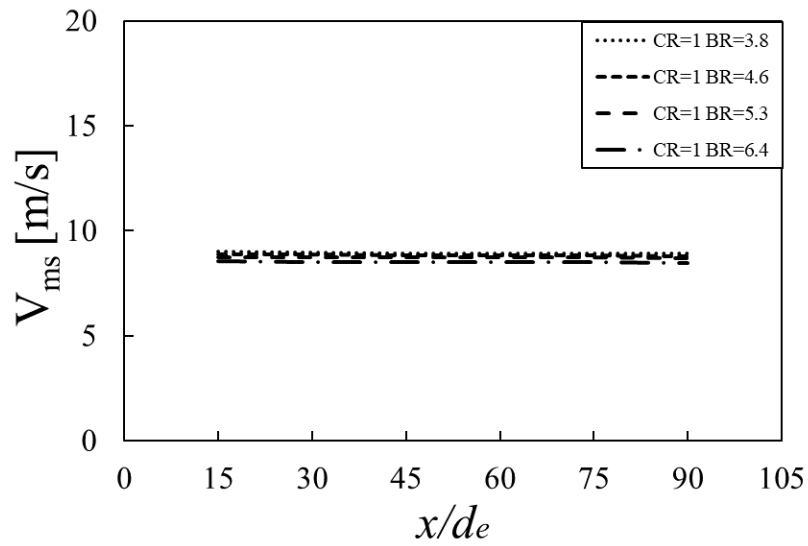


Figure 42: Mainstream velocity variations with normalized streamwise location for mainstream Reynolds values of $Re_{ms,avg}=166000$ to 176000 .

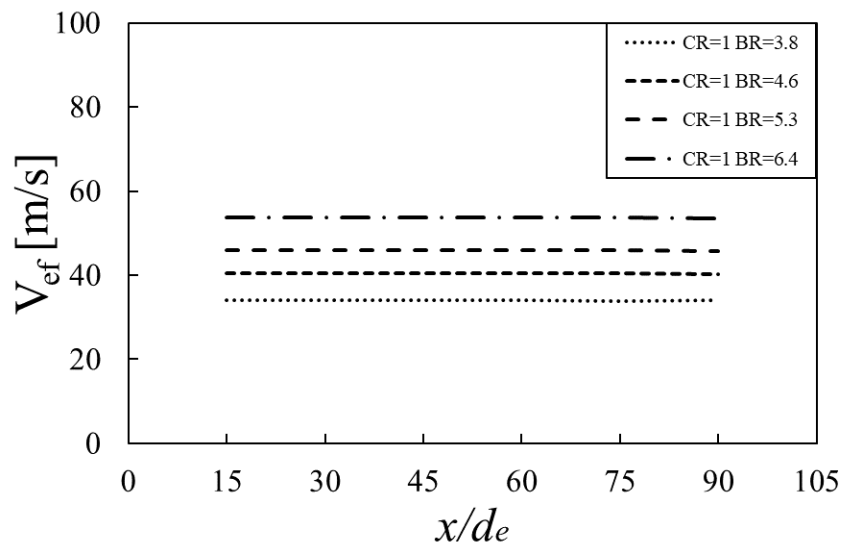


Figure 43: Effusion hole exit velocity variations with normalized streamwise location for mainstream Reynolds values of $Re_{ms,avg}=166000$ to 176000 .

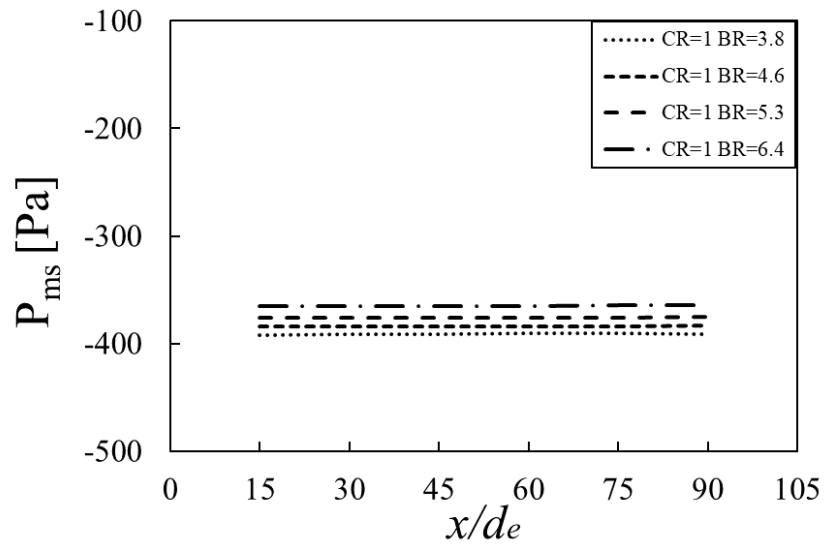


Figure 44: Mainstream pressure variations with normalized streamwise location for mainstream Reynolds values of $Re_{ms,avg}=166000$ to 176000 .

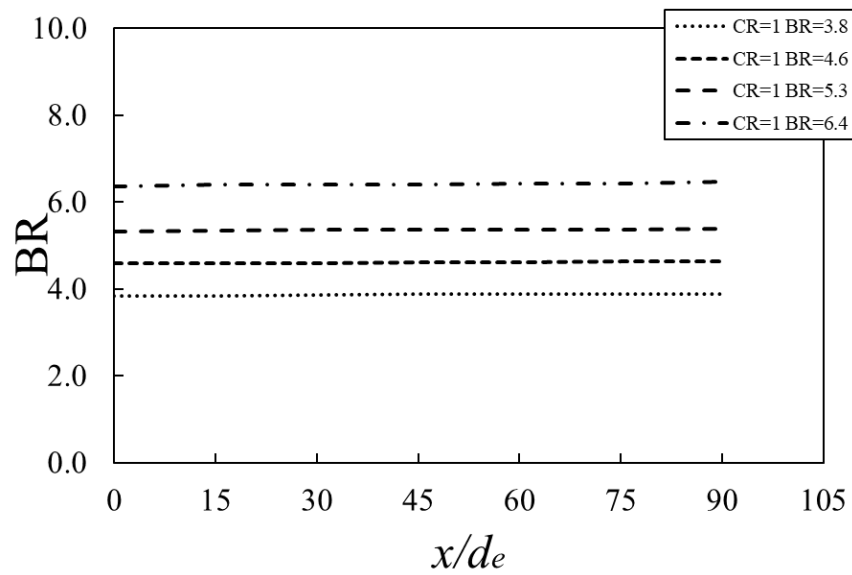


Figure 45: Blowing ratio variations with normalized streamwise location for mainstream Reynolds values of $Re_{ms,avg}=166000$ to 176000 .

6.3 Line-Averaged Cold-Side Data for the Combination Cross Flow and Impingement Jet Array Arrangement

Line-averaged Nusselt number data for cross flow cooling and impingement jet array cooling together are presented in Figure 46 as they vary with x/de , for the cold side of the double-wall test plate. Such results are determined from surface distributions of local, spatially-resolved surface Nusselt numbers. The data in Figure 46 are given for initial blowing ratios of 3.9, 4.7, 5.4, and 6.5, and for main flow Reynolds numbers $Re_{ms,avg}$ of 166000 to 176000. Measured test surface Nusselt numbers within these figures vary from 25 to values as high as 85, and are given for the $CR=1$ cross flow/impingement combination configuration. Note that dashed rectangles denote impingement hole streamwise locations, whereas solid rectangles denote effusion hole entrance streamwise locations, within Figure 46. Within this figure, the upstream edge of the spatially-resolved measurements is located at $x/de=0$.

Regardless of the value of initial blowing ratio BR , results in Figure 46 show that the highest line-averaged Nusselt numbers are often present at larger x/de locations, relative to the locations of the impingement hole centerlines. These locally augmented Nusselt number regions are then often positioned at lower x/de locations, relative to effusion hole entrance streamwise locations. As such, evidence is provided of turning and re-direction of the impingement jets, as the jet fluid crosses the cross flow passage. Associated variations indicate that the impingement jets are more influential in affecting local and line-averaged Nusselt number variations, than the cross flow. Data in Figure 46 evidence such a conclusion since greater impingement jet turning seems to be present at local blowing ratio increases. In addition, when compared for a particular streamwise location x/de and mainstream Reynolds number $Re_{ms,avg}$, line-averaged Nusselt numbers in Figure 46 consistently increase with initial blowing ratio BR for most all x/de values.

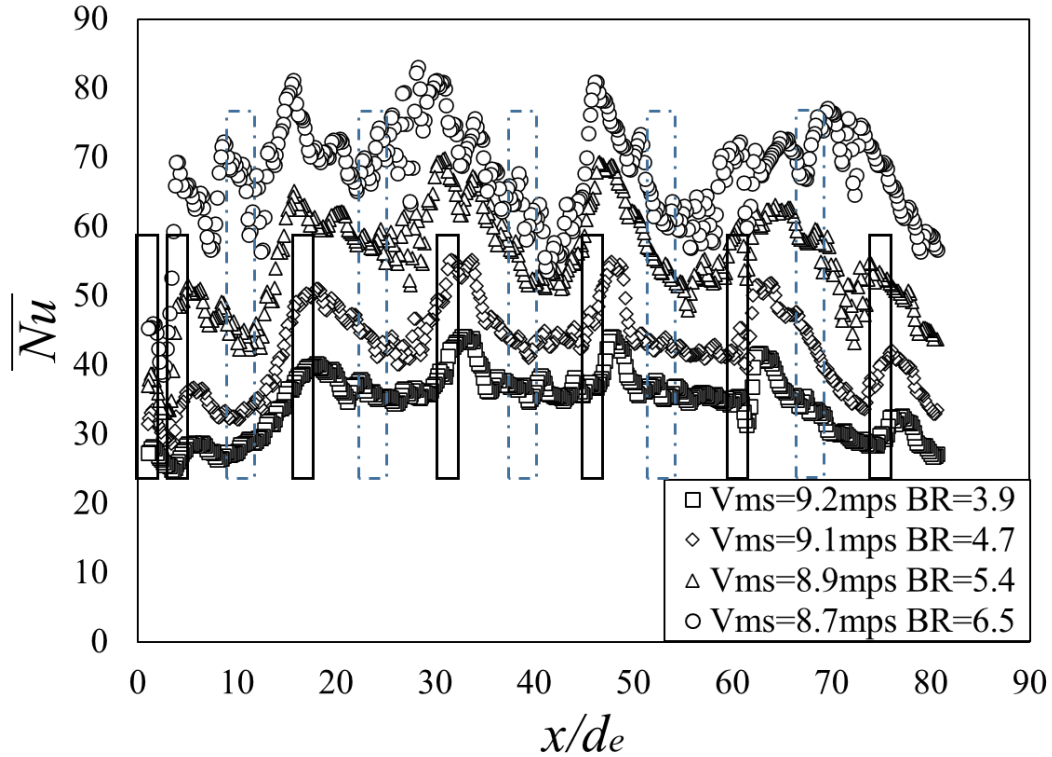


Figure 46: Cold-side line-averaged surface Nusselt number variations with normalized streamwise location for different values of initial blowing ratio for $Re_{ms,avg}=166000$ to 176000 . Solid rectangles denote effusion hole entrance streamwise locations. Dashed rectangles denote impingement hole streamwise locations.

6.4 Line-Averaged Cold-Side Nusselt Number Data for Different Coolant Supply Arrangements

Additional line-averaged Nusselt number data are given in Figures 47-50 for different blowing ratios. Compared in these figures are data for louver and effusion cooling with $CR=1$ and data for effusion only cooling with $CR=4$. Each comparison is provided for an effective blowing ratio for the louver and effusion arrangement, which approximately matches the blowing ratio associated with the effusion cooling only arrangement. For all of these results, the coolant is supplied by a cross flow and impingement jet array combination arrangement.

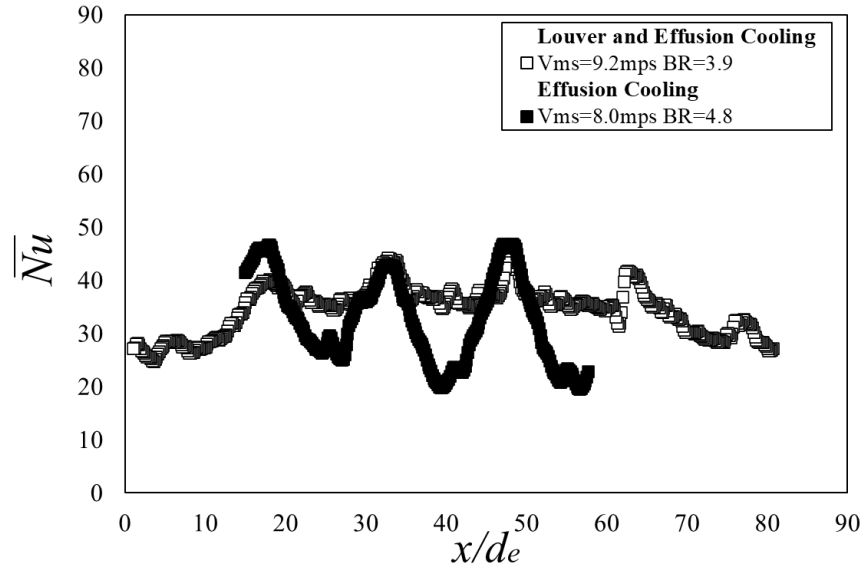


Figure 47: Comparison of line-averaged surface Nusselt number variations for louver and effusion cooling with CR=1 and BR=3.9, and effusion only cooling with CR=4 for and BR=4.8.

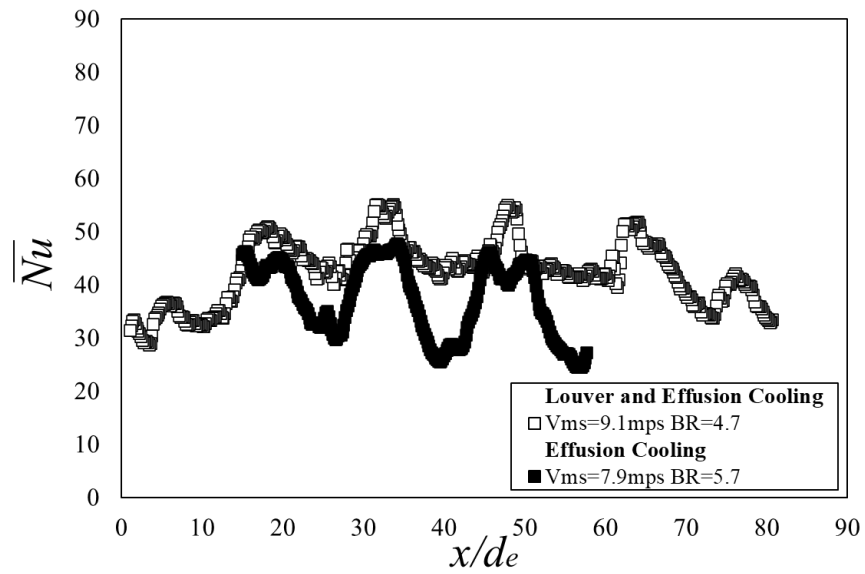


Figure 48: Comparison of line-averaged surface Nusselt number variations for louver and effusion cooling with CR=1 and BR=4.7, and effusion only cooling with CR=4 for and BR=5.7.

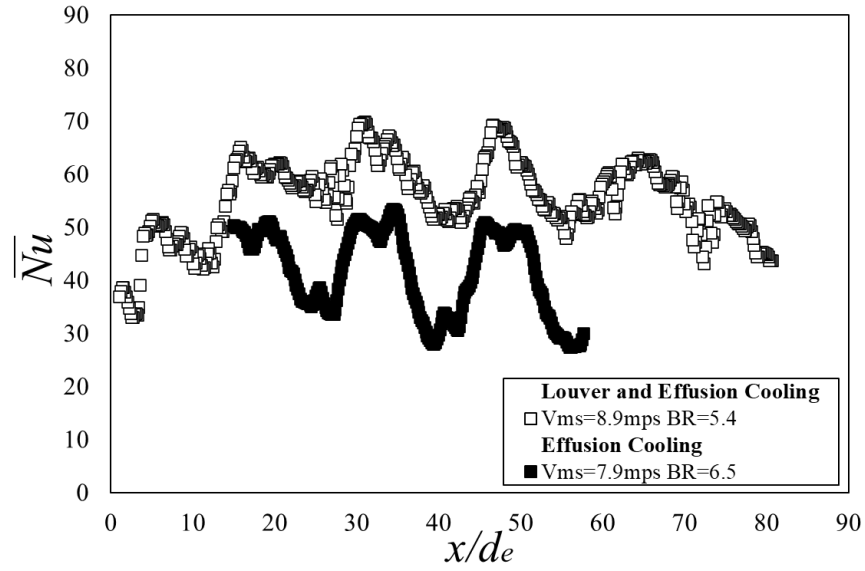


Figure 49: Comparison of line-averaged surface Nusselt number variations for louver and effusion cooling with CR=1 and BR=5.4, and effusion only cooling with CR=4 for and BR=6.5.

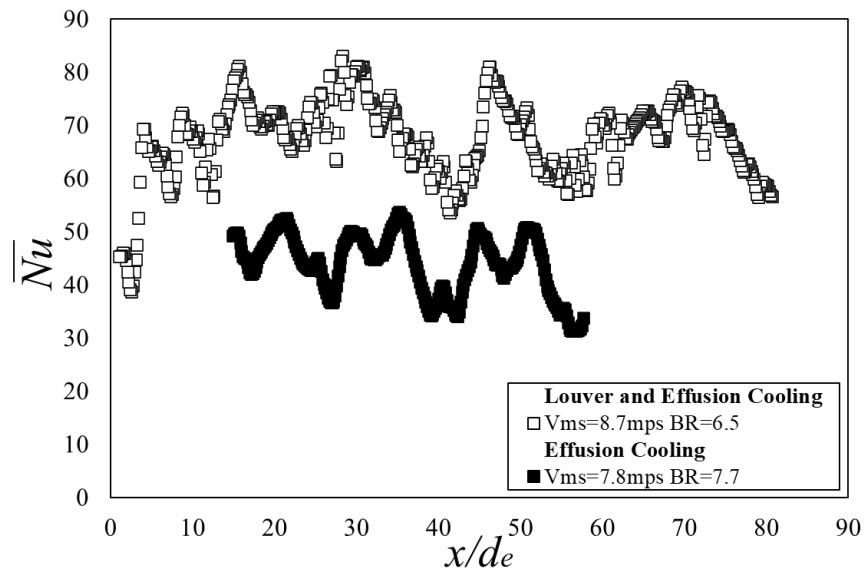


Figure 50: Comparison of line-averaged surface Nusselt number variations for louver and effusion cooling with CR=1 and BR=6.5, and effusion only cooling with CR=4 for and BR=7.7.

Chapter 7: Louver and Effusion Combination Cooling with an Impingement Only Coolant Supply Arrangement for the Cross Flow Side of the Effusion Plate

The present chapter provides information on experimental flow conditions, line-averaged Nusselt numbers, and comparisons of line-averaged Nusselt number variations for louver and effusion cooling with an impingement only coolant supply. Data in the first part of the chapter are given for mainstream Reynolds values $Re_{ms,avg}$ of 145000 to 161000. Data in the second part of the chapter are given for mainstream Reynolds values $Re_{ms,avg}$ of 92000 to 102000.

7.1 Experimental Conditions

Experimental conditions for the full-coverage film cooling and louver slot cooling are given in Table 8 and Table 9, respectively. Note that louver slot blowing ratios are provided for the spanwise-normal plane at the exit of the louver leap arrangement. Table 10 provides louver slot cooling effective blowing ratios. These effective blowing ratios apply to the full-coverage holes, and represent values determined with the same overall film mass flow rates as are present in the full-coverage holes and louver slot holes together. Such blowing ratio effective values offer a basis of comparison of data obtained with full-coverage holes and louver slots together, with data obtained with full-coverage film cooling holes only.

Table 8: Experimental Conditions for Impingement Only for mainstream Reynolds number values of $Re_{ms,avg}$ =145000 to 161000.

Main Flow					Cross Flow			Impingement Flow		
	V_{ms}	Mass Flow Rate	Re_{ms}	$Re_{ms,avg}$	V_{cf}	Mass Flow Rate	Re_{cf}	V_{imp}	Mass Flow Rate	Re_{imp}
Test	[m/s]	[kg/s]			[m/s]	[kg/s]		[m/s]	[kg/s]	
1	8.45	1.033	161451	160404	-	-	-	15.21	0.060	8238
2	8.18	0.998	155872	154449	-	-	-	22.82	0.090	12434
3	7.80	0.952	148637	147657	-	-	-	31.24	0.125	17220
4	7.62	0.933	145891	145083	-	-	-	35.51	0.143	19713
Effusion Flow					Non-Dimensional Parameters					
	V_{ef}	Mass Flow Rate	Mach Number	Re_{ef}	Discharge Coefficient	Density Ratio	Velocity Ratio	Momentum Flux Ratio	Blowing Ratio	
Test	[m/s]	[kg/s]			C_d	DR	VR	I	BR	
1	18.6	0.060	0.05	7637	0.65	1.04	2.20	5.03	2.29	
2	28.0	0.090	0.08	11506	0.71	1.05	3.42	12.23	3.58	
3	38.6	0.125	0.11	15895	0.74	1.05	4.95	25.70	5.19	
4	44.0	0.143	0.13	18190	0.76	1.05	5.77	35.02	6.07	

Table 9: Louver slot cooling experimental conditions.

Velocity Ratio	Momentum Flux Ratio	Blowing Ratio	Density Ratio
VR	I	BR	DR
1.02	1.09	1.07	1.04
1.59	2.65	1.67	1.05
2.30	5.56	2.42	1.05
2.68	7.58	2.83	1.05

Table 10: Louver slot cooling effective blowing ratios.

Effusion BR	Louver Slot BR	Effective BR without Louver Slot
2.29	1.07	3.23
3.58	1.67	5.05
5.19	2.42	7.34
6.07	2.83	8.57

The experimental conditions illustrated by the data in Table 8 are obtained as the impingement jet Reynolds number is altered, as the impingement jet array only is used to supply the coolant. The range of experimental conditions associated with these tests is larger than the range of experimental conditions associated with the combination coolant supply arrangement.

7.2 Test Section Velocity, Pressure, and Blowing Ratio Variations

Additional understanding of the impingement jet coolant supply arrangement is provided by the data in Figures 51-53. Here, the normalized pressure drop is presented as it varies with blowing ratio for the cross flow and main flow passages (Figure 51), the impingement and main flow passages (Figure 52), and the impingement and the cross flow passages (Figure 53). These data are presented for a $Re_{ms,avg}$ main flow Reynolds number of 145000 to 160000. Note that the sum of the first and third pressure drops is equal to the second pressure drop at each blowing ratio considered. Note that all three types of pressure drop generally increase with blowing ratio. Because coolant air is supplied to the louver feed holes and the effusion holes from the same cross flow passage source, pressure variations associated with the louver alone cannot be determined separately.

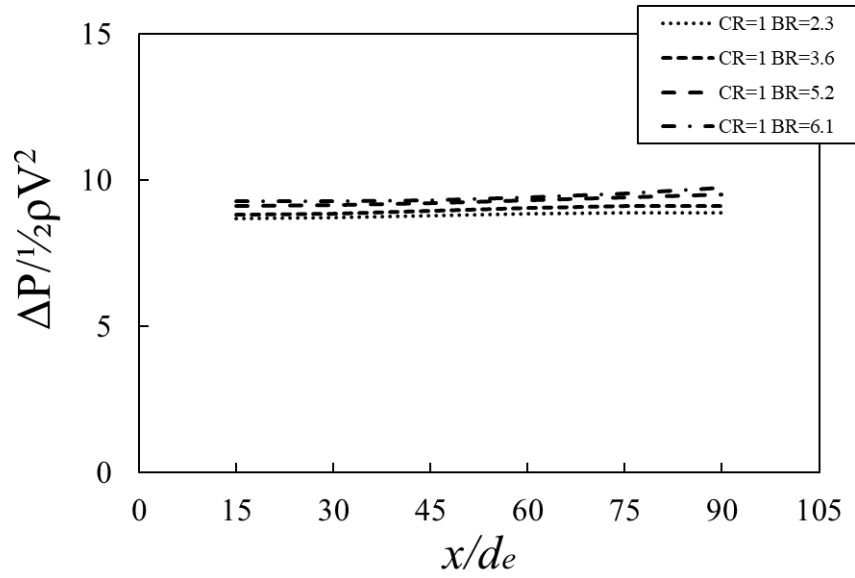


Figure 51: Normalized pressure variations between cross flow to mainstream flow for mainstream Reynolds values of $Re_{ms,avg}=145000$ to 161000 .

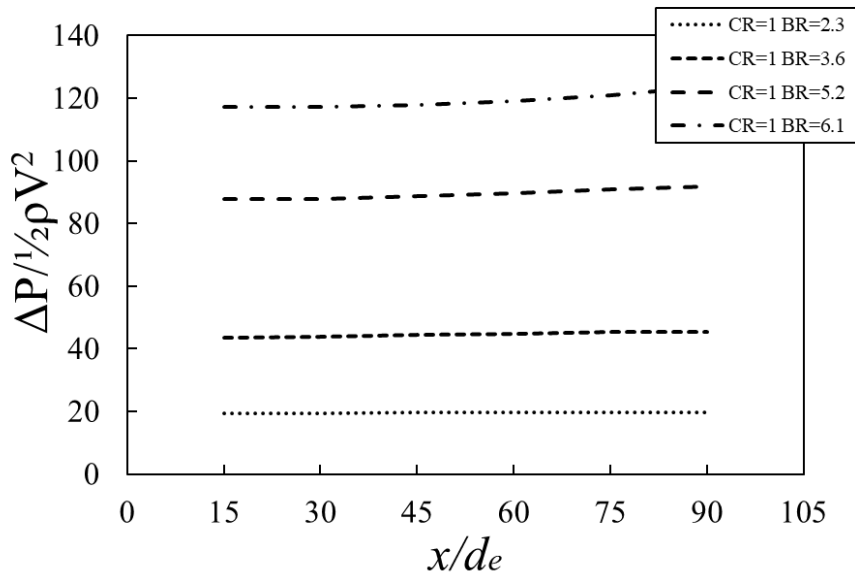


Figure 52: Normalized pressure variations between impingement flow to mainstream flow for mainstream Reynolds values of $Re_{ms,avg}=145000$ to 161000 .

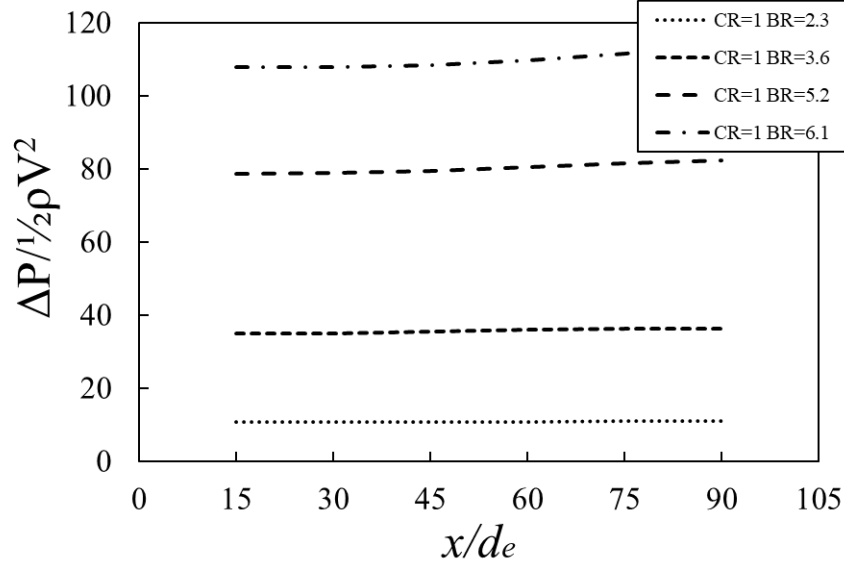


Figure 53: Normalized pressure variations between impingement flow to cross flow for mainstream Reynolds values of $Re_{ms,avg}=145000$ to 161000 .

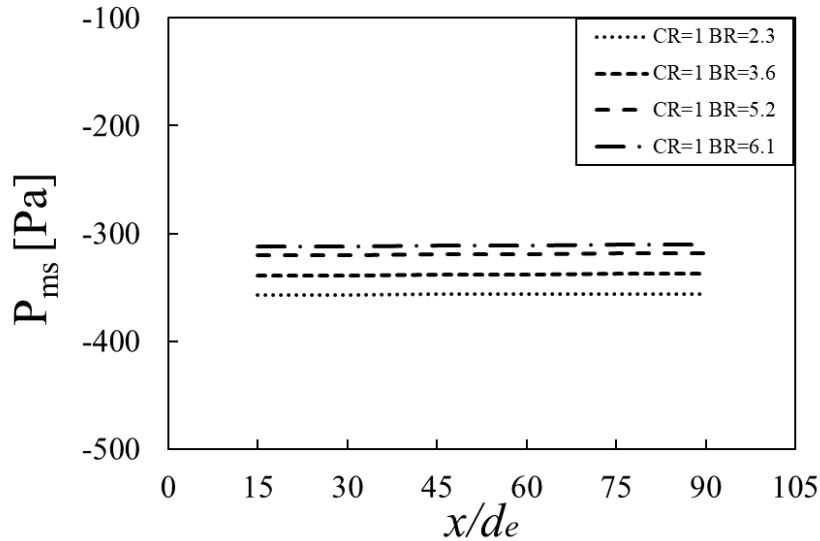


Figure 54: Mainstream pressure variations for mainstream Reynolds values of $Re_{ms,avg}=145000$ to 161000 .

The resulting alterations of local main flow static pressure, local main flow freestream velocity, and spatially-averaged effusion flow velocity with blowing ratio are then given in Figures 54, 55, and 56, respectively. Because the test section inlet and outlet areas are the same within the current study, no significant pressure gradient is present within the main flow passage, and the freestream velocity is constant with streamwise position. Figure 55 shows that this freestream velocity is also invariant with blowing ratio. The associated main flow static pressure is also generally invariant

with x/d_e streamwise location and blowing ratio, as shown in Figure 54. Figure 57 then presents local blowing ratio changes with normalized streamwise location x/d_e for different initial blowing ratio values.

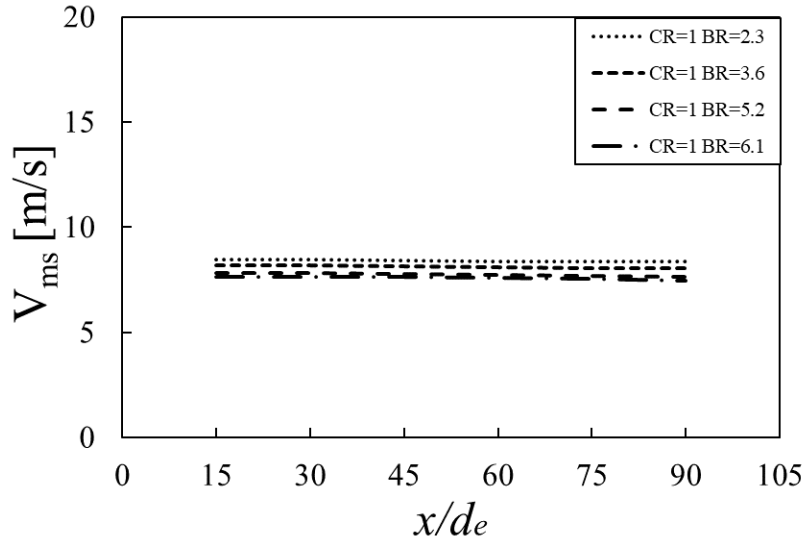


Figure 55: Mainstream velocity variations for mainstream Reynolds values of $Re_{ms,avg}=145000$ to 161000.

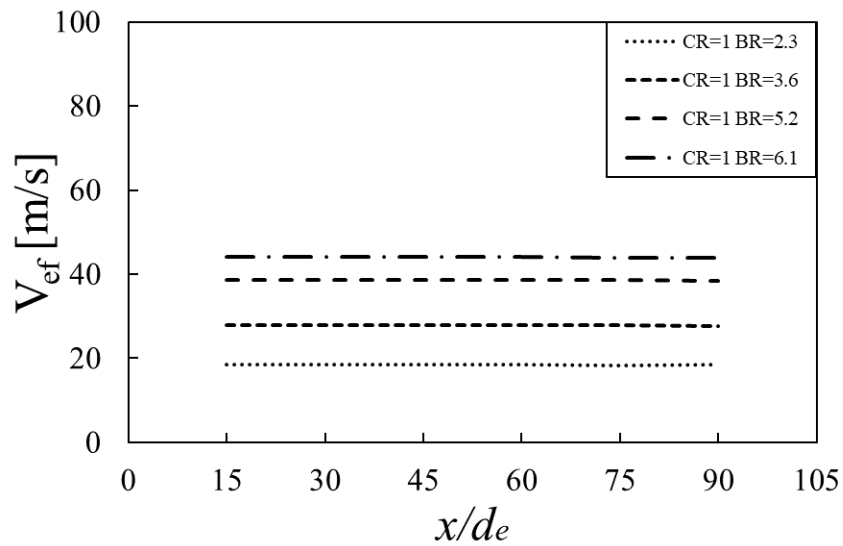


Figure 56: Effusion hole velocity variations for mainstream Reynolds values of $Re_{ms,avg}=145000$ to 161000.

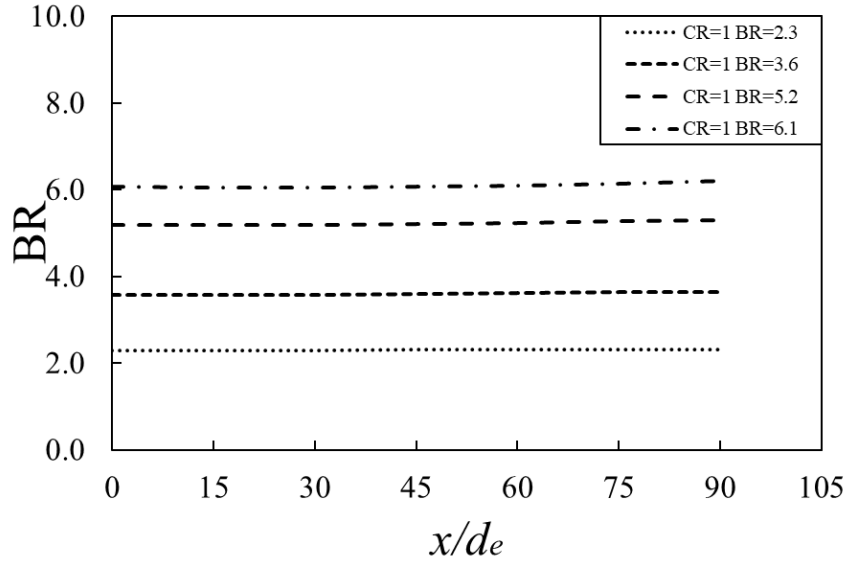


Figure 57: Blowing ratio variations for mainstream Reynolds values of $Re_{ms,avg}=145000$ to 161000

7.3 Line-Averaged Cold-Side Data for the Impingement Jet Array Only Arrangement

Line-averaged Nusselt number data for impingement jet array cooling only are presented in Figure 58 as they vary with x/de , for the cold side of the double-wall test plate. Such results are determined from surface distributions of local, spatially-resolved surface Nusselt numbers. The data in Figure 58 are given for initial blowing ratios of 2.3, 3.6, 5.2, and 6.1, and for main flow Reynolds numbers $Re_{ms,avg}$ of 166000 to 176000. Measured test surface Nusselt numbers within these figures vary from 25 to values as high as 75, and are given for the CR=1 impingement only configuration. Note that dashed rectangles denote impingement hole streamwise locations, whereas solid rectangles denote effusion hole entrance streamwise locations, within Figure 58. Within this figure, the upstream edge of the spatially-resolved measurements is located at $x/de=0$.

Regardless of the value of initial blowing ratio BR, results in Figure 58 show that the highest line-averaged Nusselt numbers are often present at larger x/de locations, relative to the locations of the impingement hole centerlines. These locally augmented Nusselt number regions are then often positioned at lower x/de locations, relative to effusion hole entrance streamwise locations. As such, evidence is provided of turning and re-direction of the impingement jets, as the jet fluid crosses the cross flow passage. This is because static pressure variations within the cross flow passage induce coolant motion towards and into the entrances of effusion holes. Note that, for the present arrangement, this turning is in the same direction as the cross flow, whose direction is aligned with the positive x/de direction. Data in Figure 58 also show that greater impingement jet

turning seems to be present at local blowing ratio increases. In addition, when compared for a particular streamwise location x/d_e and mainstream Reynolds number $Re_{ms,avg}$, line-averaged Nusselt numbers in Figure 58 often increase with initial blowing ratio BR, especially near impingement jet impact locations. These changes are directly related to increases of the impingement jet Reynolds number, which is directly related to the strength of each individual impingement jet.

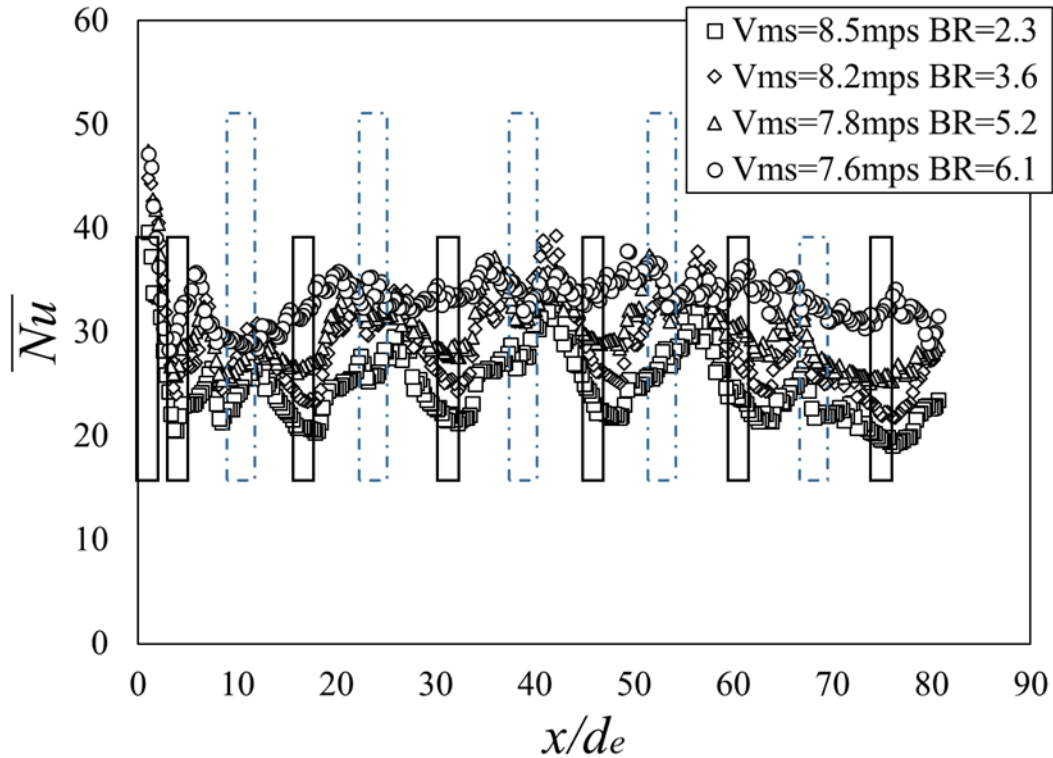


Figure 58: Cold-side line-averaged surface Nusselt number variations with normalized streamwise location for different values of initial blowing ratio for $Re_{ms,avg}=145000$ to 161000 . Solid rectangles denote effusion hole entrance streamwise locations. Dashed rectangles denote impingement hole streamwise locations.

7.4 Line-Averaged Cold-Side Nusselt Number Data for Different Coolant Supply Arrangements

Line-averaged Nusselt number data for the cold side of the double-wall test plate, and for different coolant supply arrangements, are given in Figures 59-62. Compared in these figures are data for the CR=1 louver and effusion cooling, with combination cross flow and impingement jet array coolant supply, and CR=1 louver and effusion cooling with impingement jet array only

coolant supply. Nusselt number data associated with the louver and effusion combination cooling generally increase as BR increases.

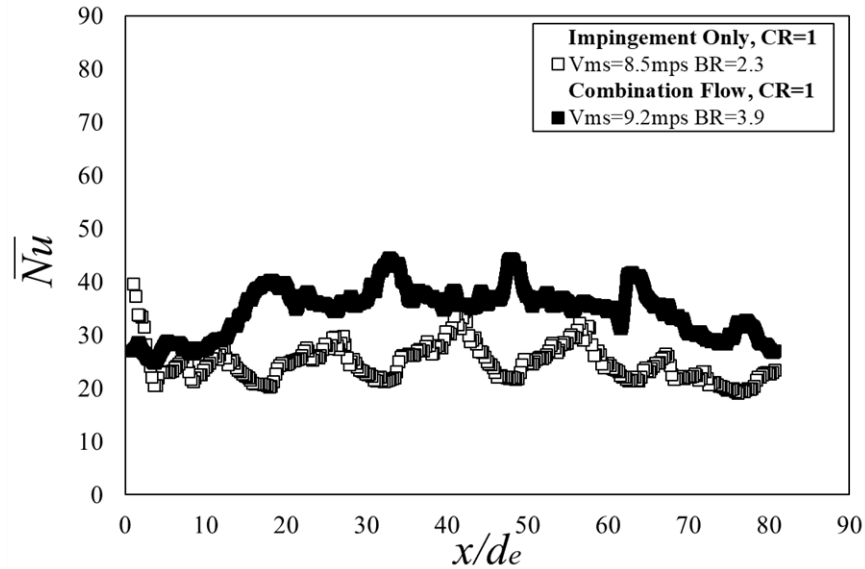


Figure 59: Comparison of line-averaged surface Nusselt number variation between impingement only and cross flow and impingement together for BR=2.3 and BR=3.9, respectively.

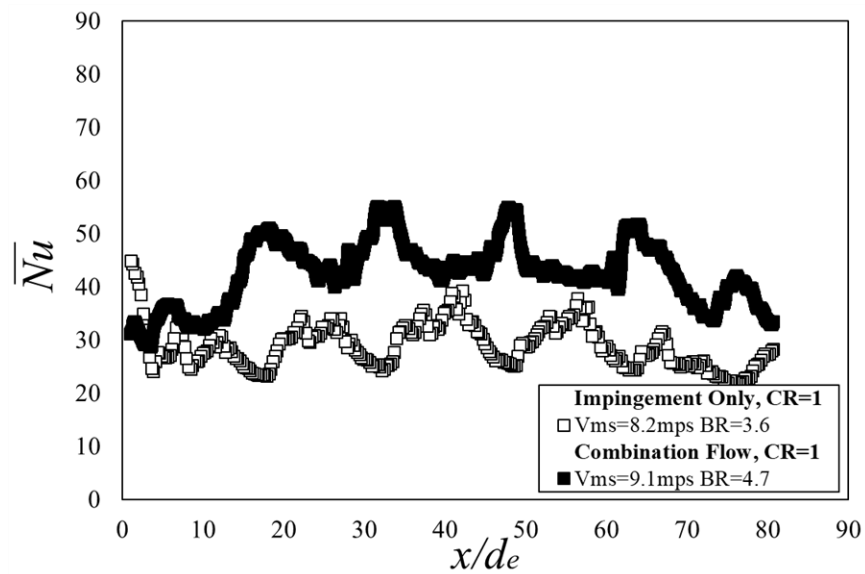


Figure 60: Comparison of line-averaged surface Nusselt number variation between impingement only and cross flow and impingement together for BR=3.6 and BR=4.7, respectively.

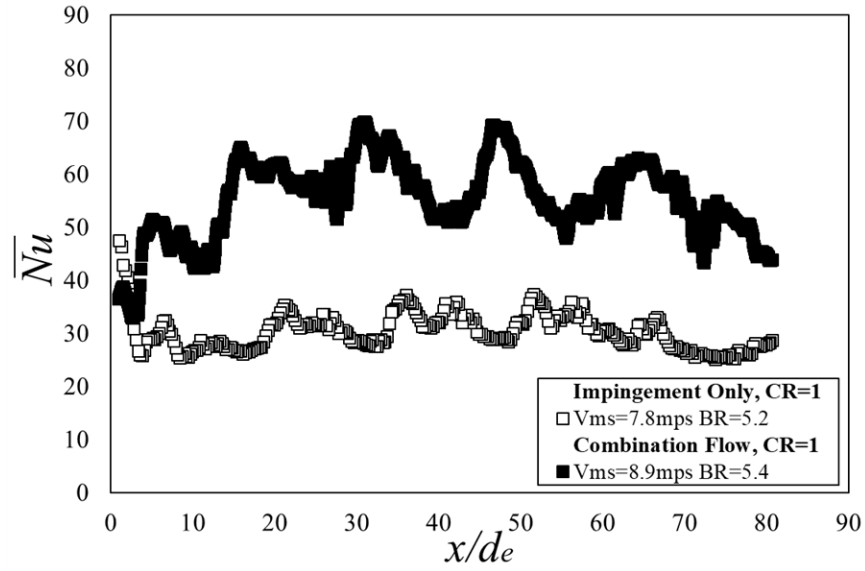


Figure 61: Comparison of line-averaged surface Nusselt number variation between impingement only and cross flow and impingement together for BR=5.2 and BR=5.4, respectively.

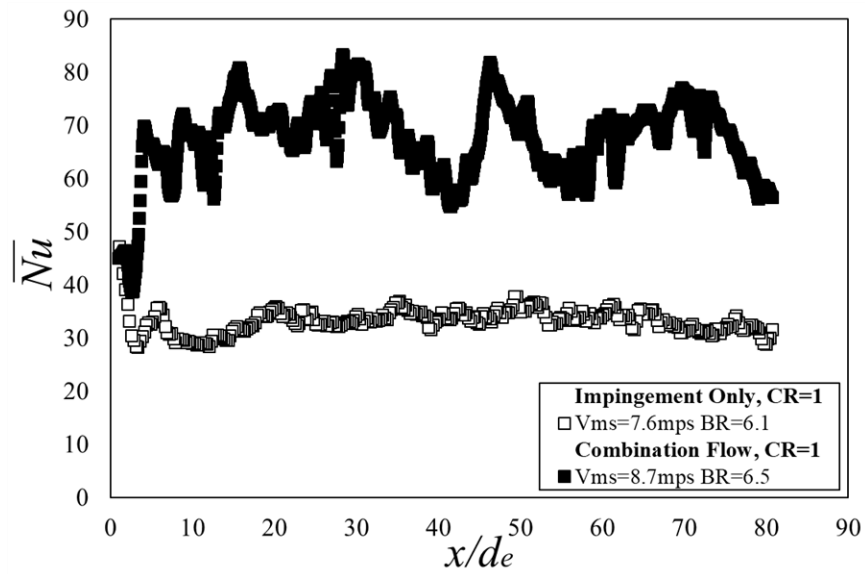


Figure 62: Comparison of line-averaged surface Nusselt number variation between impingement only and cross flow and impingement together for BR=6.3 and BR=6.1, respectively.

7.5 Experimental Conditions

Experimental conditions for the full-coverage film cooling and louver slot cooling are given in Table 11 and Table 12, respectively. The experimental conditions illustrated by the data in Table 11 are obtained as the impingement jet Reynolds number is altered, as impingement jets only are used to supply the coolant. Note that louver slot blowing ratios are provided for the spanwise-normal plane at the exit of the louver leap arrangement. Table 13 provides louver slot cooling effective blowing ratios. These effective blowing ratios apply to the full-coverage holes, and represent values determined with the same overall film mass flow rates as are present in the full-coverage holes and louver slot holes together. Such blowing ratio effective values offer a basis of comparison of data obtained with full-coverage holes and louver slots together, with data obtained with full-coverage film cooling holes only.

Table 11: Experimental Conditions for Impingement Only for mainstream Reynolds number values of $Re_{ms,avg}=92000$ to 102000 .

Main Flow					Cross Flow			Impingement Flow		
	V_{ms}	Mass Flow Rate	Re_{ms}	$Re_{ms,avg}$	V_{cf}	Mass Flow Rate	Re_{cf}	V_{imp}	Mass Flow Rate	Re_{imp}
Test	[m/s]	[kg/s]			[m/s]	[kg/s]		[m/s]	[kg/s]	
1	5.34	0.653	102140	102426	-	-	-	9.63	0.038	5198
2	5.10	0.623	97339	97674	-	-	-	13.94	0.055	7534
3	4.91	0.600	93661	93570	-	-	-	18.77	0.074	10167
4	4.80	0.587	91900	91779	-	-	-	21.29	0.084	11553
Effusion Flow					Non-Dimensional Parameters					
	V_{ef}	Mass Flow Rate	Mach Number	Re_{ef}	Discharge Coefficient	Density Ratio	Velocity Ratio	Momentum Flux Ratio	Blowing Ratio	
Test	[m/s]	[kg/s]			C_d	DR	VR	I	BR	
1	12.0	0.038	0.03	4913	0.62	1.04	2.24	5.21	2.33	
2	18.4	0.055	0.05	7530	0.74	1.04	3.60	13.49	3.75	
3	25.6	0.074	0.07	10456	0.80	1.04	5.21	28.25	5.42	
4	29.2	0.084	0.08	11973	0.82	1.04	6.10	38.65	6.34	

Table 12: Louver slot cooling experimental conditions.

Velocity Ratio	Momentum Flux Ratio	Blowing Ratio	Density Ratio
VR	I	BR	DR
1.02	1.09	1.06	1.04
1.55	2.51	1.62	1.04
2.18	4.93	2.27	1.04
2.53	6.64	2.63	1.04

Table 13: Louver slot cooling effective blowing ratios.

Effusion BR	Louver Slot BR	Effective BR without Louver Slot
2.33	1.06	3.29
3.75	1.62	5.29
5.42	2.27	7.66
6.34	2.63	8.95

7.6 Test Section Velocity, Pressure, and Blowing Ratio Variations

Additional understanding of the impingement jet coolant supply arrangement is provided by the data in Figures 63-65. Here, the normalized pressure drop is presented as it varies with blowing ratio for the cross flow and main flow passage (Figure 63), impingement and cross flow passage (Figure 64), and impingement and the cross flow passages (Figure 65). These data are presented for a $Re_{ms,avg}$ main flow Reynolds number of 92000 to 102000. Because coolant air is supplied to the louver feed holes and the effusion holes from the same cross flow passage source, pressure variations associated with the louver alone cannot be determined separately.

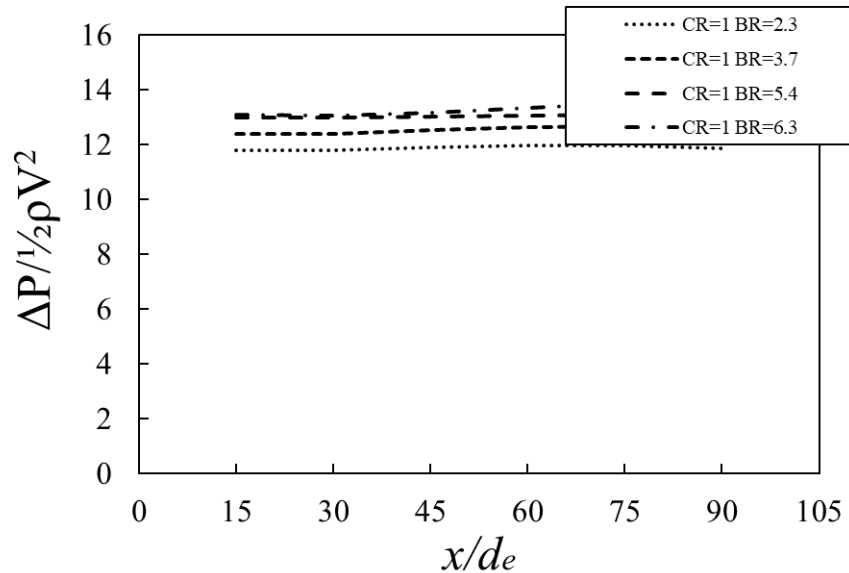


Figure 63: Normalized pressure variations between cross flow to mainstream for mainstream Reynolds values of $Re_{ms,avg}=92000$ to 102000 .

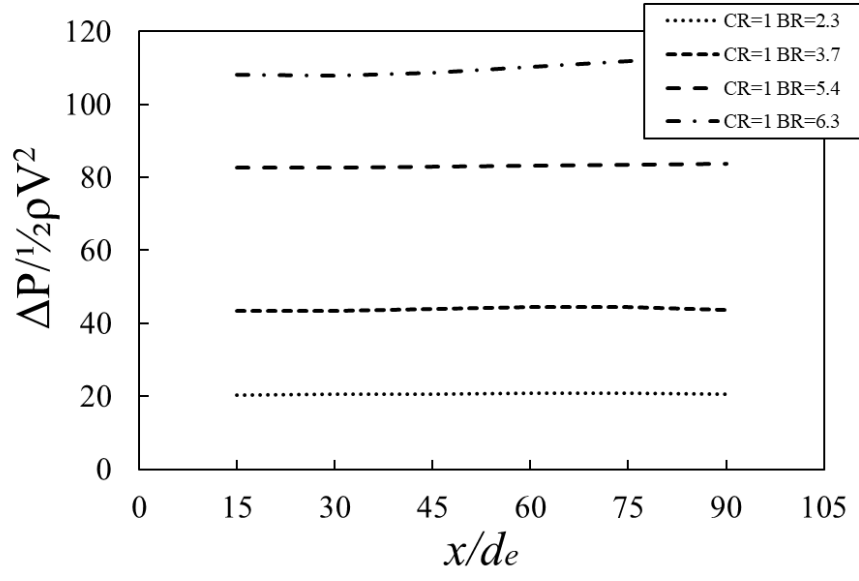


Figure 64: Normalized pressure variations between impingement flow to mainstream for mainstream Reynolds values of $Re_{ms,avg}=92000$ to 102000 .

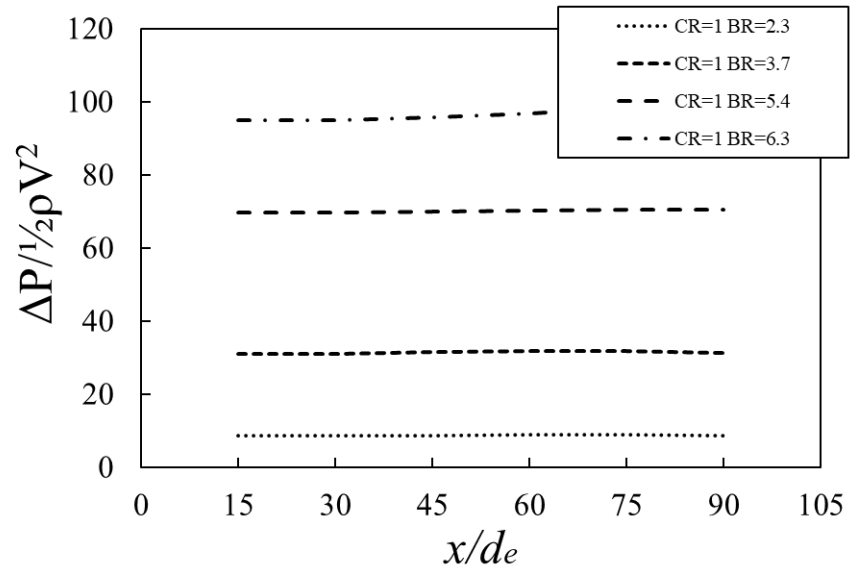


Figure 65: Normalized pressure variations between impingement flow to cross flow for mainstream Reynolds values of $Re_{ms,avg}=92000$ to 102000 .

The resulting alterations of local main flow freestream velocity and spatially-averaged effusion flow velocity with blowing ratio are then given in Figures 67 and 68, respectively. Because the test section inlet and outlet areas are the same within the current study, no significant pressure gradient is present in the main flow passage, and the freestream velocity is constant with streamwise position. Figure 67 shows that this freestream velocity is also invariant with blowing ratio. The associated main flow static pressure is also generally invariant with x/d_e streamwise

location and blowing ratio, as shown in Figure 66. Figure 69 then presents local blowing ratio changes with normalized streamwise location x/de for different initial blowing ratio values.

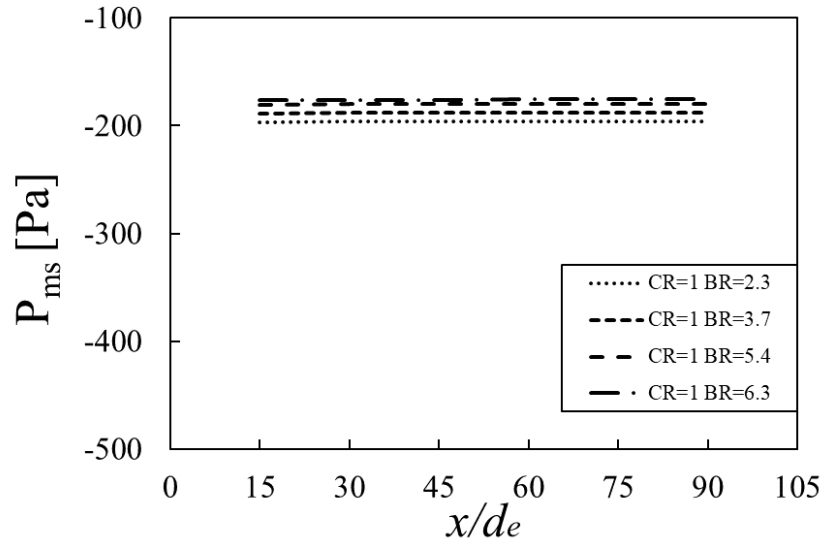


Figure 66: Mainstream pressure variations for mainstream Reynolds values of $Re_{ms,avg}=92000$ to 102000 .

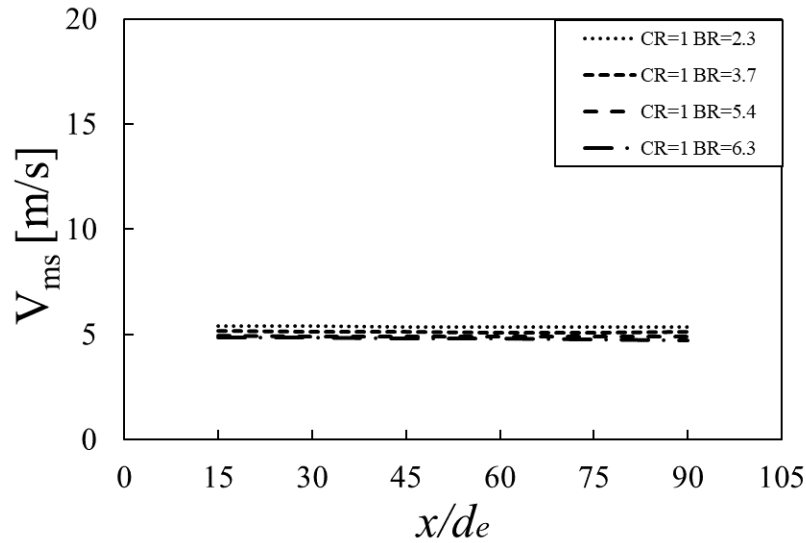


Figure 67: Mainstream velocity variations for mainstream Reynolds values of $Re_{ms,avg}=92000$ to 102000 .

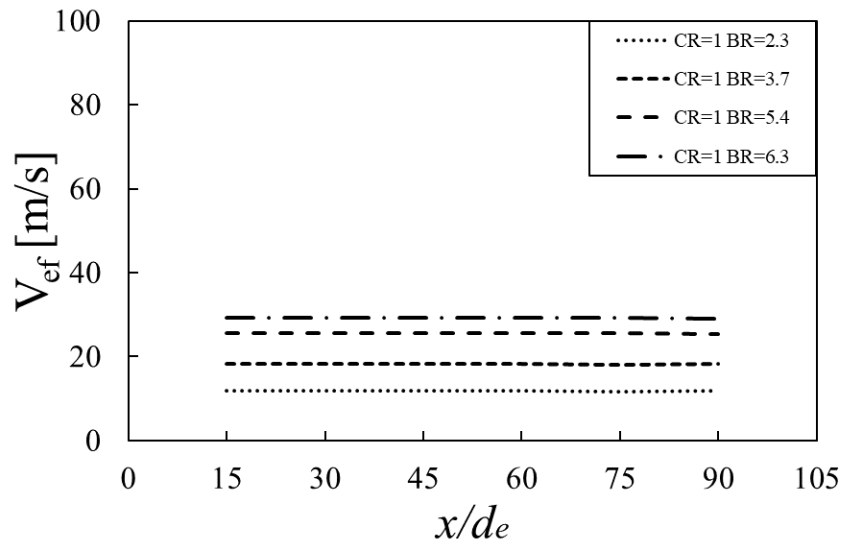


Figure 68: Effusion hole exit velocity variations for mainstream Reynolds values of $Re_{ms,avg}=92000$ to 102000 .

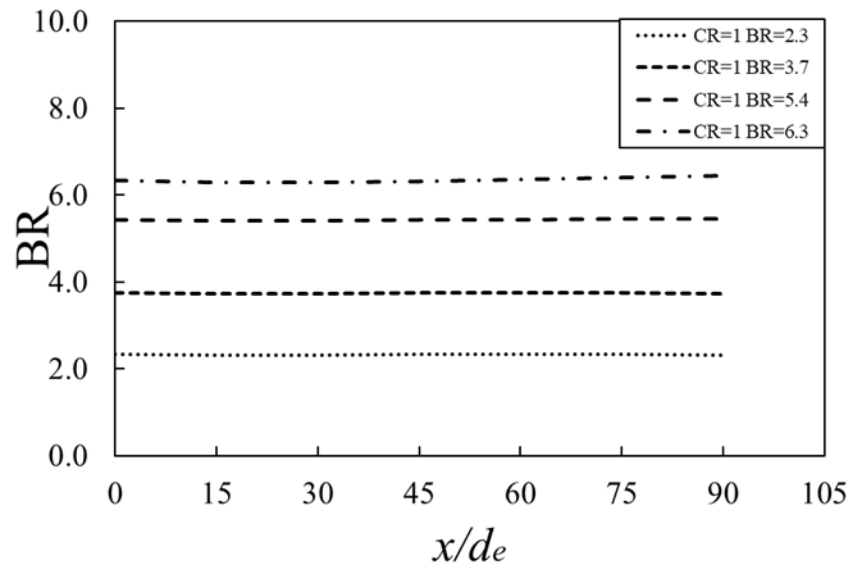


Figure 69: Blowing ratio variations for mainstream Reynolds values of $Re_{ms,avg}=92000$ to 102000 .

7.7 Line-Averaged Cold-Side Data for Impingement Jet Array Only Arrangement

Line-averaged Nusselt number data for impingement jet array only cooling are presented in Figure 70 as they vary with x/d_e , for the cold side of the double-wall test plate. Such results are determined from surface distributions of local, spatially-resolved surface Nusselt numbers. The data in Figure 70 are given for initial blowing ratios of 2.3, 3.7, 5.4, and 6.3, and for main flow Reynolds numbers $Re_{ms,avg}$ of 92000 to 102000. Measured test surface Nusselt numbers within

these figures vary from 20 to values as high as 75, and are given for the CR=1 impingement only cooling configuration. Within this figure, the upstream edge of the spatially-resolved measurements is located at $x/de=0$. Regardless of the value of initial blowing ratio BR, results in Figure 70 show that the highest line-averaged Nusselt numbers are often present at larger x/de locations, relative to the locations of the impingement hole centerlines. These locally augmented Nusselt number regions are then often positioned at lower x/de locations, relative to effusion hole entrance streamwise locations. When compared for a particular streamwise location x/de and mainstream Reynolds number $Re_{ms,avg}$, line-averaged Nusselt numbers in Figure 70 often increase with initial blowing ratio BR, especially for larger x/de values, and especially near impingement jet impact locations. These changes are directly related to increases of the impingement jet Reynolds number.

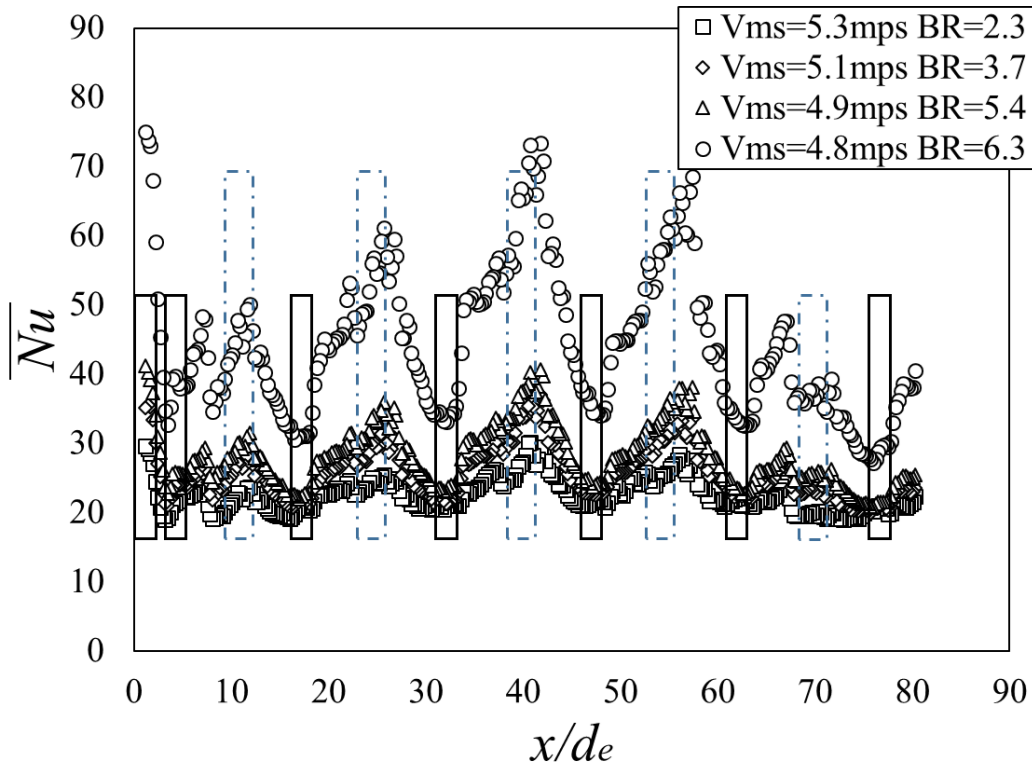


Figure 70: Cold-side line-averaged surface Nusselt number variations with normalized streamwise location for different values of initial blowing ratio for $Re_{ms,avg}=92000$ to 102000 . Solid rectangles denote effusion hole entrance streamwise locations. Dashed rectangles denote impingement hole streamwise locations.

7.8 Line-Averaged Cold-Side Nusselt Number Data for Different Coolant Supply Arrangements

Line-averaged Nusselt number data for the cold side of the double-wall test plate, and for different coolant supply arrangements, are given in Figures 71-74. Compared in these figures are data for the CR=1 louver and effusion cooling, with combination cross flow and impingement jet array coolant supply, and CR=1 louver and effusion cooling with impingement jet array only coolant supply.

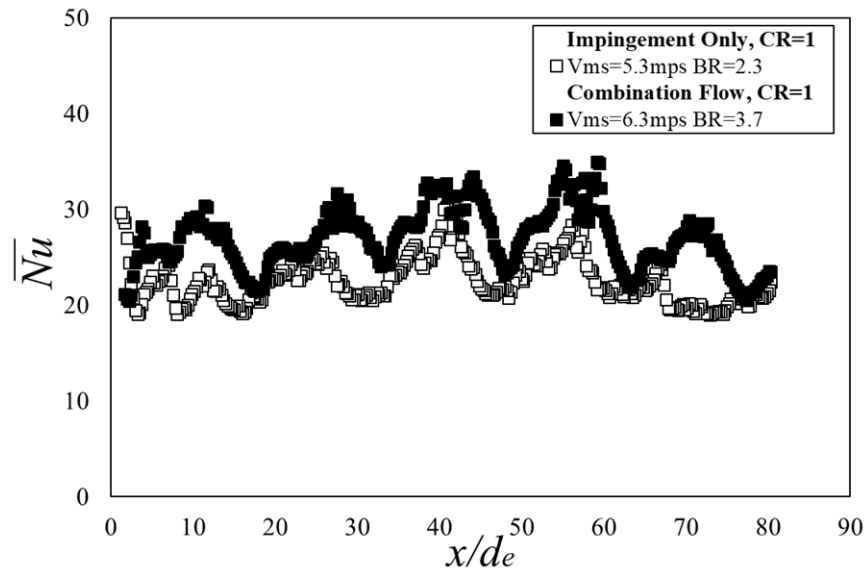


Figure 71: Comparison of line-averaged surface Nusselt number variation between impingement only and cross flow and impingement together for BR=2.3 and BR=3.7, respectively.

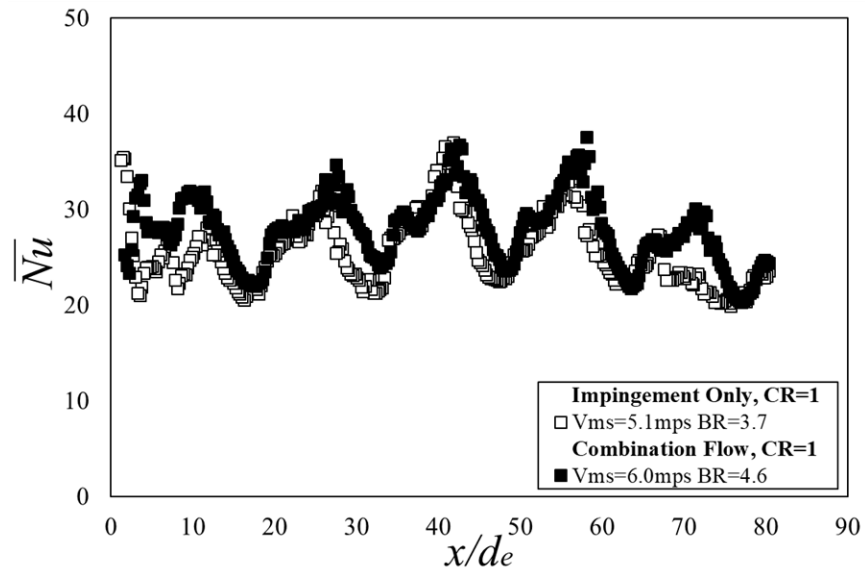


Figure 72: Comparison of line-averaged surface Nusselt number variation between impingement only and cross flow and impingement together for BR=3.7 and BR=4.6, respectively.

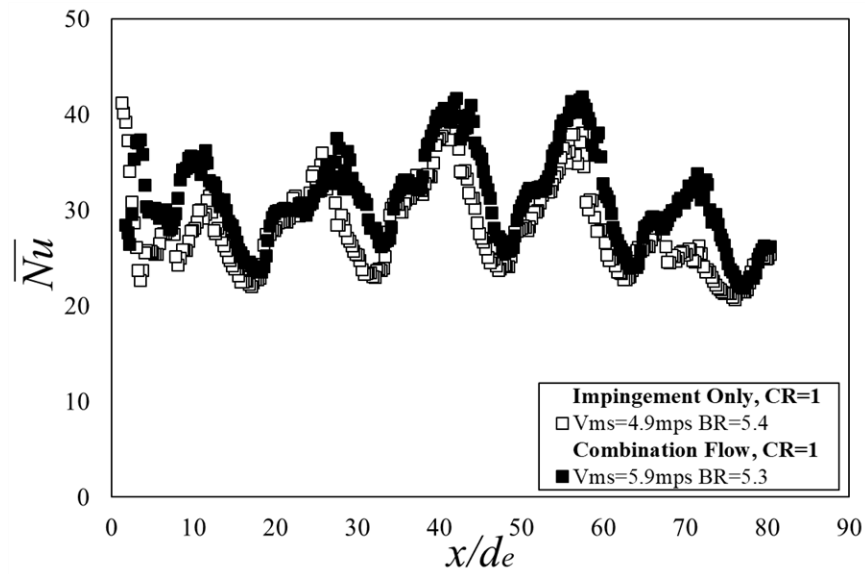


Figure 73: Comparison of line-averaged surface Nusselt number variation between impingement only and cross flow and impingement together for BR=5.4 and BR=5.3, respectively.

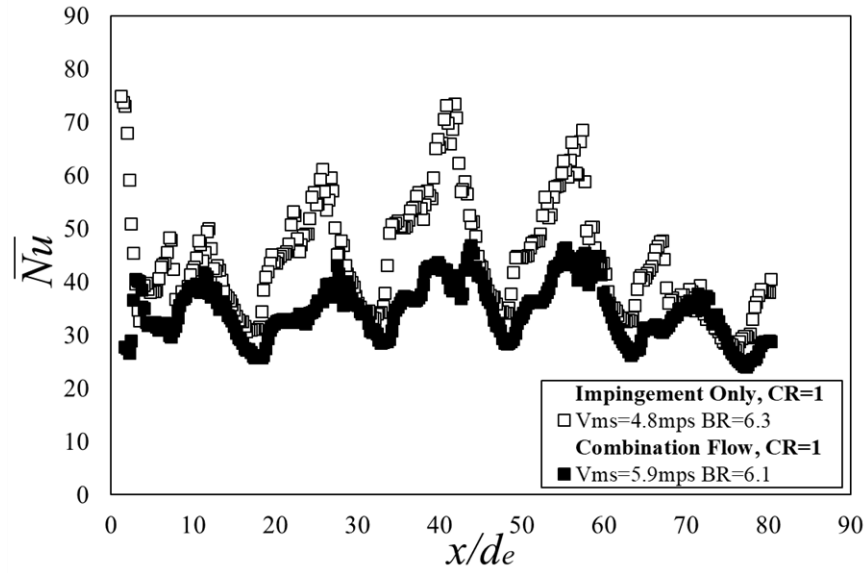


Figure 74: Comparison of line-averaged surface Nusselt number variation between impingement only and cross flow and impingement together for BR=6.3 and BR=6.1, respectively.

Chapter 8: Summary and Conclusions

Presented are experimental heat transfer data for five different experimental configurations, where results are provided on different sides of the effusion plate, with full-coverage effusion cooling, both with and without louver slot injection. Three different coolant supply arrangements are considered, including a cross flow only arrangement, an impingement jet array only arrangement, and a combination cross flow and impingement jet array arrangement. Contraction ratios of 1 and 4 are used within the main flow passage to provide streamwise development with a zero pressure gradient, as well as with a strong favorable pressure gradient. With the five configurations, data are given for: (1) the film cooled side of the effusion plate, for effusion only cooling, with a combination coolant supply arrangement, (2) the cross flow side of the effusion plate, for effusion only cooling, with a combination coolant supply arrangement, (3) the film cooled side of the effusion plate, with louver and effusion combination cooling, with a combination coolant supply arrangement, (4) the cross flow side of the effusion plate, with louver and effusion combination cooling, with a combination coolant supply arrangement, and (5) the cross flow side of the effusion plate, with louver and effusion combination cooling, with an impingement only coolant supply. Results for these five configurations are given in Chapters 3, 4, 5, 6, and 7, respectively.

For configurations (1) and (2), presented are the effects of different coolant supply arrangements on surface thermal performance for both sides of a double-wall cooled effusion plate. Supply arrangements include a cross flow only arrangement, an impingement jet array only arrangement, and a combination cross flow and impingement jet array arrangement. A favorable streamwise pressure gradient is provided by a main flow passage contraction ratio CR of 4, which is characterized using the acceleration parameter $K=(v/V_{ms}^2)(dV_{ms}/dx)$. For the effusion cooled/hot surface, presented are spatially-resolved distributions of surface adiabatic film cooling effectiveness, and surface heat transfer coefficients (measured using transient infrared thermography). For the coolant/cold side, presented are spatially-resolved distributions of surface Nusselt numbers (measured using steady-state liquid crystal thermography). These results are given for main flow Reynolds numbers $Re_{ms,avg}$ of 222,000 to 233,000. Four different combination values of crossflow Reynolds number and impingement Reynolds number are tested, which are associated with four different values of initial blowing ratio BR. With this arrangement, crossflow Reynolds number is approximately constant as impingement jet Reynolds number is varied.

With configuration (3), considered are experimentally-measured results wherein a louver slot is employed upstream of an array full coverage film cooling holes. The present results deviate from those from other prior investigations, because of the particular louver slot arrangement that is employed, and because of the unique coolant supply configurations. A combination arrangement is employed to supply the cooling air with both an impingement jet array and cross flow used together, such that the cross flow Reynolds number is roughly invariant, as the impingement jet Reynolds number is varied. The louver consists of an aligned collection of film cooling holes, contained within a specially-designed device which concentrates, and directs the coolant from a slot, so that it then advects as a layer downstream along the test surface. This louver-supplied coolant is then supplemented by coolant which emerges from different rows of downstream film cooling holes. The same coolant supply passage is employed for the louver row of holes, as well as for the film cooling holes, such that different louver and film cooling rates of mass flow and blowing ratios are set by different hole diameters for the two different types of cooling holes. Experimental results are given and discussed for mainstream Reynolds numbers from 107000 to 114000, and full-coverage blowing ratios from 3.68 to 5.70, with constant values as x/d_e changes and flow develops along the test surface. Corresponding louver slot blowing ratios then range from 1.72 to 2.65.

Provided for configuration (3) are measured distributions of local and spanwise-averaged heat transfer coefficient and adiabatic effectiveness values, both of which show less variation with streamwise development location, relative to results obtained without a louver employed, as considered at the same approximate cross flow Reynolds number, effective blowing ratio, impingement jet Reynolds number, and mainstream Reynolds number. The louver also gives more uniform data variations, as normalized spanwise location y/d_e changes, for each streamwise location which is considered. When compared at the same effective blowing ratio or the same impingement jet Reynolds number, spanwise-averaged heat transfer coefficients are consistently lower, especially for the downstream portions of the test plate, when the louver is utilized. With the same type of comparisons, the presence of the louver slot results in significantly larger adiabatic film cooling effectiveness values which are line-averaged, particularly at and near the upstream portions of the test plate. With such characteristics, dramatic increases in thermal protection are provided by the presence of the louver slot, depending upon experimental condition and test surface location.

For upstream locations along the hot-side of the effusion plate with configuration (1), such as $x/d_e=30$, the addition of cross flow to impingement cooling (employed with the combination cooling arrangement) generally seems to alter and sometimes degrade associated coolant distributions on the hot-side of the effusion plate, for the present experimental conditions and configurations. Such characteristics for this streamwise location are evidenced by line-averaged adiabatic film cooling values for the cross flow/impingement combination configuration, which are substantially lower than impingement only arrangement values for BR values greater than 6.0. When $x/d_e=80$, line-averaged adiabatic film cooling values, for the impingement only arrangement and for the cross flow/impingement combination configuration, are in approximate agreement as BR varies, such that values for both arrangements increase dramatically with initial blowing ratio BR. Such variations for $x/d_e=80$ are a result of higher concentrations of effusion coolant along the test surface from the different rows of effusion holes for both of these cooling arrangements. Resulting coolant distributions are then tied to reduced cross flow influences with the cross flow passage, as x/d_e increases, for the cross flow/impingement combination. As a consequence, coolant is inserted into the entrance of each effusion hole from each adjacent impingement hole in an efficient manner.

Configuration (1) results also show that, overall, for larger x/d_e values, the cross flow/impingement combination behaves in a manner which is similar to the impingement only arrangement. Also measured are sequential increases of $\bar{\eta}$ with streamwise development for these configurations, which are due to accumulations of effusion coolant along the test surface. In most cases, coolant accumulations with x/d_e location are so pronounced that they offset the effects of decreasing local blowing ratio values with streamwise development, as well as main flow acceleration. The influences of local blowing ratio variations and main flow acceleration are more pronounced for heat transfer coefficient data, than for film effectiveness data, because the former are more strongly affected by magnitudes and distributions of local turbulent transport. As a result, line-averaged heat transfer coefficient values for $x/d_e=80$ are lower than values for $x/d_e=35$, when compared for the same coolant supply configuration and initial blowing ratio.

When compared at a particular BR value with configuration (2), cold-side measurements show that line-averaged Nusselt number are generally highest for the impingement only configuration, and lowest for the cross flow only arrangement. Nusselt number data associated with the cross flow/impingement combination generally increase as BR increases, whereas the cross flow only

data increase only slightly with initial blowing ratio. Locally augmented Nusselt number provide evidence of turning and re-direction of the impingement jets, as the jet fluid crosses the cross flow passage. Associated variations indicate that the impingement jets are more influential in affecting local and line-averaged Nusselt number variations, than the cross flow. Evidence of cross flow influences (for the cross flow/impingement combination arrangement) are additionally provided by cross flow/impingement combination Nusselt numbers, relative to the impingement only values, with differences that are more pronounced for locations between impingement jets ($x/d_e=45$), and less pronounced for locations closer to impingement jet centerlines ($x/d_e=37$).

References

- Al Dabagh, A. M., Andrews, G. E., Abdul Husain, R. A. A., Husain C. I., Nazari, A., and Wu, J., 'Impingement/Effusion Cooling: The Influence of the Number of Impingement Holes and Pressure Loss on the Heat Transfer Coefficient,' *Journal of Turbomachinery* 112 (1990) 467-476.
- Allgaier, C., Ren, Z., Vanga, S. R., Ligrani, P. M., Liberatore, F., Patel, R., Srinivasan, R., and Ho, Y.-H., "Double Wall Cooling of a Full Coverage Effusion Plate With Cross Flow Supply Cooling and Main Flow Pressure Gradient," ASME TURBO EXPO 2018 GT2018-77061
- Andreini, A., Caciolli, G., Facchini, B., and Tarchi, L., 2012, "Density Ratio Effects on the Cooling Performances of a Combustor Liner Cooled by a Combined Slot-Effusion System," Paper Number GT2012-43434, TURBO EXPO 2012 – 57th TURBO EXPO Turbine Technical Conference and Exposition, Copenhagen, Denmark, June 11-15, 2012.
- Andreini, A., Ceccherini, A., and Facchini, B., 2010, "Combined Effect of Slot Injection, Effusion Array and Dilution Hole on the Heat Transfer Coefficient of a Real Combustor Liner Part 2: Numerical Analysis," Paper Number GT2010-22937, TURBO EXPO 2010 – 55th ASME Gas Turbine Technical Congress and Exposition, Glasgow, Scotland, United Kingdom, June 14-18, 2010.
- Andrews, G. E., Al-Dabagh, A. M., Asere, A. A., Bazdidi-Tehrani, F., Mkpadi, M. C., and Nazari, A., "Impingement/Effusion Cooling". AGARD Conference Proceedings 527, 80th Symposium on Heat Transfer and Cooling in Gas Turbines (1992) 30.1-30.10.
- Andrews G. E., Asere A. A., Husain C. I., Mkpadi M. C., and Nazari A., 'Impingement/Effusion Cooling: Overall Wall Heat Transfer,' ASME Turbo Expo 1988 Paper Number 88-GT-290
- Andrews G. E., and Nazari, A., 'Impingement/Effusion Cooling: Influence of Number of Holes On the Cooling Effectiveness For An Impingement X/D of 10.5 and Effusion X/D of 7.0,' Proceedings of the GTSJ Int. Gas Turbine Congress, Vol. II, IGTC TS-51 (1999) 639 - 646.
- Ceccherini, A., Facchini, B., and Tarchi, L., 2009, "Combined Effect of Slot Injection, Effusion Array and Dilution Hole on the Cooling Performance of a Real Combustion Liner," Paper Number GT2009-60047, 54th ASME TURBO EXPO Gas Turbine and Aeroengine Technical Congress, Exposition, and Users Symposium, Orlando, Florida, June 8-12, 2009.

- Cho, H. H., and Rhee, D. H., 'Local Heat/Mass Transfer Measurement on the Effusion Plate In Impingement/Effusion Cooling Systems,' *Journal of Turbomachinery* 123, (2001) 601-608.
- Cho H. H., Rhee D. H., and Goldstein, R. J., 'Effects of Hole Arrangements on Local Heat/Mass Transfer for Impingement/Effusion Cooling With Small Hole Spacing,' *Journal of Turbomachinery* 130 (2008) 1-11.
- El-Jumrah A. M., Andrews G. E. and Staggs J. E. J., 'Impingement/Effusion Cooling Wall Heat Transfer Conjugate Heat Transfer Computational Fluid Dynamic Predictions,' ASME Turbo Expo 2016 GT2016-56961
- El-Jumrah, A. M., Nazari, A., Andrews, G. E., and Staggs, J. E. J., 'Impingement/Effusion Cooling Wall Heat Transfer: Reduced Number of Impingement Jet Holes Relative to the Effusion Holes' ASME Turbo Expo 2017 GT2017-63494
- Hong S. K., Rhee D. H., and Cho H. H., 'Effects of Fin Shapes and Arrangements on Heat Transfer for Impingement/Effusion Cooling With Cross-Flow,' *Journal of Heat Transfer* 129, (2007) 1697-1707.
- Inanli, S., Yasa, T., and Ulas, A., 2017, "Experimental Investigation of Effusion and Film Cooling for Gas Turbine Combustor," Proceedings of 12th International Conference on Heat Transfer, Fluid Mechanics and Thermodynamics, Malaga, Spain.
- Jia, R., Sunden, B., Miron, P., and Leger, B., 2003, "Numerical and Experimental Study of the Slot Film Cooling Jet With Various Angles," Proceedings of ASME Summer Heat Transfer Conference 2003, ASME, New York, New York, USA, pp. 845-856.
- Juhasz, A. J., and Marek, C. J., 1971, "Combustor Liner Film Cooling in the Presence of High Free-Stream Turbulence," NASA TN D-6360.
- Kiyici, F., Topal, A., Hepkaya, E., and Inanli, S., 2018, "Numerical Investigation of Gas Turbine Combustor Liner Film Cooling Slots," Paper Number GT2018-75608, ASME TURBO EXPO 2018: Turbomachinery Technical Conference and Exposition, Oslo, Norway, June 11-15, 2018.
- Kline, S. J., and McClintock, F. A., 'Describing Uncertainties in Single Sample Experiments,' *Mechanical Engineering* 75 (1953) 3-8.
- Krewinkel, R., 'A Review of Gas Turbine Effusion Cooling Studies,' *International Journal of Heat and Mass Transfer* 66 (2013) 706-722.
- Lefebvre, A. H., 1998, "Gas Turbine Combustion," CRC Press, Boca Raton, Florida, USA.

- Miller, M., Natsui, G., Ricklick, M., Kapat, J., and Schilp, R., "Heat Transfer in a Coupled Impingement-Effusion Cooling System," ASME Turbo Expo 2014 GT2014-26416
- Moffat, R. J., 'Describing the Uncertainties in Experimental Results,' *Experimental Thermal and Fluid Science*, 1 (1988) 3-17.
- Oguntade, H. I., Andrews, G. E., Burns, A. D., Ingham, D. B., and Pourkashanian, M., 'Impingement/Effusion Cooling with Low Coolant Mass Flow,' ASME Turbo Expo 2017 GT2017- 63484
- Ren, Z., Vanga, S. R., Rogers, N., Ligrani, P. M., Hollingsworth, K. D., Liberatore, F., Patel, R., Srinivasan, R., and Ho, Y., 'Internal and External Cooling of a Full Coverage Effusion Cooling Plate: Effects of Double Wall Cooling Configuration and Conditions,' ASME Turbo Expo 2017 GT2017-64921
- Ritchie, D., Click, A., Ligrani, P. M., Liberatore, F., Patel, R., and Ho, Y.-H., 2019, "Double Wall Cooling of an Effusion Plate With Simultaneous Cross Flow and Impingement Jet Array Internal Cooling," *ASME Transactions – Journal of Engineering for Gas Turbines and Power*, 141 (9), pp. 091008-2 to 091008-11.
- Rogers, N., Ren, Z., Buzzard, W., Sweeney, B., Tinker, N., Ligrani, P. M., Hollingsworth, K. D., Liberatore, F., Patel, R., Ho, S., and Moon, H.-K., "Effects of Double Wall Cooling Configuration and Conditions on Performance of Full Coverage Effusion Cooling," Paper Number GT2016-56515, ASME TURBO EXPO 2016: Turbomachinery Technical Conference and Exposition, Seoul, South Korea, June 13-17, 2016.
- Schulz, A., 'Combustor Liner Cooling Technology in Scope of Reduced Pollutant Formation and Rising Thermal Efficiencies,' *Heat Transfer in Gas Turbine Systems*, *Annals of the New York Academy of Sciences* 934 (2001) 135-146.
- Shi, B., Li, J., Li, M., Ren, J., and Jiang, H., 'Cooling Effectiveness on a Flat Plate With Both Film Cooling and Impingement Cooling in Hot Gas Conditions,' ASME Turbo Expo 2016 GT2016-57224
- da Silva, L. M., Tomita, J. T., Bringhamti, C., and Gronstedt, T., 2018, "Numerical Investigation of Film and Impingement Cooling Schemes for Gas Turbine Application," Paper Number GT2018-76222, ASME TURBO EXPO 2018: Turbomachinery Technical Conference and Exposition, Oslo, Norway, June 11-15, 2018.

Vanga, S. R., Ren, Z., Click, A. J., Ligrani, P. M., Liberatore, F., Patel, R., Srinivasan, R., and Ho, Y.-H., “Double Wall Cooling of a Full Coverage Effusion Plate With Main Flow Pressure Gradient, Including Internal Impingement Array Cooling,” ASME TURBO EXPO 2018 GT2018-77036

Appendix A: Data File Directory

The following Appendix provides information on data files used. Data files appear in the order presented.

Configuration (1) & (2)

Re _{ms,avg}	BR	Data File Name	Description
232821	5.0	Flow Data A1 - Flow Data A4.txt	Pressure Readings from LabView for pressure measurements
		Temperature A1 - Temperature A4.txt	Temperature Readings from LabView for pressure measurements
		Flow Data A1 - Flow Data A5.txt	Pressure Readings from LabView for cold side
		Temperature A1 - Temperature A5.txt	Temperature Readings from LabView for cold side
		Temperatures A.txt	Temperature Readings from LabView for hot side
		Case A.wmv	Video File from IR Camera
		A1 - A5.bmp	Images used for cold side data processing
		Case A.xlsx	File used to convert hue values to Nusselt numbers
230528	5.9	Flow Data B1 - Flow Data B4.txt	Pressure Readings from LabView for pressure measurements
		Temperature B1 - Temperature B4.txt	Temperature Readings from LabView for pressure measurements
		Flow Data B1 - Flow Data B5.txt	Pressure Readings from LabView for cold side
		Temperature B1 - Temperature B5.txt	Temperature Readings from LabView for cold side
		Temperatures B.txt	Temperature Readings from LabView for hot side
		Case B.wmv	Video File from IR Camera
		B1 - B5.bmp	Images used for cold side data processing
		Case B.xlsx	File used to convert hue values to Nusselt numbers
226118	6.8	Flow Data C1 - Flow Data C4.txt	Pressure Readings from LabView for pressure measurements
		Temperature C1 - Temperature C4.txt	Temperature Readings from LabView for pressure measurements
		Flow Data C1 - Flow Data C5.txt	Pressure Readings from LabView for cold side
		Temperature C1 - Temperature C5.txt	Temperature Readings from LabView for cold side
		Temperatures C.txt	Temperature Readings from LabView for hot side
		Case C.wmv	Video File from IR Camera
		C1 - C5.bmp	Images used for cold side data processing
		Case C.xlsx	File used to convert hue values to Nusselt numbers
221816	7.9	Flow Data D1 - Flow Data D4.txt	Pressure Readings from LabView for pressure measurements
		Temperature D1 - Temperature D4.txt	Temperature Readings from LabView for pressure measurements
		Temperatures D.txt	Temperature Readings from LabView for hot side
		Case D.wmv	Video File from IR Camera - Data file missing
		D1 - D5.bmp	Images used for cold side data processing
		Case D.xlsx	File used to convert hue values to Nusselt numbers
		HTC & ETA Constant CF High Re.xlsx	File used to Line Average HTC & ETA values
		HTC High Re Cnst Cf March 28.xlsx	File used to plot HTC values and comparisons with previous data
		ETA High Re Cnst Cf March 28.xlsx	File used to plot ETA values and comparisons with previous data
		Pressure Calcs Constant CF High Re	File used to calculate experimental conditions

Configuration (3)

Re _{ms,avg}	BR	Data File Name	Description
113656	3.7	Flow Data A1 - Flow Data A4.txt	Pressure Readings from LabView for pressure measurements
		Temperature A1 - Temperature A4.txt	Temperature Readings from LabView for pressure measurements
		Flow Data A.txt	Pressure Readings from LabView for hot side
		Temperature A.txt	Temperature Readings from LabView for hot side
		Thermocouple Readings A.xlsx	Excel file used by MATLAB to read temperature values
		Case A.wmv	Video File from IR Camera
		110204	4.3
Temperature B1 - Temperature B4.txt	Temperature Readings from LabView for pressure measurements		
Flow Data B.txt	Pressure Readings from LabView for hot side		
Temperature B.txt	Temperature Readings from LabView for hot side		
Thermocouple Readings B.xlsx	Excel file used by MATLAB to read temperature values		
Case B.wmv	Video File from IR Camera		
107801	4.9		
		Temperature C1 - Temperature C4.txt	Temperature Readings from LabView for pressure measurements
		Flow Data C.txt	Pressure Readings from LabView for hot side
		Temperature C.txt	Temperature Readings from LabView for hot side
		Thermocouple Readings C.xlsx	Excel file used by MATLAB to read temperature values
		Case C.wmv	Video File from IR Camera
		106610	5.7
Temperature D1 - Temperature D4.txt	Temperature Readings from LabView for pressure measurements		
Flow Data D.txt	Pressure Readings from LabView for hot side		
Temperature D.txt	Temperature Readings from LabView for hot side		
Thermocouple Readings D.xlsx	Excel file used by MATLAB to read temperature values		
Case D.wmv	Video File from IR Camera		
		HTC Constant CF Low Re Louver.xlsx	File used to plot HTC values and comparisons with previous data
		ETA Constant CF Low Re Louver.xlsx	File used to plot ETA values and comparisons with previous data
		Pressure Calcs Constant CF Low Re Louver.xlsx	Excel file used to calculate experimental conditions

Configuration (4)

Re _{ms,avg}	BR	Data File Name	Description
174256	3.9	Flow Data A1 - Flow Data A4.txt	Pressure Readings from LabView for pressure measurements
		Temperature A1 - Temperature A4.txt	Temperature Readings from LabView for pressure measurements
		Temperature A1 - Temperature A5.txt	Temperature Readings from LabView for cold side
		A1 - A5.bmp	Images used for cold side data processing
		Case A.xlsx	File used to convert hue values to Nusselt numbers
172376	4.6	Flow Data B1 - Flow Data B4.txt	Pressure Readings from LabView for pressure measurements
		Temperature B1 - Temperature B4.txt	Temperature Readings from LabView for pressure measurements
		Temperature B1 - Temperature B5.txt	Temperature Readings from LabView for cold side
		B1 - B5.bmp	Images used for cold side data processing
		Case B.xlsx	File used to convert hue values to Nusselt numbers
169697	5.4	Flow Data C1 - Flow Data C4.txt	Pressure Readings from LabView for pressure measurements
		Temperature C1 - Temperature C4.txt	Temperature Readings from LabView for pressure measurements
		Flow Data C1 - Flow Data C5.txt	Pressure Readings from LabView for cold side
		Temperature C1 - Temperature C5.txt	Temperature Readings from LabView for cold side
		C1 - C5.bmp	Images used for cold side data processing
	Case C.xlsx	File used to convert hue values to Nusselt numbers	
166078	6.5	Flow Data D1 - Flow Data D4.txt	Pressure Readings from LabView for pressure measurements
		Temperature D1 - Temperature D4.txt	Temperature Readings from LabView for pressure measurements
		Temperature D1 - Temperature D5.txt	Temperature Readings from LabView for cold side
		D1 - D5.bmp	Images used for cold side data processing
		Case D.xlsx	File used to convert hue values to Nusselt numbers
	HolesPlacement.pptx	PowerPoint Used to position boxes denoting Impingement and Effusion holes on plots	
	Constant CF Cold Side High Re.xlsx	Excel file used to plot and compare surface Nusselt Numbers	
	Pressure Calcs Constant CF High Re Louver.xlsx	Excel file used to calculate experimental conditions	

Configuration (5) High Reynolds

Re _{ms,avg}	BR	Data File Name	Description
160404	2.3	Flow Data A1 - Flow Data A4.txt	Pressure Readings from LabView for pressure measurements
		Temperature A1 - Temperature A4.txt	Temperature Readings from LabView for pressure measurements
		Flow Data A1 - Flow Data A5.txt	Pressure Readings from LabView for cold side
		Temperature A1 - Temperature A5.txt	Temperature Readings from LabView for cold side
		A1 - A5.bmp	Images used for cold side data processing
		Case A.xlsx	File used to convert hue values to Nusselt numbers
154449	3.6	Flow Data B1 - Flow Data B4.txt	Pressure Readings from LabView for pressure measurements
		Temperature B1 - Temperature B4.txt	Temperature Readings from LabView for pressure measurements
		Flow Data B1 - Flow Data B5.txt	Pressure Readings from LabView for cold side
		Temperature B1 - Temperature B5.txt	Temperature Readings from LabView for cold side
		B1 - B5.bmp	Images used for cold side data processing
		Case B.xlsx	File used to convert hue values to Nusselt numbers
147657	5.2	Flow Data C1 - Flow Data C4.txt	Pressure Readings from LabView for pressure measurements
		Temperature C1 - Temperature C4.txt	Temperature Readings from LabView for pressure measurements
		Flow Data C1 - Flow Data C5.txt	Pressure Readings from LabView
		Temperature C1 - Temperature C5.txt	Temperature Readings from LabView
		C1 - C5.bmp	Images used for cold side data processing
		Case C.xlsx	File used to convert hue values to Nusselt numbers
145083	6.1	Flow Data D1 - Flow Data D4.txt	Pressure Readings from LabView for pressure measurements
		Temperature D1 - Temperature D4.txt	Temperature Readings from LabView for pressure measurements
		Flow Data D1 - Flow Data D5.txt	Pressure Readings from LabView for cold side
		Temperature D1 - Temperature D5.txt	Temperature Readings from LabView for cold side
		D1 - D5.bmp	Images used for cold side data processing
		Case D.xlsx	File used to convert hue values to Nusselt numbers
		ImpEffusionHolesPlacement.pptx	PowerPoint used to position boxes denoting Impingement and Effusion holes on plots
		ImpOnlyHoles.pptx	PowerPoint used to position white circles over effusion holes
		Imp Only Cold Side High Re.xlsx	Excel file used to plot and compare surface Nusselt Numbers
		Pressure Calcs Impingement Only High Re Louver.xlsx	Excel file used to calculate experimental conditions

Configuration (5) Low Reynolds

Re _{ms,avg}	BR	Data File Name	Description
102426	2.3	Flow Data A1 - Flow Data A4.txt	Pressure Readings from LabView for pressure measurements
		Temperature A1 - Temperature A4.txt	Temperature Readings from LabView for pressure measurements
		Flow Data A1 - Flow Data A5.txt	Pressure Readings from LabView for cold side
		Temperature A1 - Temperature A5.txt	Temperature Readings from LabView for cold side
		A1 - A5.bmp	Images used for cold side data processing
		Case A.xlsx	File used to convert hue values to Nusselt numbers
97674	3.8	Flow Data B1 - Flow Data B4.txt	Pressure Readings from LabView for pressure measurements
		Temperature B1 - Temperature B4.txt	Temperature Readings from LabView for pressure measurements
		Flow Data B1 - Flow Data B5.txt	Pressure Readings from LabView for cold side
		Temperature B1 - Temperature B5.txt	Temperature Readings from LabView for cold side
		B1 - B5.bmp	Images used for cold side data processing
		Case B.xlsx	File used to convert hue values to Nusselt numbers
93570	5.4	Flow Data C1 - Flow Data C4.txt	Pressure Readings from LabView for pressure measurements
		Temperature C1 - Temperature C4.txt	Temperature Readings from LabView for pressure measurements
		Flow Data C1 - Flow Data C5.txt	Pressure Readings from LabView for cold side
		Temperature C1 - Temperature C5.txt	Temperature Readings from LabView for cold side
		C1 - C5.bmp	Images used for cold side data processing
		Case C.xlsx	File used to convert hue values to Nusselt numbers
91779	6.3	Flow Data D1 - Flow Data D4.txt	Pressure Readings from LabView for pressure measurements
		Temperature D1 - Temperature D4.txt	Temperature Readings from LabView for pressure measurements
		Flow Data D1 - Flow Data D5.txt	Pressure Readings from LabView for cold side
		Temperature D1 - Temperature D5.txt	Temperature Readings from LabView for cold side
		D1 - D5.bmp	Images used for cold side data processing
		Case D.xlsx	File used to convert hue values to Nusselt numbers
		ImpEffusionHolesPlacement.pptx	PowerPoint Used to position boxes denoting Impingement and Effusion holes on plots
		ImpOnlyHoles.pptx	PowerPoint used to position white circles over effusion holes
		Imp Only Cold Side Low Re.xlsx	Excel file used to plot and compare surface Nusselt Numbers
		Pressure Calcs Impingement Only Low Re Louver.xlsx	Excel file used to calculate experimental conditions

Appendix B: Software Directory

Software	File Name	Description
LabView Professional Development System version 17.0 (2017)	Facility_Measurements Louver Data	LabView Program to collect data from thermocouples and pressure transducers
LiquiTherm Image Processor	LiquiTherm Image Processor.jar	Used to convert pixel color to hue angle
FlyCapture	Point Grey FlyCap2.exe	Used to collect liquid crystal images
ResearchIR		Used to record and export files from the infrared camera
Excel 2016	LCCalibration.xlsx	Used to determine correlation between temperature and liquid crystal hue values
MATLAB	IRTransientAnalysis v12	Used to determine surface heat transfer coefficients and perform in situ calibration of IR camera
MATLAB	ContourPlotsCR1	Used to plot surface contour plots for hot-side heat transfer data
MATLAB	desT2qsiimp1	Used to convert grayscale values to temperatures and calculate HTC